TECHNISCHE UNIVERSITÄT WIEN

Monolithic Metal-Semiconductor-Metal Heterostructures for electro-plasmonic hybrid devices

PhD thesis by

Zehao Song, MSc

Institute of Solid State Electronics

Technische Universität Wien

Supervisor

Ao.Univ.Prof. Dipl.-Ing. Dr.techn. Alois Lugstein

Vienna, June 2023

Die approbierte gedruckte Originalversion dieser Dissertation ist an der TU Wien Bibliothek verfügbar.
The approved original version of this doctoral thesis is available in print at TU Wien Bibliothek.
TU WIEN Bibliothek Your knowledge hub

TU WIEN Bibliothek Your knowledge hub
Die approbierte gedruckte Originalversion dieser Dissertation ist an der TU Wien Bibliothek verfügbar.
The approved original version of this doctoral thesis is available in print at TU Wien Bibliothek.

Die approbierte gedruckte Originalversion dieser Dissertation ist an der TU Wien Bibliothek verfügbar.
The approved original version of this doctoral thesis is available in print at TU Wien Bibliothek.
TU WIEN Bibliothek Your knowledge hub

Statutory Declaration

I declare, that I have authored the present work independently according to the code of conduct, that I have not used other than the declared sources and that I have explicitly marked all material quoted either literally or by content from the used sources. This work was not yet submitted to any examination procedure neither in Austria, nor in any other country.

Erklärung zur Verfassung der Arbeit

Hiermit erkläre ich, dass die vorliegende Arbeit gemäß dem Code of Conduct - Regeln zur Sicherung guter wissenschaftlicher Praxis - ohne unzulässige Hilfe Dritter und ohne Benutzung anderer als der angegebenen Hilfsmittel, angefertigt wurde. Die aus anderen Quellen direkt oder indirekt übernommenen Daten und Konzepte sind unter Angabe der Quelle gekennzeichnet. Die Arbeit wurde bisher weder im In- noch im Ausland in gleicher oder in ähnlicher Form in anderen Prüfungsverfahren vorgelegt.

Vienna, June 2023 .... Zehao Song ....

Die approbierte gedruckte Originalversion dieser Dissertation ist an der TU Wien Bibliothek verfügbar.
The approved original version of this doctoral thesis is available in print at TU Wien Bibliothek.
TU WIEN Bibliothek Your knowledge hub

Die approbierte gedruckte Originalversion dieser Dissertation ist an der TU Wien Bibliothek verfügbar.
The approved original version of this doctoral thesis is available in print at TU Wien Bibliothek.
TU WIEN Bibliothek Your knowledge hub

Abstract

Nowadays, an industrial requirement of ultra-fast optical interconnects has been set out for silicon photonics' technology, as metallic wire-based electrical interconnects face severe challenges including substantial loss, crosstalk and power dissipation in advanced CMOS technology nodes. An essential component for optical interconnections is scalable high-speed photodetectors as the receivers that can be integrated on the chip. Miniaturization of the semiconductor photodetector would dramatically enhance its bandwidth, but at the cost of responsivity due to a shortened absorption length. This so-called efficiency-speed trade-off is an obstacle for combining the compactness of an electronic circuit with the bandwidth of a photonic network. Although, very fast photodetectors based on group III-V materials have been reported, their integration into mature Si platform technology is a major challenge for large-scale implementation. Thus, from the material side, germanium is an obvious choice for the realization of a high-bandwidth on-chip photodetector, since it provides high charge carrier mobility, compatibility with CMOS technology and a small bandgap covering the established telecommunication C-band.

Further advances in addressing the bandwidth-quantum efficiency trade-off may rely on plasmonics, which can concentrate electromagnetic energy well below the diffraction limit, into structures as small as a few tens of nanometers. Plasmon assisted metal/semiconductor hybrid devices have proven to be particularly suitable for this purpose. Such devices use ultimately hot charge carriers, arising from non-radiative plasmon decay at the metal/semiconductor interface, to directly generate a detectable current. Self-powered hot-carrier photodetectors, which have the capability of generating a net photocurrent at zero bias are of particular interest in order to reduce the power consumption of the overall optical link.

However, without detailed understanding of the underlying mechanisms of plasmon-induced hot carriers transfer and transport dynamics at the metal-semiconductor interface, proper material matching and design considerations are extremely challenging. Here, monolithic metal-semiconductor-metal heterostructures, involving Al-Ge-Al or Al-Si-Al, are employed as a research platform. The fabrication of such monolithic metal-semiconductor heterostructures, with atomically sharp interfaces, could be achieved by a process we developed based on a thermally induced solid-state exchange reaction.

Light absorption, surface plasmon generation and separation of hot charge carriers arising from the non-radiative decay of surface plasmons is realized in a monolithic Schottky barrier field effect transistor. Such electrostatic gated heterojunction devices enable to tune the effective

barrier height at the abrupt metal-semiconductor interface to control the plasmon-induced hot carrier injection. Further the monolithic Al leads perform a dual function and simultaneously carry both optical and electrical signals, giving rise to exciting new capabilities.

Aluminum have been chosen as it is CMOS compatible and is excellent for plasmonics, because of its broad response spectrum from ultraviolet to infrared, and a self-limiting native oxide layer protecting the metal surface.

For such devices some novel physical phenomena related to the dynamics of hot carriers inside the germanium channel are demonstrated, including negative photoconductivity and detectors with superlinear responsivity. An ultra-scaled prototype device with a deep-sub-micrometer scaled Ge channel comprises in effect a hot-carrier photodetector with a ballistic carrier transport, enabling a bandwidth of 50 GHz at 1560 nm at notably zero bias.

Using an Al-Si-Al device with splitgate architecture, effective charge separation of the plasmonically injected hot charge carriers could be demonstrated for the first time, thus demonstrating a function comparable to that of an on-chip photovoltaic device.

Die approbierte gedruckte Originalversion dieser Dissertation ist an der TU Wien Bibliothek verfügbar.
The approved original version of this doctoral thesis is available in print at TU Wien Bibliothek.
TU Bibliothek WIEN Your knowledge hub

Kurzfassung

Aktuell wir intensiv an ultraschnellen optischen Signalleitungen geforscht, da die Metallisierung fortgeschrittener CMOS-Technologieknoten zunehmend mit erheblichen Verlusten und der Problematik des Übersprechens konfrontiert ist. Eine Schlüsselkomponente für optische Signalleitung sind skalierbare Hochgeschwindigkeits-Photodetektoren als Empfänger, die auf dem Chip integriert werden können. Die Miniaturisierung eines Halbleiterphotodetektors würde seine Bandbreite drastisch erhöhen, allerdings auf Kosten der Empfindlichkeit aufgrund der einhergehenden Verkürzung der Absorptionslänge. Dieser so genannte Effizienz-Geschwindigkeits-Kompromiss erschwert die Kombination der Kompaktheit elektronischer Schaltungen mit der großen Bandbreite eines photonischen Netzwerks. Obwohl bereits sehr schnelle Photodetektoren auf der Basis von III-V-Materialien entwickelt wurden, stellt deren Integration in die ausgereifte Siliziumtechnologie eine große Herausforderung für die technische Umsetzung dar. Von der Materialseite her ist für die Realisierung eines On-Chip-Photodetektors mit hoher Bandbreite besonders Germanium geeignet, da es eine hohe Ladungsträgerbeweglichkeit, CMOS-Kompatibilität und eine kleine Bandlücke aufweist, die das etablierte C-Band der Telekommunikation abdeckt.

Für die Kombination von Bandbreite und Quanteneffizienz erweist sich Plamonik als nützlich, da hierbei elektromagnetische Energie in nur einige zehn Nanometer große Strukturen konzentrieren werden kann, also weit unterhalb der Beugungsgrenze des Lichts.

Plasmonische Metall-Halbleiter-Hybridbauelemente haben sich für diesen Zweck als besonders geeignet erwiesen. Solche Bauelemente nutzen letztlich die heißen Ladungsträger, die beim nicht-strahlenden Plasmonenzerfall an der Metall/Halbleiter-Grenzfläche entstehen. Sogenannte Hot-Carrier-Photodetektoren, die in der Lage sind, bei Nullvorspannung einen Nettophotostrom zu erzeugen, sind dabei von besonderem Interesse, um den Stromverbrauch der gesamten optischen Signalverarbeitung zu verringern.

Ohne ein detailliertes Verständnis der zugrundeliegenden Mechanismen des plasmoneninduzierten Transfers von heißen Ladungsträgern und der Transportdynamik an der Metall-Halbleiter-Grenzfläche sind die richtige Materialanpassung und Designüberlegungen der entsprechenden Bauteile jedoch eine große Herausforderung. In dieser Arbeit wurden monolithische Metall-Halbleiter-Metall-Heterostrukturen mit Al-Ge-Al oder Al-Si-Al als Forschungsplattform eingesführtt. Die Herstellung solcher monolithischer Metal-Halbleiterheterostrukturen mit atomar scharfen Grenzflächen konnte durch einen von uns entwickelten Prozess erreicht werden der auf einer thermisch induzierten

Die approbierte gedruckte Originalversion dieser Dissertation ist an der TU Wien Bibliothek verfügbar.
The approved original version of this doctoral thesis is available in print at TU Wien Bibliothek.
TU WIEN Bibliothek Your knowledge hub

Festkörperaustauschreaktion beruht.

Die Lichtabsorption, die Erzeugung von Oberflächenplasmonen und die Detektion der heißen Ladungsträgern, die durch den nicht-strahlenden Zerfall von Oberflächenplasmonen entstehen, werden in einem monolithischen Schottky-Barrieren-Feldeffekttransistor realisiert. Diese ermöglichen es, die effektive Barrierenhöhe an der Metall-Halbleiter-Grenzfläche einzustellen, und damit die plasmoneninduzierte Injektion heißer Ladungsträger zu steuern. Darüber hinaus erfüllen die monolithischen Al-Metallisierung eine Doppelfunktion und leiten gleichzeitig optische und elektrische Signale, was zu interessanten neuen Möglichkeiten führte.

Aluminium wurde verwendet da es CMOS-kompatibel ist und sich aufgrund seines breiten Einsatzspektrums von Ultraviolett bis Infrarot sowie einer selbstbegrenzenden nativen Oxidschicht zum Schutz der Metalloberfläche hervorragend für die Plasmonik eignet.

Für solche Bauelemente wurden einige neuartige physikalische Phänomene im Zusammenhang mit der Dynamik heißer Ladungsträger im Germaniumkanal nachgewiesen, darunter negative Photoleitfähigkeit und Detektoren mit superlinearer Empfindlichkeit. Ein ultraskalierter Prototyp mit einem Ge-Kanal im Submikrometerbereich erwies sichals Hot-Carrier-Photodetektor mit ballistischem Ladungsträgertransport, der eine Bandbreite von 50 GHz bei 1560 nm und Nullvorspannung ermöglicht.

Unter Verwendung eines Al-Si-Al-Bauelements mit Splitgate-Architektur konnte erstmals eine effektive Ladungstrennung der plasmonisch injizierten heißen Ladungsträger demonstriert werden und damit eine Funktion, die mit der eines On-Chip-Photovoltaik-Bauelements vergleichbar ist.

TU Bibliothek WIEN Your knowledge hub
Die approbierte gedruckte Originalversion dieser Dissertation ist an der TU Wien Bibliothek verfügbar.
The approved original version of this doctoral thesis is available in print at TU Wien Bibliothek.

Acknowledgments

I always believe I initially made the correct decision to choose Vienna, making me meet so many friendly and kind people. I would like to express my heartfelt appreciation to these people who gave me help and support throughout my PhD journey. Despite the immense challenges posed by the Covid-19 pandemic, the unconditional support and care from my supervisors, co-workers and project partners built the cornerstone for the success of my research. Therefore, I would like to thank...

Alois Lugstein

for his unconditional support and care in academic research and life. Additionally, I am super grateful to him for offering such an incredible opportunity to study abroad, which definitely alters my life. There are countless reasons to express my gratitude and appreciation towards him. He is someone I greatly admire and look up to as I navigate my future academic path, because of his professionality in science, kindness and humour.

Masiar Sistani, Lukas Wind and Daniele Nazzari

for their kind help with the fabrications and measurements. I would like to appreciate Masiar Sistani for guiding me through all the nanofabrication and measurement processes. I am also grateful to Lukas Wind and Nazzari Daniele for their invaluable assistance in addressing the issue of the fabrication process. It was an absolute delight for me to collaborate with them.

Weber Walter Michael

for providing a foreigner-friendly work environment in the institute.

Werner Schrenk and Markus Schinnerl

for their patient introduction and unconditional support in the cleanroom.

All my colleagues of the FKE and ZMNS

for enriching my life with meaningful conversations and unforgettable moments of joy.

Juraj Darmo

for supporting our joint project on pump-probe cross-correlation measurements. I am also grateful to him for the helpful discussion on plasmonic physics.

Die approbierte gedruckte Originalversion dieser Dissertation ist an der TU Wien Bibliothek verfügbar.
The approved original version of this doctoral thesis is available in print at TU Wien Bibliothek.
TU Bibliothek WIEN Your knowledge hub

My family

for their unconditional understanding of my decisions and unwavering love throughout my life. Their belief in me has been the driving force behind my journey thus far. I am forever grateful for their unconditional love and unwavering support.

My friends in Vienna

for always offering me joy and relaxing time. I am deeply grateful to Qinzheng Li and Zeyu Huang who are my best Chinese friends in Vienna.

Die approbierte gedruckte Originalversion dieser Dissertation ist an der TU Wien Bibliothek verfügbar.
The approved original version of this doctoral thesis is available in print at TU Wien Bibliothek.
TU WIEN Bibliothek Your knowledge hub

Contents

1. Introduction **1**

2. Theory **9**

2.1 Materials 10

2.1.1 Silicon 10

2.1.2 Germanium 12

2.1.3 Aluminum 14

2.2 Carrier transport in semiconductors 16

2.2.1 Semiconductor statistics 16

2.2.2 Dynamics of charge carriers in semiconductors 20

2.2.3 The p-n diode 22

2.2.4 Schottky junction 24

2.3 Light-matter interaction 29

2.3.1 Light-semiconductor interaction 29

2.3.2 Surface plasmons 32

2.4 Optoelectronic sensors 41

2.4.1 Basic photodetection mechanisms 41

2.4.2 Characteristic parameters of photodetectors 42

2.4.3 Internal photoemission 43

3. Experimental techniques **47**

3.1 Device fabrication 48

3.2 Electrical characterization techniques 50

3.2.1 Output measurements 50

3.2.2 Transfer measurements 51

3.2.3 Temperature dependent electrical measurements 51

Die approbierte gedruckte Originalversion dieser Dissertation ist an der TU Wien Bibliothek verfügbar.
The approved original version of this doctoral thesis is available in print at TU Wien Bibliothek.
TU WIEN Bibliothek Your knowledge hub

3.3 Optoelectronic characterization 53
3.3.1 Characterization of photodetectors 53
3.3.2 Scanning photocurrent microscopy technique 53
3.3.3 Pump-probe cross-correlation measurement 54
4. Results and Discussion 59
4.1 Al-Ge-Al heterostructures 60
4.1.1 The formation of Al-Ge-Al heterostructure devices 60
4.1.2 Basic electrical properties of Al-Ge-Al heterostructures 63
4.1.3 Plasmonic applications of Al-Ge-Al heterostructure devices 68
4.2 Al-Si-Al heterostructure 98
4.2.1 The formation of Al-Si-Al heterostructure devices 98
4.2.2 Basic electrical properties of Al-Si-Al heterostructure devices 99
4.2.3 Plasmonic applications of Al-Si-Al heterostructure devices 102
5. Summary and outlook 113
Curriculum Vitae 117
List of figures 121
List of abbreviations 127
List of symbols 129
Bibliography 133

Die approbierte gedruckte Originalversion dieser Dissertation ist an der TU Wien Bibliothek verfügbar.
The approved original version of this doctoral thesis is available in print at TU Wien Bibliothek.
TU WIEN Bibliothek Your knowledge hub

Chapter 1

Introduction

Silicon (Si) based electronics has proceeded with an impressive success of economic and technological advancements, supporting the information age we enjoy today. One of the most important cornerstones thereof are integrated circuits (ICs), enabling the miniaturization and integration of electronic components into a single chip realizing successfully smaller, faster and more functional devices, for instance, computers and mobile phones. The driving force behind the exponential development of ICs is famously known as Moore's law (**Figure 1.1**), introduced by Gordon Moore in 1965, which implies that the number of transistors on a logic chip would double roughly every two years.

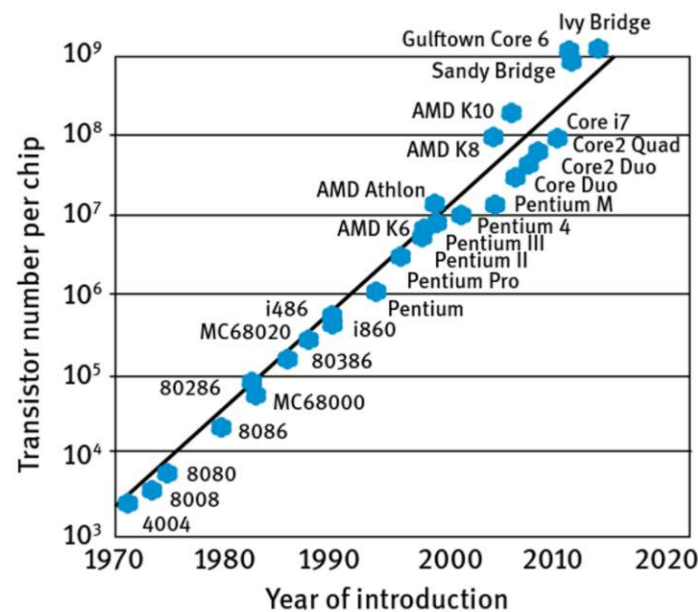

Figure 1.1 The number of transistors in one microprocessor from 1970 to 2020. Image adapted from König K. et al.[1].

Since Si as the basic material of ICs firstly was used in microelectronics in the 1950s, Moore's law has held true for 50 years. In the last decade, the development has slowed down somewhat, as physical limitations become more and more serious. For example, the Apple A14 Bionic is manufactured by TSMC on a 5 nm process node with a transistor count of 11.8 billion (**Figure 1.1**). These transistors are fabricated in FinFET architecture with the gate fully wrapped around

Die approbierte gedruckte Originalversion dieser Dissertation ist an der TU Wien Bibliothek verfügbar.
The approved original version of this doctoral thesis is available in print at TU Wien Bibliothek.
TU WIEN Bibliothek Your knowledge hub

the channel on three sides to minimize short channel effects like leakage current of the gate DIBL(drain induced barrier lowering)[2]. Apart from short channel effects, another challenge which results with scaling is the RC delay of the metal interconnects. **Figure 1.2a** and **b** demonstrate the complexity of metal interconnects comprising multiple stacked layers.

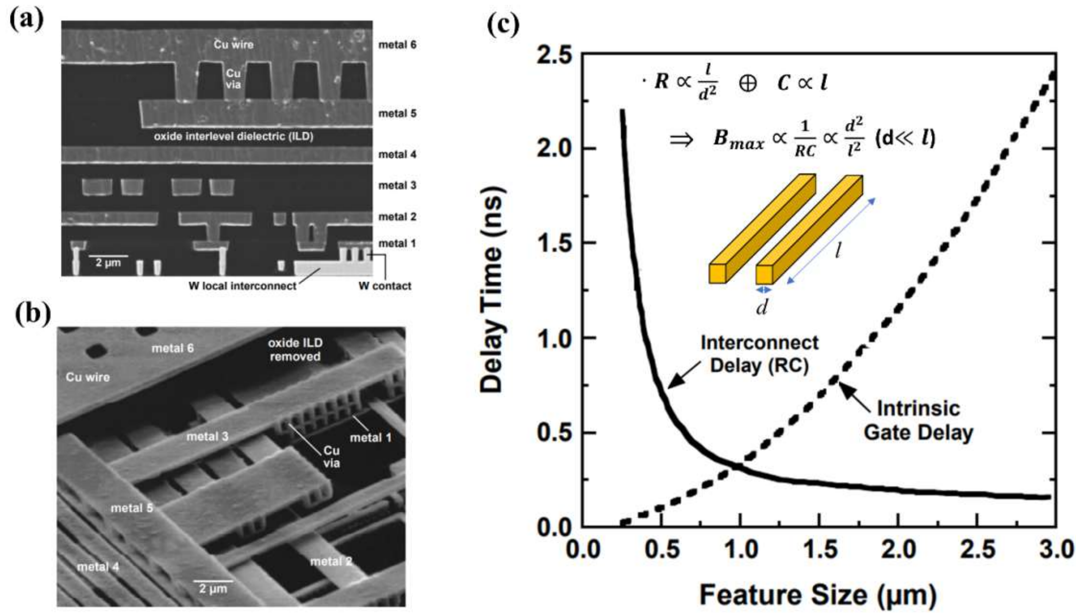

Figure 1.2 Scanning electron microscopy images showing (a) the cross-sectional (adapted from Edelstein D. et al.[3]) and (b) global view of modern ICs interconnect architecture (adapted from Venkatesan S. et al.[4]). (c) Delay time determined by the feature size of interconnect metal wires for transistors. The inset demonstrates the derivation process of the RC delay for thin metal wires. Image adapted from Loke A. et al.[5].

Taking the Apple A7 application processor as an example, the total length of metallization wires would be approximately 20 kilometers if stretching out and measuring all metal wires. Besides, due to the tiny dimensions of transistors, the cross-section of connecting copper wires is also ultra-small. Therefore, according to Ohm law, the resistance for such metal interconnects becomes intrinsically large. In addition, boundary scattering and surface effects are further significant factor to increase the resistance of such thin metal wires. Meanwhile, the capacitance increases as well, because of the reduced spacing between the wires. Consequently, the RC delay of metal interconnects becomes an apparent issue limiting the computing speed of advanced microchips, counteracting the scaling to enhance the operating speed (**Figure 1.2c**).

One of the promising alternatives to metal interconnects are optical interconnects, which

Die approbierte gedruckte Originalversion dieser Dissertation ist an der TU Wien Bibliothek verfügbar.
The approved original version of this doctoral thesis is available in print at TU Wien Bibliothek.
TU Bibliothek Your knowledge hub WIEN

typically consists of a laser, a modulator, a waveguide, and a photodetector, as well as some electrical circuits for encoding and decoding the signal. The transmitter comprised of a laser and a modulator emits the coded optical signal. The waveguide transports such signal, and finally the photodetector acts as the receiver converting the optical signal to the electrical one, which can then be decoded by the electrical circuit[6]. Compared to metal interconnects, optical interconnects carry out potential advantages in bandwidth, and power consumption for global signaling. However, the main challenge for miniaturizing optical components results due to the diffraction limit of light, which prohibits confinement of electromagnetic waves below the wavelength in the material. For instance, the smallest dimension of the Si waveguide should not be below 200 nm (i.e. $\lambda/2n \sim 200$ nm with $n = 3.5$ at $\lambda = 1550$ nm) for guiding infrared light in the C-band region. Therefore, using optical interconnects would result in a large footprint of individual optical components and a low integration level, which is far behind the advance of modern electronics. Also due to this trade-off between footprint and performance, shrinking the dimension of CMOS image sensors below the sub-micrometer region challenges. Consequently, there are great efforts to combine the desirable compactness of electronics with the remarkable bandwidth of photonics. **Figure 1.3** demonstrates the relationship between critical dimensions and the operating speed for different interconnect techniques, including electrical, optical and plasmonic ones.

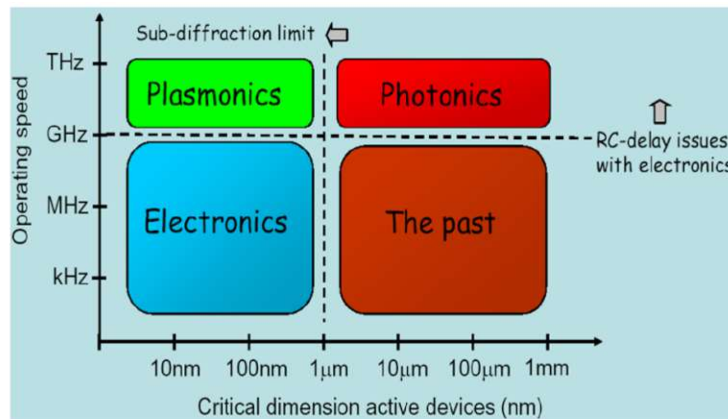

Figure 1.3 The comparison of various interconnect methods with respect to device size and operating speed. Image adapted from Zia R. et al.[7].

Although incredible improvements have been realized in terms of integration density, electronics still suffer from the RC-delay issue, causing extreme challenges for manufacturing ICs surpassing an operation speed >10 GHz. As discussed before, photonic networks feature

TU WIEN Bibliothek Your knowledge hub
Die approbierte gedruckte Originalversion dieser Dissertation ist an der TU Wien Bibliothek verfügbar.
The approved original version of this doctoral thesis is available in print at TU Wien Bibliothek.

large footprints originating from the diffraction limit of light, despite they have high bandwidth. Clearly, plasmonics is regarded as one cutting-edge technology with the potential to surmount the speed-footprint trade-off, thereby becoming the next-generation chip-scale technology. Surface plasmons are denoted as collective oscillations of electrons propagating on the surface of metallic nanostructures responding to incident electromagnetic waves. Generally, via this technology, visible and even infrared light can be confined to several nanometers, and the limitation lies in the crystal structure of the metal and the dispersion of the incident electromagnetic waves.

Owing to the potential to increase the operation speed and keeping the advance of the compact footprint, the application of plasmonics for ICs has gained enormous research interests, accompanied by the rapid developments of related on-chip components (**Figure 1.4**).

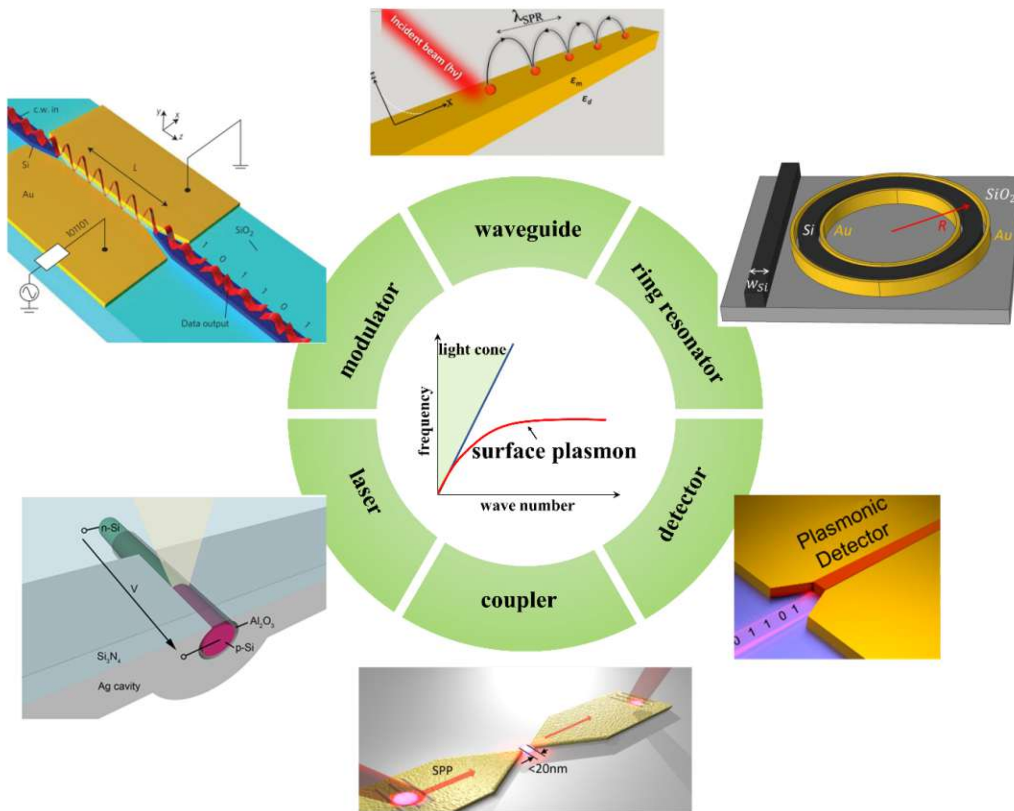

Figure 1.4 Various plasmonic devices expanding the field of silicon technology. Images for light emitter[8], modulator[9], waveguide[10], ring resonator[11], detector[12] and coupler[13] are adapted from the respective literatures.

Following the former route of on-chip optical networks, plasmon-based light emitter[8], modulators[9], waveguides[10], ring resonators[11], detectors[12], and couplers[13], have

Die approbierte gedruckte Originalversion dieser Dissertation ist an der TU Wien Bibliothek verfügbar.
The approved original version of this doctoral thesis is available in print at TU Wien Bibliothek.
TU WIEN Bibliothek Your knowledge hub

been explored, preparing the basis for future optoelectronic ICs. The plasmonic function in the essential components shall be briefly described here

(i) Light emitter: Si is an extremely ineffective light emitter due to the indirection bandgap. A plasmon cavity can efficiently increase the phonon-assisted recombination of hot carriers enabling effective luminescence of Si-based diodes.

(ii) Modulator: The phase or magnitude of a surface plasmon polariton (SPP) has been effectively modulated by employing the thermo-optic effect[14], the Pockels effect[15] or the plasma dispersion effect[16], enabling high-speed, ultra-compact and power efficient electro-optic modulation.

(iii) Waveguide: In order to facilitate SPPs' propagation over a substantial distance, the geometry of surface plasmonic waveguide requires a proper design, due to the trade-off between confinement and propagation length.

(iv) Ring resonator. The aim of integrating a plasmon ring resonator on the chip is to select the SPP of the resonant wavelength and simultaneously amplify its intensity, due to constructive interference enabled by the geometry of the closed loop.

(v) Detector: A plasmonic structure can enhance the light absorption in semiconductors due to its capacity to concentrate light[17]. A further very sensitive type of plasmon assited photodetector, utilizes hot carriers originating from the non-radiative decay of SPPs[18].

(vi) Coupler: A well designed antenna enables the effective conversion of photonic modes to SPPs at the target wavelength[19].

This thesis will mainly focus on the plasmon coupler and waveguide as well as plasmon assisted photodetection. The schematic in **Figure 1.5** illustrates the fundamental structure of a plasmonic Al-semiconductor-Al heterostructure device, employing oval trenches, Al feed lines, and a group-IV semiconductor (i.e. Si or Ge) segment acting as plasmon coupler, SPP waveguides, and plasmon photodetector, respectively.

Aluminum (Al) have been chosen as it is CMOS compatible and is excellent for plasmonics, because of its broad response spectrum from ultraviolet to infrared[20], and a self-limiting native oxide layer protecting the metal surface. Due to their ubiquity in electronics, Si and Ge were selected as the active base materials of the proposed plasmonic on-chip heterostructure devices. Current Si-based ICs technology already uses nanoscale metallic structures, such as Al interconnects[21], to route electronic signals between transistors on a chip. This mature processing technology can thus be used for integrating plasmonic devices with their electronic and dielectric photonic counterparts.

TU Bibliothek Your knowledge hub WIEN
Die approbierte gedruckte Originalversion dieser Dissertation ist an der TU Wien Bibliothek verfügbar.
The approved original version of this doctoral thesis is available in print at TU Wien Bibliothek.

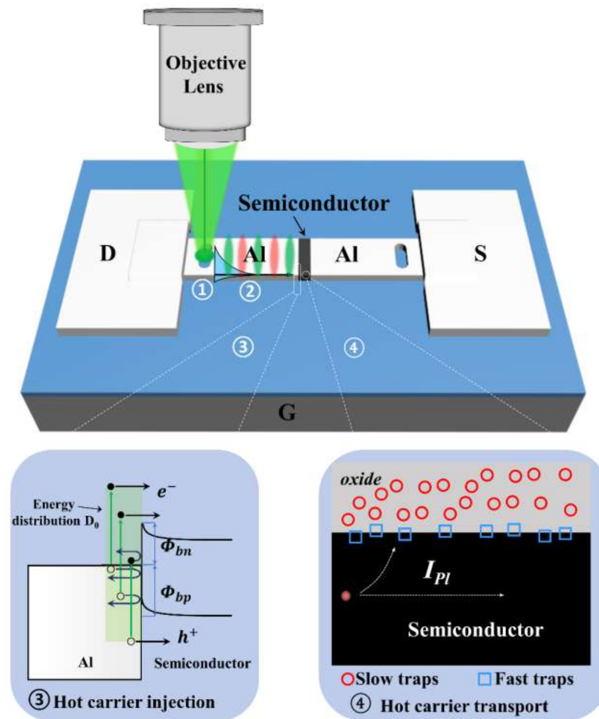

Figure 1.5 Schematic of a monolithic plasmon device assembled by two plasmon trenches and Al-Semiconductor-Al heterostructure. The whole hot-carrier photodetection process is comprised of four main steps: ① the generation of SPPs at the plasmon trench, ② the propagation of SPPs along the Al feed line, ③ the injection of hot carriers at the Al/semiconductor interface and ④ the transport of hot carriers inside the semiconductor channel.

Furthermore, on account of momentum matching, a monolithic metal-semiconductor-metal device architecture is employed. Due to the different dielectric constants between the metal and the semiconductor in momentum space, only charge carriers in a limited escape cone can be injected into the semiconductor segment[22]. Compared to most common structures in which metal pads are deposited atop of the semiconductor segment, a well-aligned interface apparently provides a broader escape cone for hot-carrier injection.

The aim of this PhD thesis is to investigate and understand the fundamental mechanism of plasmon-induced hot-carrier generation and detection. The ultimate goal is to realize a compact and ultra-fast plasmon and/or photodetector. The studies are undertaken in a spatial sequence, that is, the generation of SPPs at a plasmon coupler, the propagation of SPPs along the Al feed line, the injection of hot carriers at the metal/semiconductor interface and their transport dynamics inside the semiconductor channel. Finally, ultra-fast response is realized by a compact device with the channel length of less than 100 nm following ballistic transport.

TU Bibliothek WIEN Your knowledge hub
Die approbierte gedruckte Originalversion dieser Dissertation ist an der TU Wien Bibliothek verfügbar.
The approved original version of this doctoral thesis is available in print at TU Wien Bibliothek.

In chapter 2, some related background knowledges, including the basic properties of used semiconductors and carrier transport, are introduced. Further, the theory of light-matter interaction as well as the working principle of common semiconductor photodetectors and hot-carrier detectors are discussed. In chapter 3, the main device fabrication steps as well as measurement procedures are described. In chapter 4, the experimental results are discussed. In particular, firstly the advance in the manufacturing of the plasmon coupler by a thermal induced solid phase reaction is introduced. Following that, the monolithic Al waveguide is characterized. Subsequently, some novel phenomena in terms of transport dynamics, including photogating effect, superlinear photo-electronic scheme and the selective injection of hot electrons/holes, are investigated. The picosecond kinetics of the overall plasmon system is studied by a modified pump-probe cross-correlation method.

Die approbierte gedruckte Originalversion dieser Dissertation ist an der TU Wien Bibliothek verfügbar.
The approved original version of this doctoral thesis is available in print at TU Wien Bibliothek.
TU WIEN Bibliothek Your knowledge hub

Die approbierte gedruckte Originalversion dieser Dissertation ist an der TU Wien Bibliothek verfügbar.
The approved original version of this doctoral thesis is available in print at TU Wien Bibliothek.
TU WIEN Bibliothek Your knowledge hub

Chapter 2

Theory

This chapter carries out a comprehensive discussion about the theoretical background for this thesis. It involves material properties, theory of carrier transport in semiconductors, light-matter interaction and particular optoelectronic device. The first part provides a brief introduction about the basic properties of Si, Ge and Al. Afterward, the subsequent one discusses the transport dynamics of charge carriers moving inside semiconductors, as well as crossing the p-n junction or the Schottky junction. Further, light-matter interaction is introduced, involving light-semiconductor and light-metal interaction. The final section exhibits the working mechanism of a conventional semiconductor photodetector and the plasmon-induced hot-carrier photodetector.

Die approbierte gedruckte Originalversion dieser Dissertation ist an der TU Wien Bibliothek verfügbar.
The approved original version of this doctoral thesis is available in print at TU Wien Bibliothek.
TU Wien Bibliothek Your knowledge hub

2.1 Materials

2.1.1 Silicon

The 21st century also has been denoted as the Si age, owing to the massive contribution of elemental Si to the modern world economy. Si is particularly one of the most important materials in the ICs industry, originally also due to the excellent properties of silicon dioxide (SiO_2) which serves as a perfect insulator, passivating dangling bonds at the semiconductor-oxide interface. In the earth's crust Si is the second most abundant element by mass, although the pure element rarely occurs. However, through distillation techniques and using a float zone or Czochralski process[23], Si can be purified and single crystalline up to 12-inch wafers can routinely be fabricated.

Si is an element of the fourth main group and is located at the 14th position in the periodic table of elements. Therefore, a Si atom with four valence electrons generally connects to other atoms by four covalent bonds. **Figure 2.1** illustrates the main polytype of Si crystalline structure in the cubic diamond lattice.

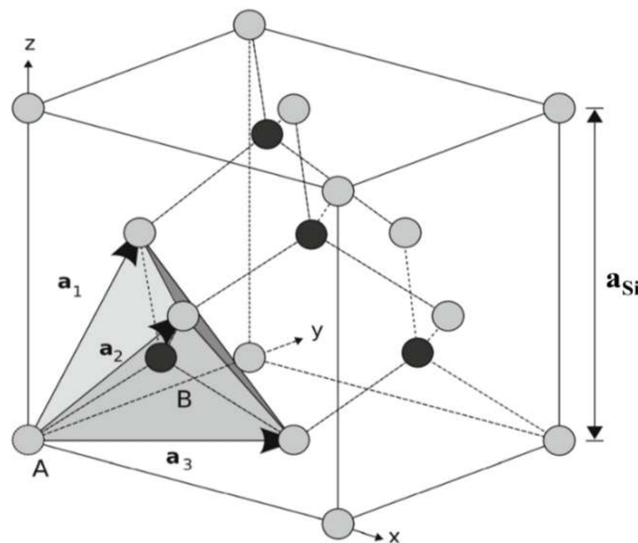

Figure 2.1 Schematic of the diamond cubic lattice structure of Si, which can be considered as two intersected face-centered cubic (FCC) lattices compositing atoms A (grey) and B (black). The primitive cell is built by the fundamental vectors $\vec{a}_1$, $\vec{a}_2$ and $\vec{a}_3$ with a_{Si} = 0.543 nm. Image adapted from Glassner S.[24].

Die approbierte gedruckte Originalversion dieser Dissertation ist an der TU Wien Bibliothek verfügbar.
The approved original version of this doctoral thesis is available in print at TU Wien Bibliothek.
TU Bibliothek WIEN Your knowledge hub

The fundamental vectors in the cubic diamond lattice are defined as

$$\vec{a}_1 = \frac{a_0}{2}\begin{pmatrix}0\\1\\1\end{pmatrix}, \quad \vec{a}_2 = \frac{a_0}{2}\begin{pmatrix}1\\0\\1\end{pmatrix} \text{ and } \vec{a}_3 = \frac{a_0}{2}\begin{pmatrix}1\\1\\0\end{pmatrix} \tag{2.1}$$

Thereby, any lattice point can be expressed by the linear combination of the fundamental vectors

$$\vec{a} = i \cdot \vec{a}_1 + j \cdot \vec{a}_2 + k \cdot \vec{a}_3 \tag{2.2}$$

The Brillouin zones are defined as the elementary cell of the reciprocal lattice, wherein the corresponding fundamental vectors $\vec{b}_1$, $\vec{b}_2$ and $\vec{b}_3$ can be derived from that of the unit cell $\vec{a}$

$$\vec{B}_i = 2\pi \frac{\vec{a}_j \times \vec{a}_k}{(\vec{a}_1 \times \vec{a}_2) \cdot \vec{a}_3} \tag{2.3}$$

with the indicators i, j, k being affected by cyclic rotation. The first Brillouin zone of Si contains the six equivalent ellipsoids corresponding to the degenerate conduction band minima which positions along the Δ lines (see **Figure 2.2a**). **Figure 2.2b** illustrates important lines and directions in one quadrant of the first Brillouin zone. The Δ line indicates the direction from the zone origin point Γ towards the boundary point X.

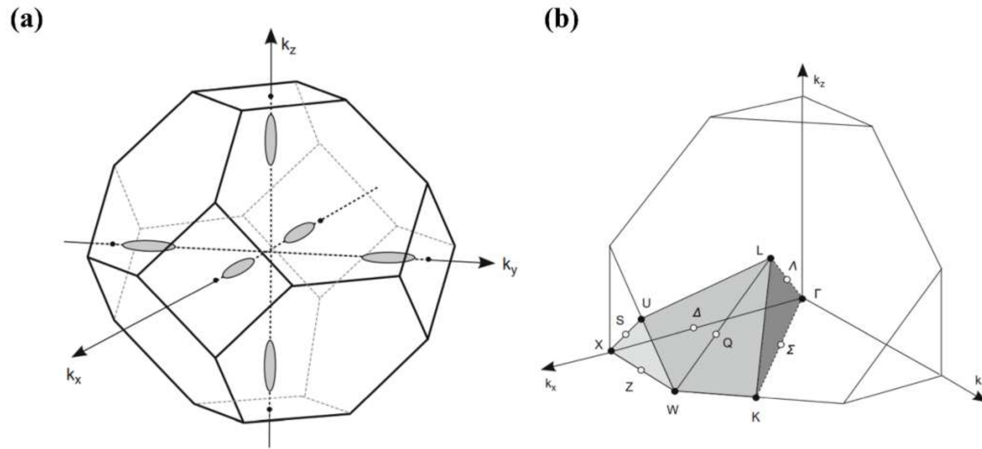

Figure 2.2 (a) The first Brillouin zone of Si involving 14 faces. (b) One quadrant of the first Brillouin zone. The origin of the coordinate system situates at the Γ-point. The center of the square and hexagonal faces locates at the X and L points, respectively. The direction from Γ towards X, L and K is represented by the lines Δ, Λ and Σ, respectively. Image adapted from Glassner S.[24].

If the wave vector $\vec{k}$ of electrons in the conduction band is equal to that of holes in the valence band, the band gap thereof is referred to as a direct one. By contrast, indirect bandgap semiconductors manifest in different wave vectors $\vec{k}$, and Si is the typical one with the bandgap

Die approbierte gedruckte Originalversion dieser Dissertation ist an der TU Wien Bibliothek verfügbar.
The approved original version of this doctoral thesis is available in print at TU Wien Bibliothek.
TU WIEN Bibliothek Your knowledge hub

of E_g = 1.12 eV at room temperature derived from the maximum of the valence band at the Γ-point to the minimum of the conduction band close to the X-point. The gap decreases with increasing temperature following

$$\Delta E_g = -\frac{\alpha \cdot T^2}{T+\beta} \tag{2.4}$$

with material specific parameters of α = 4.9 × 10^{-4} eV/K and β = 655 eV/K for Si. **Figure 2.3** depicts the corresponding band structure of Si.

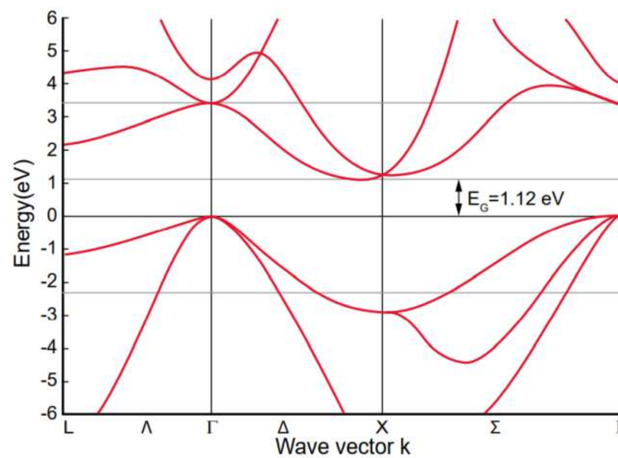

Figure 2.3 Band structure of Si with the band gap of E_g = 1.12 eV. Image adapted from Glassner S.[24].

Bulk Si commonly features a six-fold degenerate conduction band with the minimum located around the X-point. Furthermore, the second minimum exactly positions at the X-point with an energy difference of only 0.1 eV, compared to the first minimum. But the maximum of the valence band is at the Γ-point, resulting in an indirect gap of E_g = 1.12 eV. Nevertheless, the corresponding direct gap at the Γ-point is 3.4 eV, which apparently exceeds the indirect gap by far.

2.1.2 Germanium

Ge is also an indirect bandgap group IV semiconductor located at the 32nd position in the periodic table of elements, and its melting- and boiling points are at 1211 K and 3107 K, respectively. Ge occurs mainly in mineral compounds such as argyrodite or germanite. Similar to Si, Ge crystallizes in a diamond lattice as well, with a lattice constant of a_{Ge} = 0.566 nm, as shown in **Figure 2.4(a)**.

Die approbierte gedruckte Originalversion dieser Dissertation ist an der TU Wien Bibliothek verfügbar.
The approved original version of this doctoral thesis is available in print at TU Wien Bibliothek.
TU Bibliothek WIEN Your knowledge hub

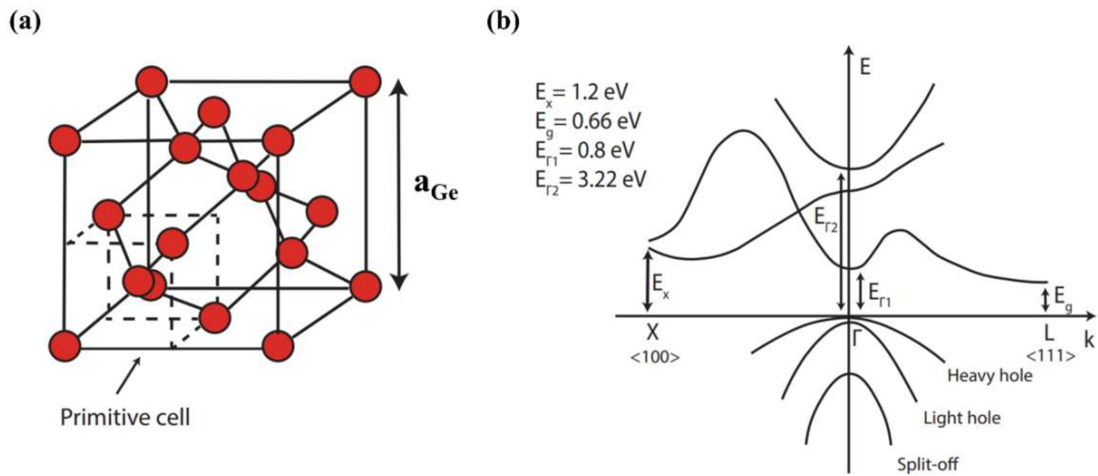

Figure 2.4 (a) Schematic of the Ge diamond lattice structure with the lattice constant of a_{Ge} = 0.566 nm. (b) Band structure demonstrates that Ge is an indirect band gap with E_g = 0.66 eV. Image adapted from Bartmann M. G.[25].

Figure 2.4(b) demonstrates the band diagram of Ge at room temperature, with an indirect bandgap of E_g = 0.66 eV at the L-point minimum and a direct bandgap of E_Γ = 0.8 eV located at the Γ-point. Due to the small difference between the two bandgaps, alloying with Sn or applying high tensile strain in suspended Ge structures can enable the transition of Ge to a direct bandgap semiconductor enabling even Ge based laser[26,27]. Compared to Si, Ge has larger carrier mobilities (i.e. μ_n = 3800 $cm^2 \cdot V^{-1} \cdot s^{-1}$ for electrons and μ_p = 1820 $cm^2 \cdot V^{-1} \cdot s^{-1}$ for holes). The first transistor fabricated by Shockley Bardeen and Brattain in 1947 was based on Ge. However, in the past decades Ge was not as widely used as Si in the transistor industry. The main reason is the high quality of the silicon oxide, compared to Ge, that serves as a good insulator and naturally passivates dangling bonds at the semiconductor-oxide interface. The species of germanium oxide are much numerous and complex including Ge dioxide (GeO_2), Ge monoxide (GeO), Ge_2O_3 and Ge_2O[28]. It was verified that the electrical properties of the interface for Ge are mainly determined by the composition of these sub-oxides. Many strategies have been provided to achieve a high-quality GeO_2/Ge interface, as the GeO_2 performs higher quality to reduce surface trapping[29]. The surface states can be classified mainly into two groups with respect to the detrapping time: fast surface states and slow surface states (**Figure 2.5**). The empty surface states are neutral and may capture electrons, thus the filled traps become negatively charged. Fast surface states are situated near the interface between GeO_x and bulk Ge, which can easily be filled by electrons and the detrapping time is in the scale of

Die approbierte gedruckte Originalversion dieser Dissertation ist an der TU Wien Bibliothek verfügbar.
The approved original version of this doctoral thesis is available in print at TU Wien Bibliothek.
TU WIEN Bibliothek Your knowledge hub

microseconds[28]. The slow surface traps inside the germanium oxide GeO_x require a tunneling-assisted process to capture electrons. Therefore, the detrapping time of electrons re-emitted from the slow surface states can be up to minutes[28].

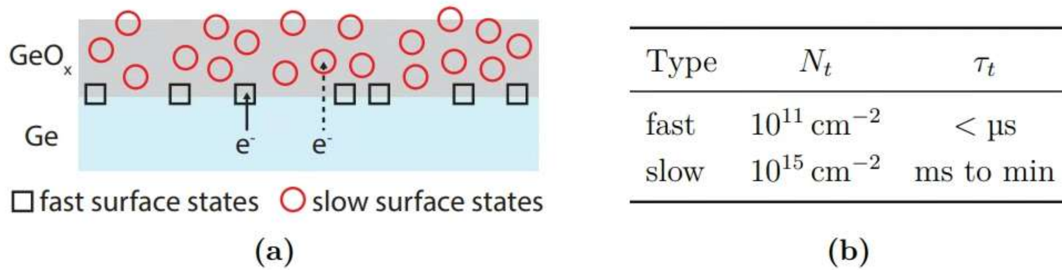

Type	N_t	τ_t
fast	$10^{11}\,\mathrm{cm}^{-2}$	$<$ µs
slow	$10^{15}\,\mathrm{cm}^{-2}$	ms to min

Figure 2.5 (a) Schematic diagram with respect to the surface traps of Ge. (b) A comparison of the density and detrapping time τ_t for fast and slow surface traps. Image adapted from Staudinger P.[30].

Nevertheless, as for the sub-45 nm technology nodes high-k dielectrics were employed as gate-oxides, and the advantage of a high-quality oxide was no longer crucial, making Ge a promising candidate for future high-performance transistors again. Moreover, Ge can be employed as a material for different optical systems in the infrared region such as infrared (IR) spectrometers[31]. Further, germanium oxides are applied for the fabrication of wide-angle camera lenses and microscope objectives due to a high index of reflection and dispersion. Besides, due to the high absorption coefficient of Ge in the wavelength range between 800 nm and 1550 nm, it is an interesting candidate for optoelectronic applications, especially for IR photodetectors[32] as well as efficient IR absorbers for tandem solar cells[33].

2.1.3 Aluminum

Al is a metal located at the 13th position in group III of the periodic table of elements with melting- and boiling points at 933 K and 2790 K, respectively. Al crystallizes in the FCC lattice with a lattice constant of a_{Al} = 0.405 nm (see **Figure 2.6a**). It is clearly seen in **Figure 2.6b** that no band gap inducts for Al with the minimum of the conduction band being lower than the maximum of the valence band. Elemental Al does not occur in nature due to the high chemical reactivity, although it is the most abundant metallic element in the earth's crust. Hence it always occurs in compounds, for example, feldspar, bauxite core or granite. Nowadays, Al with approximately 99.99% purity is extracted from the ore bauxite by energy-intensive electrolysis.

TU Bibliothek WIEN Your knowledge hub
Die approbierte gedruckte Originalversion dieser Dissertation ist an der TU Wien Bibliothek verfügbar.
The approved original version of this doctoral thesis is available in print at TU Wien Bibliothek.

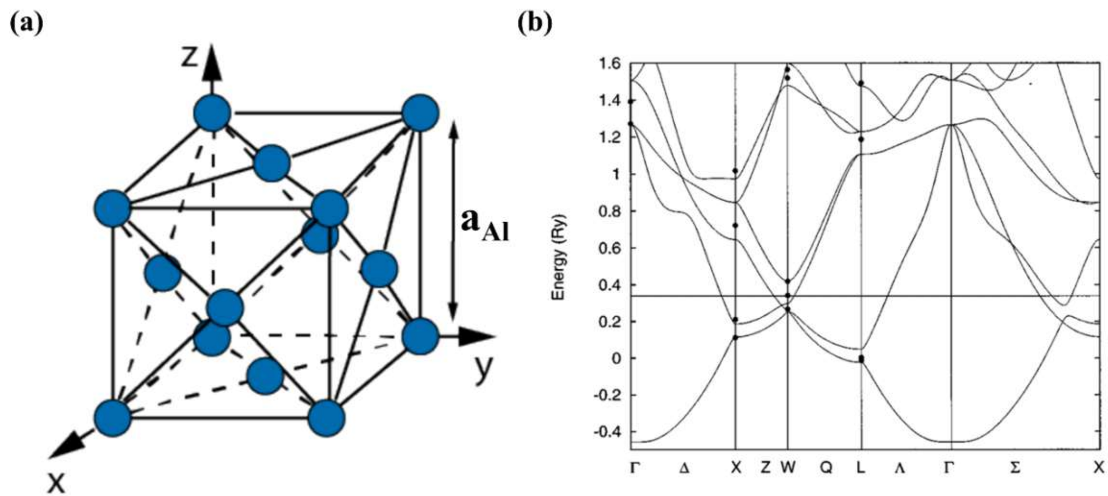

Figure 2.6 (a) The primitive unit cell of Al crystallinity in the FCC lattice structure. Adapted from Sistani M.[34]. (b) Band structure of Al. Adapted from Yang S. H. et al.[35].

Al exhibits excellent electrical and mechanical properties, including an electrical conductivity of approximately 36 mS·mm^{-2} as well as Young's modulus of 69 GPa. At present Al is the second most widely used metal in industrial production, although only started to be commercially produced in 1886. Further, owing to a suitable work function of 4.1 eV, Al is a promising candidate for electrodes and integrated transducers. In the modern microelectronic industry, Al is widely applied as metallization and interconnect material. But Al was replaced by Cu as the preferred interconnect metal in 1997, since unacceptable electromigration in Al interconnects occurs at high current densities. As Al becomes superconducting at a bulk transition temperature of $T_c = 1.19\,K$ and has a high-quality native oxide (Al_2O_3), it has a wide variety of applications in quantum research for resonators or superconducting qubits.

Die approbierte gedruckte Originalversion dieser Dissertation ist an der TU Wien Bibliothek verfügbar.
The approved original version of this doctoral thesis is available in print at TU Wien Bibliothek.
TU WIEN Bibliothek Your knowledge hub

2.2 Carrier transport in semiconductors

2.2.1 Semiconductor statistics

One simple one-dimensional crystal model comprising atoms in the number of N is considered. Additionally, the distance between two adjacent atoms is rather compact, thus allowing their orbitals to interact. If N = 2, two individual atom orbitals will overleap, resulting in two new energy states, a so-called bonding (the lower energy one) and an antibonding (the higher energy one). For N = 3, it produces a bonding, a non-bonding as well as an anti-bonding orbital. In principle, the combination of N atom orbitals enables N discrete energy states. In this view, if N is very large, a quasi continuum of orbitals forms, referred to as the band. In bulk materials, the number of atoms is as high as 6.022×10^{23} per mole. The band resembled by bonding and anti-bonding combinations is called the valence band and conduction band, respectively. Depending on the forbidden gap between the valence band and conduction band, referred to as the bandgap, solid materials can be categorized into three types: metals, insulators and semiconductors, as depicted in **Figure 2.7**.

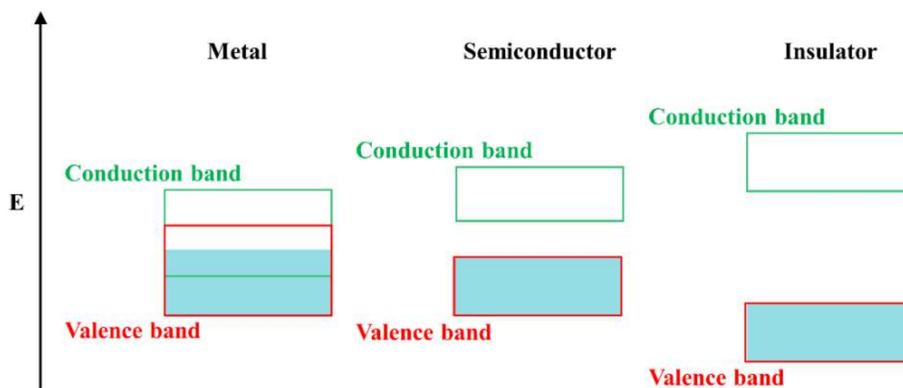

Figure 2.7 Band diagrams of a metal, a semiconductor and an insulator. The blue color marks the states filled by electrons. Image adapted from Bartmann M. G.[25].

Metals feature no bandgap (i.e. the conduction band overlaps with the valence band), allowing electrons to move freely, thereby enabling excellent conductivity. In contrast, the large bandgap of the insulator blocks the transition of electrons from the valence band to the conduction band, resulting in an extremely high resistivity. Compared to the insulator, the semiconductor owns a smaller bandgap that allows the band-to-band transition even at room temperature. Electrons are excited to the conduction band, accompanied by some holes left on the valence band. At 0 K there is no conduction in semiconductors. Nevertheless, at higher temperatures some

Die approbierte gedruckte Originalversion dieser Dissertation ist an der TU Wien Bibliothek verfügbar.
The approved original version of this doctoral thesis is available in print at TU Wien Bibliothek.
TU WIEN Bibliothek Your knowledge hub

electrons can be excited to the conduction band due to the thermal excitation, thus resulting in some current flowing in the semiconductor.

In the band structure of semiconductors, the band curvature further reflects the effective mass and is thus a measure of the charge carrier mobility. The parabolic approximation simply describes the energy dispersion relation E(k) near the conduction band minimum

$$\mathrm{E(k)} = \mathrm{E_c} + \frac{\hbar^2 k^2}{2m_e^*} \tag{2.5}$$

where $\mathrm{E_c}$ is the conduction band minimum, $\hbar$ is the Dirac constant and m_e^* denotes the effective mass of electrons.

On account of the motion within the crystal lattice, the equation of the effective mass can be rewritten

$$\frac{1}{m^*} = \frac{1}{\hbar^2}\frac{\partial^2 E}{\partial k^2} \tag{2.6}$$

Therefore, the effective mass is inversely proportional to the curvature of the conduction band. For an isotropic semiconductor the Drude model describes the movement of charge carriers driven by an external electric field ($\mathrm{E_{ext}}$) against frictional forces originating from scattering. The corresponding effective mass can be regarded as a scalar instead of a tensor. For an isotropic semiconductor the average relaxation time can be applied to characterize scattering losses. Therefore, the movement of charge carriers under an external field can be described as

$$m^* \frac{\partial v}{\partial t} + m^* \frac{v}{\tau_m} = \mathrm{qE_{ext}} \tag{2.7}$$

with v the average drift velocity, q the elementary charge and τ_m the mean scattering time of charge carriers. In the steady state ($\frac{\partial v}{\partial t} = 0$), the drift velocity can be derived via

$$v = \frac{q\tau_m}{m^*}\mathrm{E_{ext}} = \mu \mathrm{E_{ext}} \tag{2.8}$$

with μ the mobility, which is given by

$$\mu = \frac{q\tau_m}{m^*} \tag{2.9}$$

A stronger band curvature indicates a smaller effective mass, resulting in a higher mobility. Literatures have reported the mobility of electrons and holes for intrinsic silicon are 1400 and 450 $\mathrm{cm^2 \cdot V^{-1} \cdot s^{-1}}$, respectively[36].

Furthermore, the relationship between the density of states g(E) and the effective mass can be expressed as[37]

$$g(E) \equiv \frac{dn}{dE} = \frac{dn}{dk}\frac{dk}{dE} = \frac{1}{2\pi^2}\left(\frac{2m^*}{\hbar^2}\right)^{\frac{3}{2}} (E - E_0)^{\frac{1}{2}} \tag{2.10}$$

Die approbierte gedruckte Originalversion dieser Dissertation ist an der TU Wien Bibliothek verfügbar.
The approved original version of this doctoral thesis is available in print at TU Wien Bibliothek.
TU WIEN Bibliothek Your knowledge hub

The equation apparently illustrates that a heavier effective mass corresponds to a larger density of states. In other words, a stronger band curvature suggests a smaller effective mass, hence a smaller density of states.

For an intrinsic semiconductor, the electron density is given by

$$n = \int_{E_C}^{\infty} g(E) \cdot f(E)\, dE \qquad (2.11)$$

with *g(E)* the density of states (see **Eq. 2.10**) and *f(E)* the Fermi-Dirac distribution. Similarly, the hole density is given by

$$p = \int_{-\infty}^{E_V} g(E) \cdot (1 - f(E))\, dE \qquad (2.12)$$

For non-degenerate semiconductors, the Fermi-Dirac distribution *f(E)* can be simplified via the Maxwell-Boltzmann approximation

$$f(E) \approx exp(-\frac{E}{kT}) \cdot exp(\frac{E_F}{kT}) \qquad (2.13)$$

with E_F the Fermi level. Further, the electron density in the conduction band can be derived as

$$n = \int_{E_C}^{\infty} g(E) \cdot f(E)\, dE \approx N_C \cdot exp\left(-\frac{E_C - E_F}{kT}\right) \qquad (2.14)$$

with N_C the effective density of states in the conduction band, given by

$$N_c = \frac{2}{h^3}(2\pi m_e^* kT)^{\frac{3}{2}} \qquad (2.15)$$

with m_e^* the effective mass for electrons. The hole density in the valence band is given by

$$p = \int_{-\infty}^{E_V} g(E) \cdot (1 - f(E))\, dE \approx N_V \cdot exp\left(\frac{E_V - E_F}{kT}\right) \qquad (2.16)$$

with N_V the effective density of states in the valence band, expressed as

$$N_V = \frac{2}{h^3}(2\pi m_h^* kT)^{\frac{3}{2}} \qquad (2.17)$$

with m_h^* the effective mass for holes. Consequently, for the intrinsic semiconductor, in which the electron density is equal to the hole density, the carrier density in thermal equilibrium becomes

$$pn = N_C N_V \exp\left(-\frac{E_g}{kT}\right) = n_i^2 \qquad (2.18)$$

where n_i denotes an intrinsic carrier concentration. This relationship is famously known as the mass-action law. And the resulting Fermi level situates at the middle of the bandgap, as illustrated in **Figure 2.8a**.

Die approbierte gedruckte Originalversion dieser Dissertation ist an der TU Wien Bibliothek verfügbar.
The approved original version of this doctoral thesis is available in print at TU Wien Bibliothek.
TU Bibliothek WIEN Your knowledge hub

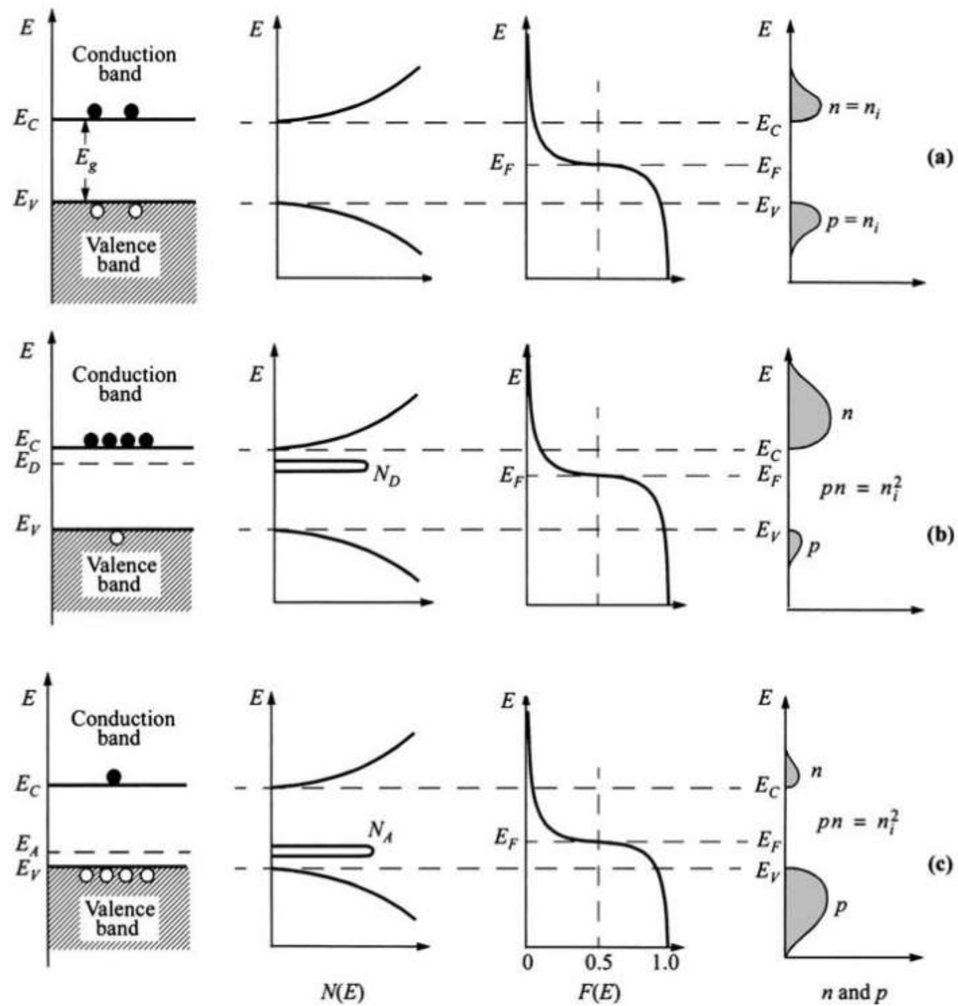

Figure 2.8 Schematic illustration of bandgap diagram, density of states, Fermi-Dirac distribution and carrier concentration for (a) intrinsic, (b) n-type, and (c) p-type semiconductor. Figures adapted from Sze S. M. et al.[37].

Aside from the intrinsic semiconductor, impurity doping enables well-controlled modulation of the electrical properties. Taking Si as an example, typical n-type and p-type dopants are phosphorus and boron, referred to as the donor and acceptor dopants, consequently resulting in electrons or holes as the majority charges, respectively. **Figure 2.8b** demonstrates that the donor level E_D of an n-type semiconductor is close to the conduction band edge and the corresponding Fermi level positions also close to the conduction band. The situation is opposite for the p-type semiconductor, in which the acceptor level situates near the valence band and the resulting Fermi level locates close to the valence band, as shown in **Figure 2.8c**.

Die approbierte gedruckte Originalversion dieser Dissertation ist an der TU Wien Bibliothek verfügbar.
The approved original version of this doctoral thesis is available in print at TU Wien Bibliothek.
TU Wien Bibliothek Your knowledge hub

Introducing E_i (i.e. the intrinsic level of an intrinsic semiconductor) as a reference energy level, the electron density is given by

$$n = n_i \exp\left(\frac{E_F - E_i}{kT}\right) \quad \text{or} \quad E_F - E_i = kTln\left(\frac{n}{n_i}\right) \tag{2.19}$$

and for p-type materials

$$p = n_i \exp\left(\frac{E_i - E_F}{kT}\right) \quad \text{or} \quad E_i - E_F = kTln\left(\frac{p}{n_i}\right) \tag{2.20}$$

Further, the occupancy function can be written as

$$N_C \exp\left(-\frac{E_C - E_F}{kT}\right) \approx \frac{N_D}{1 + 2\exp\left[\frac{(E_F - E_D)}{kT}\right]} \tag{2.21}$$

Therefore, the position of the Fermi level can be precisely calculated (e.g. $E_F = E_C - kTln(N_C/N_D)$ for an n-type semiconductor using N_D, E_D, N_C, and T. Further, the related carrier density n can be derived. A similar derivation process can be applied to analyse the respective position of Fermi level and hole density in a p-type semiconductor as well.

2.2.2 Dynamics of charge carriers in semiconductors

For moderate electric fields (i.e. applying a low external bias to a semiconductor), charge carriers are accelerated by the electric field force with a strength E_{ext} up to a steady state velocity. This electric-driven movement of charge carriers is called drift, following **E.q. 2.8**. The charge carriers are further subject to phonon and impurity scattering inside nonpolar semiconductors (e.g. Ge and Si). In this view, the mobility μ is also determined by the mean scattering time τ_m or mean free path ℓ, given by

$$\mu = \frac{q\tau_m}{m^*} = \frac{q\ell}{m^*\vartheta_{th}} \tag{2.22}$$

where m^* is the effective mass of the charge carriers, ϑ_{th} is the thermal velocity following the relationship $\ell = \vartheta_{th}\tau_m$. Generally, assuming that most shallow impurities are ionized at room temperature, the mobility decreases at higher impurity concentrations and higher temperatures, supported by other reports[38,39]. Generally, intrinsic Si or Ge demonstrates higher mobility of electrons than that of holes, as holes typically have a larger effective mass.

Aside from drift, diffusion is another essential behavior of charge carriers, directly triggered by a carrier concentration gradient. With the hypothesis that excess carriers are generated or injected locally (e.g. injection of carriers from a junction or nonuniform illumination), the carriers always migrate from the region of high concentration toward the lower one, in order to equalize carrier concentration gradients.

Die approbierte gedruckte Originalversion dieser Dissertation ist an der TU Wien Bibliothek verfügbar.
The approved original version of this doctoral thesis is available in print at TU Wien Bibliothek.
TU WIEN Bibliothek Your knowledge hub

According to Fick's law, the flow of carriers in the diffusion process can be quantitatively described as

$$\left.\frac{dn}{dt}\right|_x = -D_n \frac{dn}{dx} \tag{2.23}$$

The proportionality constant is denoted as the diffusion coefficient or diffusivity D_n.

Thus, it induces a diffusion current with density

$$J_n = qD_n \frac{dn}{dx} \tag{2.24}$$

and

$$J_p = -qD_p \frac{dp}{dx} \tag{2.25}$$

for electrons and holes, respectively. The diffusion is driven by the random thermal motion of carriers and scattering. The diffusion length L_d is used to characterize the maximum distance carriers can diffuse within the carrier lifetime τ, which follows

$$L_d = \sqrt{D\tau} \tag{2.26}$$

To derive the relationship between the diffusion coefficient and mobility, thermal equilibrium is considered, where the diffusion current is compensated by the drift current induced by the build-in electrical field. This build-in electric field is formed by the nonuniform doping[37]. Thus, without an external electrical field, the net current is zero. Such behavior can be described by

$$qn\mu_n E_{bi} = -qD_n \frac{dn}{dx} \tag{2.27}$$

For n-type semiconductors, this is given by

$$\frac{dn}{dx} = \frac{-qE_{bi}}{kT} N_C \exp\left(-\frac{E_C - E_F}{kT}\right) = \frac{-qE_{bi}}{kT} n \tag{2.28}$$

Further, it can be simplified

$$D_n = \left(\frac{kT}{q}\right)\mu_n \tag{2.29}$$

Quite analogous for a p-type semiconductor

$$D_p = \left(\frac{kT}{q}\right)\mu_p \tag{2.30}$$

This is referred to as the Einstein relation, which holds for nondegenerate semiconductors in the equilibrium state. Notably, via the Einstein relation, the diffusion coefficient can be calculated just by measuring the mobility.

In addition, generation and recombination are crucial steps to describe the non-equilibrium state (i.e. $n \cdot p \neq n_i^2$) of a semiconductor. Carrier generation results from processes in which the

Die approbierte gedruckte Originalversion dieser Dissertation ist an der TU Wien Bibliothek verfügbar.
The approved original version of this doctoral thesis is available in print at TU Wien Bibliothek.
TU Bibliothek WIEN Your knowledge hub

semiconductor absorbs energy resulting in free electrons and holes. Recombination describes the inverse processes i.e. electron-hole recombination under energy release. At equilibrium ($n_0 \cdot p_0 = n_i^2$), recombination and generation occur at equal rates, and the net charge carrier density remains constant. A non-equilibrium state with an excess of carriers (i.e., $np > n_i^2$) causes a higher recombination rate, making the system return to equilibrium. Conversely, if $np < n_i^2$, the generation rate would be higher, driving the system toward equilibrium.

2.2.3 The p-n diode

The p-n junction is one of the most important devices for modern electronic applications as well as for understanding the underlying mechanism of more sophisticated semiconductor devices. The associated theory developed by Shockley[40] is regarded as a fundamental cornerstone of semiconductors. A typical p-n junction generally forms at the interface of adjacent p- and n-type doped semiconductors (see **Figure 2.9**).

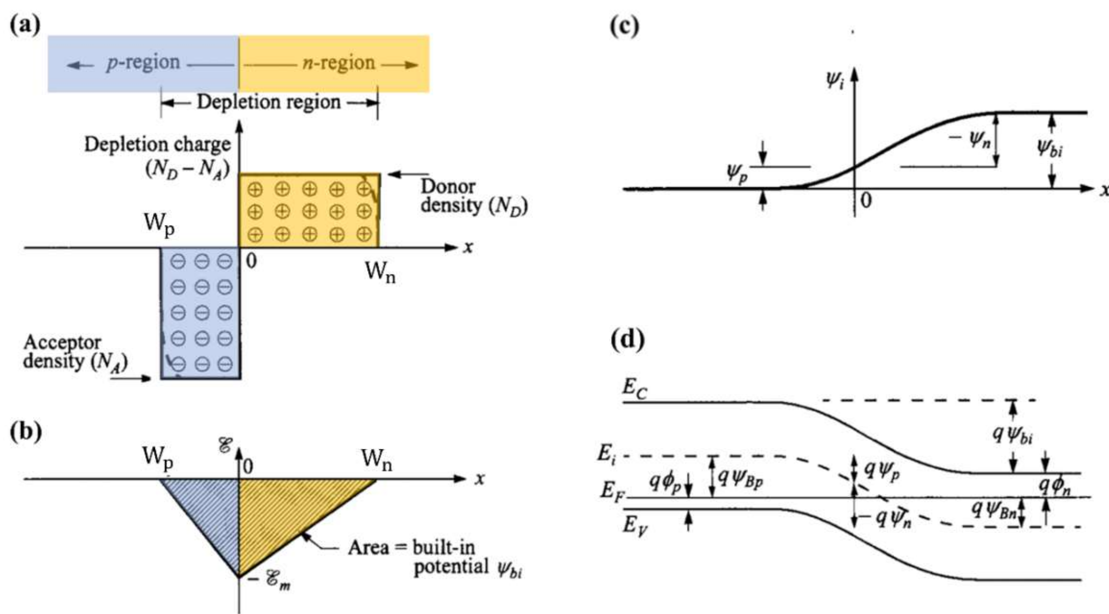

Figure 2.9 (a) Space-charge distribution in p-type and n-type semiconductors with the doping concentration of N_A and N_D, respectively. W_p and W_n represent the width of the depletion regions in the p-type and n-type semiconductors, respectively. (b) Electric-field distribution featuring a maximum at the interface (x = 0). Besides, the area under the curve indicates the build-in potential Ψ_{bi}. (c) Potential distribution. The build-in potential Ψ_{bi} can be considered as the sum of two individual potentials (i.e. $\Psi_{bi} = \Psi_p + \Psi_n$). (d) Energy-band diagram of the abrupt p-n junction in thermal equilibrium. Images adapted from Sze S. M. et al.[5].

Die approbierte gedruckte Originalversion dieser Dissertation ist an der TU Wien Bibliothek verfügbar.
The approved original version of this doctoral thesis is available in print at TU Wien Bibliothek.
TU WIEN Bibliothek Your knowledge hub

In n-type semiconductors, electrons and holes are denoted as majority and minority carriers, respectively (and vice versa for p-type semiconductors). Once p- and n-type semiconductors are in contact with each other, excess electrons from the n-region diffuse into the p-region and vice versa for holes from the p-region, in order to balance the doping gradient. Once reaching the thermal equilibrium, a space-charge region forms in the vicinity of the interface. **Figure 2.9a** illustrates the charge distribution and the induced space charge region with the respective depletion widths W_p and W_n. The charge densities are referred to as the donor and acceptor densities N_D and N_A in the n- and p-type material, respectively. The diffusion current is self-limiting as the drift current induced by the build-in electric field compensates the diffusion current (**Figure 2.9b**). With respect to the build-in electric field, the maximum electric field intensity is given at the interface (i.e. x = 0). By integrating the electric field intensity over the depletion region, the build-in potential Ψ_{bi} can be calculated (**Figure 2.9c**), which can also be derived from the charge distribution using the Poisson equation

$$\Psi_{bi} = \frac{k_B T}{q} \ln\left(\frac{N_D N_A}{n_i^2}\right) \tag{2.31}$$

with n_i the intrinsic carrier concentration.

Under thermal equilibrium and zero applied bias, the diffusion current compensates dynamically the drift current, thus no net current flows and the Fermi level would remain constant through the entire p-n junction. As the direction of the build-in electric field is toward the p-region, the position of the corresponding conduction band of the n-type semiconductor shifts downwards (**Figure 2.9d**). Due to the charge neutrality in the depletion region ($W_p \cdot N_A = W_n \cdot N_D$), the depletion width in the p- and n-region can be calculated according to

$$W_p = \sqrt{\frac{2\varepsilon_s \Psi_{bi}}{q} \frac{N_D}{N_A(N_A+N_D)}} \tag{2.32}$$

$$W_n = \sqrt{\frac{2\varepsilon_s \Psi_{bi}}{q} \frac{N_A}{N_D(N_A+N_D)}} \tag{2.33}$$

with ε_s the permittivity of the semiconductor.

The p-n junction diode generally generates a small current at negative bias and a large current at positive bias, referred to as the rectifying characteristic. **Figure 2.10** demonstrates a typical current-voltage curve of an ideal p-n junction diode. In this configuration, an external bias is applied to the p-type semiconductor, while the electrode connected to the n-type semiconductor is grounded.

TU Bibliothek WIEN Your knowledge hub
Die approbierte gedruckte Originalversion dieser Dissertation ist an der TU Wien Bibliothek verfügbar.
The approved original version of this doctoral thesis is available in print at TU Wien Bibliothek.

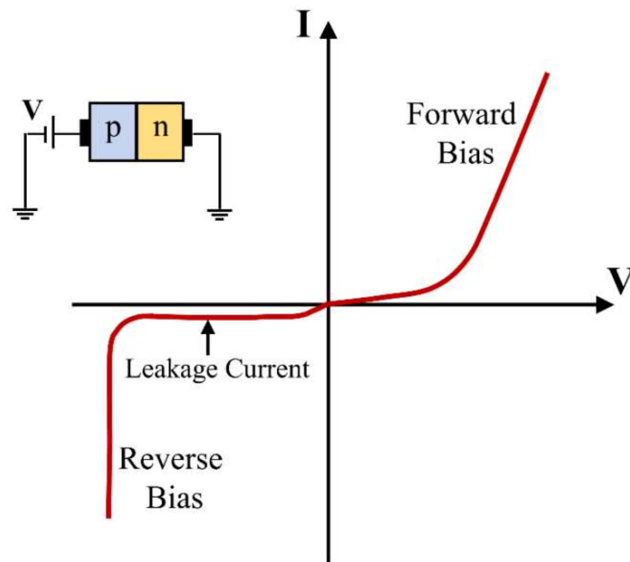

Figure 2.10 The I/V characteristic of an ideal p-n junction diode. The inset illustrates the measurement setup.

At forward bias (i.e. V > 0 V), the depletion width of the p-n junction is reduced, thereby electrons can cross the junction and be injected into the p-type semiconductor. For an ideal diode, the current density increases exponentially, according to the Shockley equation[40]

$$J = J_0 \left[e^{\frac{qV}{k_B T}} - 1 \right] \tag{2.34}$$

with J_0 the reverse-bias saturation current density.

In contrast, at the reverse bias (i.e. V < 0 V), the width of the depletion region increases, thereby limiting the flow of the current. The remaining small current is called leakage current. However, if the reverse bias is too high, the current is permitted to flow again, due to the breakthrough of the diode.

2.2.4 Schottky junction

Aside from the p-n junction formed by two adjacent semiconductors, another essential component of semiconductor technology results from the metal-semiconductor contact. Once a metal and one semiconductor are brought into contact, the Fermi levels will be aligned to match thermal equilibrium, which is realized by electrons transferring between the metal and the semiconductor. **Figure 2.11a** and **b** illustrate the energy bands of the metal and semiconductor before and after the formation of a Schottky contact, respectively.

Die approbierte gedruckte Originalversion dieser Dissertation ist an der TU Wien Bibliothek verfügbar.
The approved original version of this doctoral thesis is available in print at TU Wien Bibliothek.
TU Bibliothek WIEN Your knowledge hub

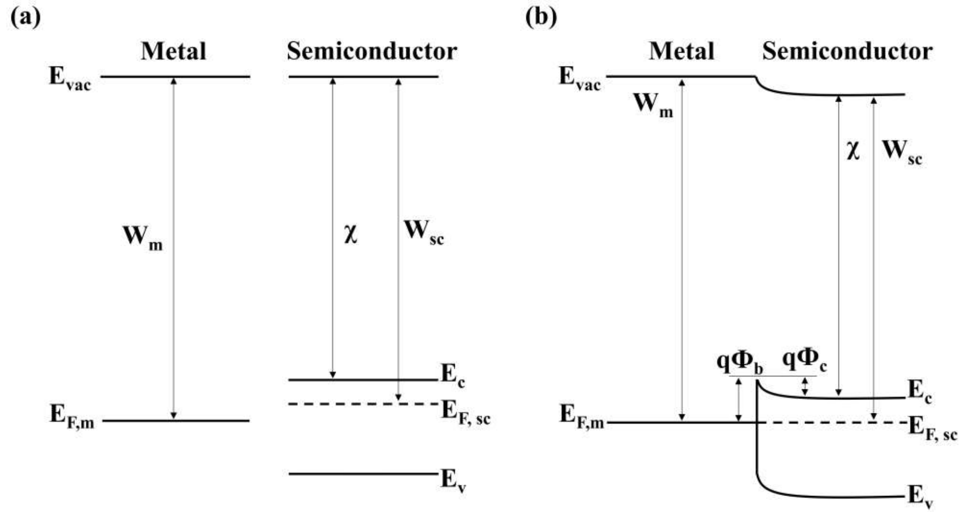

Figure 2.11 (a) Band diagrams of separated metal and n-type semiconductor, in which the work function W_m of the metal is larger than that of the n-type semiconductor. (b) Formation of the Schottky junction. Electrons will keep transferring between the n-type semiconductor and the metal, enabling the alignment of two Fermi levels $E_{F,m}$ and $E_{F,sc}$, consequently resulting in a Schottky barrier Φ_b and the build-in contact potential Φ_c. Figure adapted from Sze S. M. et al.[37].

In metals the electron density is almost equal to the density of atoms and electrons can move without restrictions forming a free electron gas. Further, the work function is applied to describe the minimum thermodynamic energy, which electrons require to escape into the vacuum. As depicted in **Figure 2.11a**, the work function is given by

$$W_m = E_{vac} - E_{F,m} \tag{2.35}$$

with E_{vac} the vacuum energy level and $E_{F,m}$ the metal's Fermi level.

For a semiconductor, the electron affinity χ denotes the energy needed to remove an electron from the conduction band edge into the vacuum level (i.e. $\chi = E_{vac} - E_c$). In analogy to the work function of the metal W_m, the work function of semiconductors W_{sc} can be expressed as

$$W_{sc} = E_{vac} - E_{F,sc} = \chi - k_B T ln\left(\frac{N_d}{N_c}\right) \tag{2.36}$$

which furthermore depends on the doping type and concentration. The corresponding build-in contact potential Φ_c is defined as the difference between the two Fermi levels, which is

$$q\Phi_c = E_{F,sc} - E_{F,m} = W_m - W_{sc} \tag{2.37}$$

Therefore, dependent on the build-in contact potential Φ_c, metal-semiconductor contacts can perform rectifying or ohmic behavior. Aside from the metal's work function, it also depends on the semiconductor's electron affinity and impurity doping[41]. **Figure 2.11b** shows a typical

Die approbierte gedruckte Originalversion dieser Dissertation ist an der TU Wien Bibliothek verfügbar.
The approved original version of this doctoral thesis is available in print at TU Wien Bibliothek.
TU WIEN Bibliothek Your knowledge hub

band diagram of the Schottky junction under thermal equilibrium, for a metal and an n-type semiconductor. After electrons flow from the n-type semiconductor into the metal, the interface region near the semiconductor is positively charged, consequently creating a depletion region, in analogy to a p-n junction. Due to the ultra-high electron density in the metal, the related negatively-charged space charge region in the metal side is negligible. Therefore, it establishes a depletion region into the semiconductor, and the corresponding width can be approximated as

$$W = \sqrt{2\varepsilon_s\varepsilon_0 \frac{\phi_c - V}{qN_D}} \tag{2.38}$$

with ε_s the relative permittivity of the semiconductor, ε_0 the vacuum permittivity, V the externally applied bias and N_D the doping concentration. Furthermore, the Schottky barrier height Φ_b can be calculated, according to

$$\Phi_b = W_m - \chi \tag{2.39}$$

Please note that all equations mentioned above are derived under the condition that the metal/semiconductor interface is clean without significant interface states. In contrast, when surface states are taken into account, the Fermi level of the semiconductor becomes pinned, making barrier height widely insensitive to the metal's work function[42]. This effect is denoted as Fermi level pinning, as depicted in **Figure 2.12**.

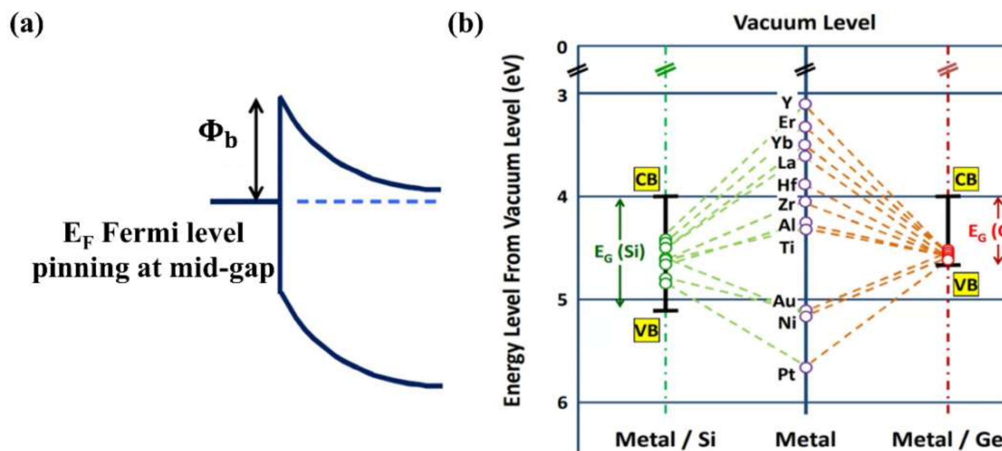

Figure 2.12 (a) Fermi level pinning at mid-gap. (b) Material screening demonstrates that most metals result in strong Fermi level pinning at mid-gap for Si and near the valence band for Ge. Adopted from Ang K. W. et al[43].

Die approbierte gedruckte Originalversion dieser Dissertation ist an der TU Wien Bibliothek verfügbar.
The approved original version of this doctoral thesis is available in print at TU Wien Bibliothek.
TU Bibliothek WIEN Your knowledge hub

Figure 2.12a shows a typical schematic diagram of Fermi level pinning for an n-type semiconductor. Generally, only surface states lying above the Fermi level are empty, and the others below the Fermi level are filled. When the Schottky contact is formed, electrons move from the semiconductor toward the metal, causing band bending near the contact. Further, an upward band bending lifts more surface states above the Fermi level E_F, meaning there is electron emission at the surface, which continues until the system reaches thermal equilibrium. However, for large surface state density, a small change in E_F will release a large number of electrons. Thus, the Fermi level tends to be located at the energy at which there is a large density of surface states, independent of the metal's work function. Here, two commercially implemented semiconductors Si and Ge are taken as examples to demonstrate the Fermi level pinning effect (**Figure 2.12b**). Regarding Ge, nearly all metals form a significant Schottky barrier to *n*-type Ge and an ohmic contact to *p*-type Ge, since the metal's Fermi level is strongly pinned to the valence band. In contrast, for Si the Fermi level tends to be pinned at the mid-gap, thus forming a significantly high barrier for electrons and holes.
Schottky diodes have similar current-voltage characteristics as p-n junctions but the reverse saturation current depends exponentially onto the barrier height Φ_b (**Figure 2.13a**).

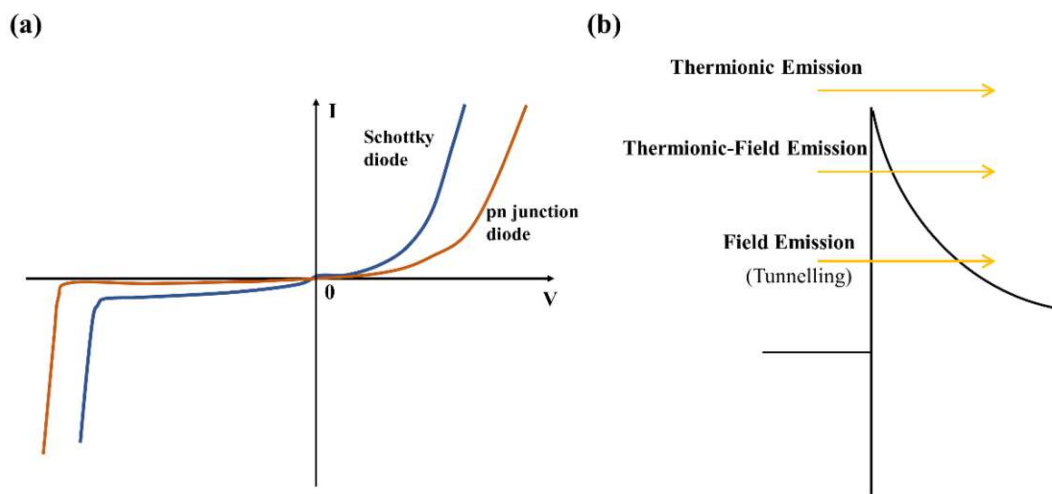

Figure 2.13 (a) Comparison of the typical I/V curve of a Schottky diode and a p-n junction diode. (b) Band diagram describing thermionic emission, thermionic-filed emission and Field emission.

At a positive bias, the Schottky junction is forward-biased with a decreased charge space region, allowing a large current to flow. By contrast, under a negative voltage, external applied

Die approbierte gedruckte Originalversion dieser Dissertation ist an der TU Wien Bibliothek verfügbar.
The approved original version of this doctoral thesis is available in print at TU Wien Bibliothek.
TU WIEN Bibliothek Your knowledge hub

electrical field would extend the width of charge space region, thus blocking the flow of the current. Therefore, Schottky diodes can also exhibit rectification characteristics like p-n junctions. In contrast to the minority carrier dominated transport in p-n junctions, the currentin metal-semiconductor junctions is carried by the majority carriers. The main mechanisms contributing to the total current, involving thermionic emission, thermionic-field emission and field emission, are discussed in **Figure 2.13b**. Thermionic emission describes the process in which electrons with sufficient energy pass the Schottky barrier. Field emission defines a tunnelling process of electrons through the Schottky barrier. Generally, a low electric field and a high temperature can prompt the occurrence of thermionic emission. In contrast, a high electric field and a low temperature are preferential conditions for field emission. The intermediate mechanism between thermionic emission and field emission is so-called thermionic-filed emission, which can be considered as a combination of thermionic emission and field emission. The thermionic-field emission describes the following transport process: the electron energy can be enhanced by thermionic emission to the higher portion of the barrier, which has a lower thickness, and the chance of tunnelling is higher, and then it passes through the barrier by tunnelling emission[45].

Die approbierte gedruckte Originalversion dieser Dissertation ist an der TU Wien Bibliothek verfügbar.
The approved original version of this doctoral thesis is available in print at TU Wien Bibliothek.
TU WIEN Bibliothek Your knowledge hub

2.3 Light-matter interaction

2.3.1 Light-semiconductor interaction

When light interacts with a semiconductor, it can either be absorbed (generating a pair of free carriers) or it can stimulate a recombination event. Absorption is the active process in e.g. solar cells and semiconductor photodetectors, while stimulated emission is the process enabling lasering.

As light passes through the semiconductor, a fraction of light is absorbed by the semiconductor on the way through. The attenuation follows an exponential decay

$$I(x) = I(x_0)e^{-\alpha(x-x_0)} \tag{2.40}$$

where $I(x_0)$ *and* $I(x)$ are the intensity at a surface point x_0 and a certain depth x inside the semiconductor respectively, and α is the absorption coefficient. The absorption coefficient characterizes the rate of losing radiant flux due to the semiconductor absorption alone, which is an intrinsic property of the semiconductor and depends on the light wavelength. The penetration depth $\boldsymbol{\delta_p}$ is another relative parameter, which is commonly used to define the depth at which the intensity of light $I(x_0)$ inside the semiconductor falls to 1/e (about 37%) of its initial value at the surface $I(x_0)$. Then according to Beer-Lambert law, the formula related to the absorption coefficient can be expressed as

$$\delta_p = \frac{1}{\alpha} \tag{2.41}$$

For example, for Si the penetration depth $\boldsymbol{\delta_p}$ at a wavelength of 1000 nm is 140 µm due to the absorption coefficient of α = 72 cm^{-1}. Therefore, it well explains why Si-based solar cells require a crystal thickness of approximately 200 µm to realize a high level of absorption.

Semiconductor absorption is also known as ‘basic lattice absorption’, that is, one electron is excited into the conduction band, leaving a hole in the valence band. Certain peculiarities of this process need comprehensive consideration, as the conservation laws of energy and momentum cause certain selection rules. Since a photon possesses a comparatively large amount of energy but a negligibly small momentum, the crystal momentum remains almost unchanged despite the crystal energy rising during the absorption process. Semiconductors can be classified into two typical types, according to the bandgap of the semiconductor i.e. direct bandgap and indirect bandgap. **Figure 2.14a** depicts the absorption process of a direct semiconductor wherein an electron with sufficient energy can be excited from the valence band

TU Bibliothek Your knowledge hub WIEN
Die approbierte gedruckte Originalversion dieser Dissertation ist an der TU Wien Bibliothek verfügbar.
The approved original version of this doctoral thesis is available in print at TU Wien Bibliothek.

maximum to the conduction band minimum without any momentum mismatch. This process can occur even when an electron does not initially locate at the valence band maximum.

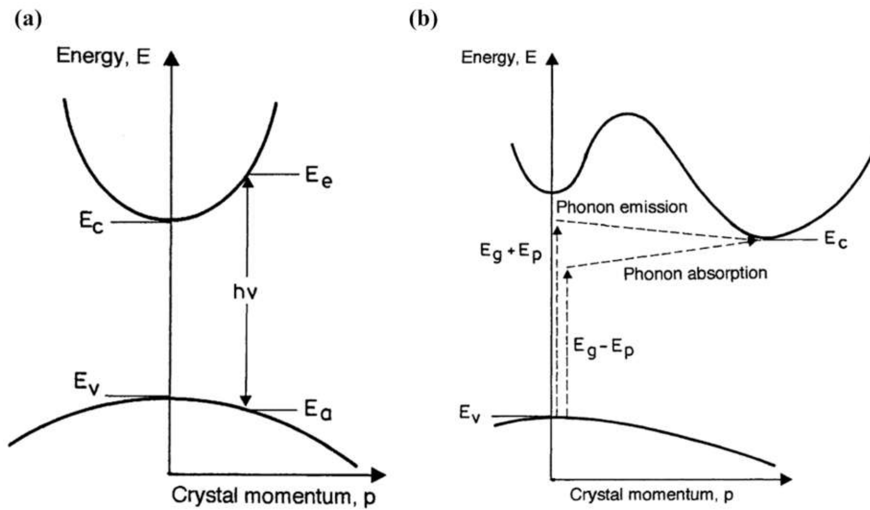

Figure 2.14 Light absorption mechanism for (a) direct-bandgap semiconductor and (b) indirect-bandgap semiconductor. Images adapted from Goetzberger A. et al.[46].

In this view, light absorption in a direct-bandgap semiconductor should be dependent on the energy of the incident light, which can be expressed as[47]

$$\alpha = C\left(h\frac{c}{\lambda} - E_g\right)^{\frac{1}{2}} = C\left(h\upsilon - E_g\right)^{\frac{1}{2}} \tag{2.42}$$

The value for the constant C approximates 2×10^4 for a direct-bandgap semiconductor. For instance, for a common direct-bandgap semiconductor like GaAs with the bandgap of $E_g = 1.52$ eV the absorption coefficient is found to be $\alpha = 6.3 \times 10^3$ cm^{-1} giving a penetration length of $\delta_p = 1.6$ µm, in agreement with other reports that GaAs only requires very thin layers of a few micrometers for solar cells[48,49].

Figure 2.14b demonstrates the absorption behavior of an indirect-bandgap semiconductor where the conduction band minimum and the valence band maximum correspond to different crystal momentum. The mandatory requirement is that the photon energy exceeds the bandgap (i.e. $hv \geq E_g$). Although the crystal momentum mismatches for indirect-bandgap semiconductors, the excited electron has some possibility to reach the conduction band with the assistance of an additional momentum from thermal vibrations (i.e. a phonon). Compared to a photon, a phonon itself owns a large momentum, despite its energy being rather low. As this process involves two different types of particles, the absorption probability of indirect-bandgap semiconductors is much lower than that of direct-bandgap semiconductors.

Die approbierte gedruckte Originalversion dieser Dissertation ist an der TU Wien Bibliothek verfügbar.
The approved original version of this doctoral thesis is available in print at TU Wien Bibliothek.
TU WIEN Bibliothek Your knowledge hub

Another crucial light-semiconductor interaction is so-called recombination. **Figure 2.15a** depicts the band-to-band recombination process for direct bandgap semiconductors.

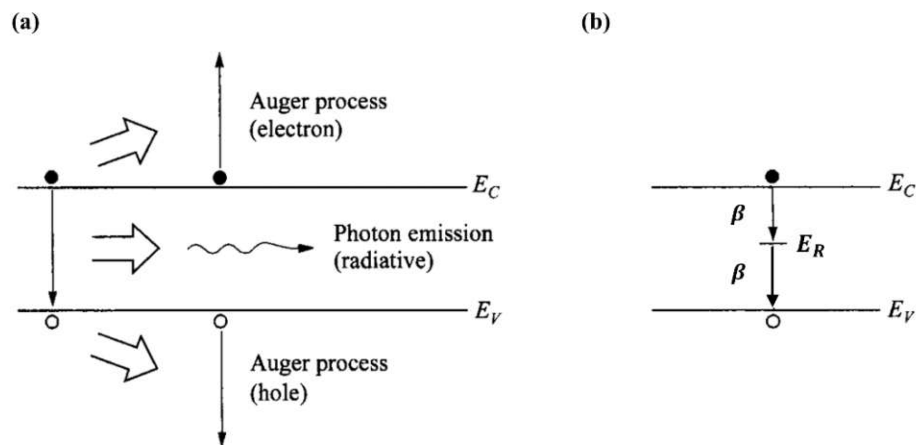

Figure 2.15 (a) Radiative recombination, resulting in the emission of photons or electrons via Auger recombination. (b) Non-radiative recombination through single-level traps. β is the capture cross-section of the imperfection. E_R is the trap energy level. Figure adapted from Satpathy R. et al.[50].

Electrons release from the conduction band to the valence band, and subsequently recombine with holes in the valence band. The energy can be released either via photon emission (radiative process) or passing the energy onto other free charge carriers (commonly referred to as an Auger process). The radiative process can be essentially considered as the inverted light absorption in the direct bandgap semiconductors, while the Auger recombination can be seen as the opposite of impact ionization[51].

Figure 2.15b demonstrates the non-radiative recombination in a semiconductor, assisted by a single-level trap with the energy of E_R inside the bandgap. In principle, such a recombination process can be divided into two steps. Firstly, an electron is captured by an empty trap. Afterward, a hole recombines with the trapped electron before the electron re-emits to the conduction band, making the occurrence of electron-hole recombination. The electron and hole capture cross-sections describe the capacity of traps to capture electrons and holes, respectively.

TU WIEN Bibliothek Your knowledge hub
Die approbierte gedruckte Originalversion dieser Dissertation ist an der TU Wien Bibliothek verfügbar.
The approved original version of this doctoral thesis is available in print at TU Wien Bibliothek.

2.3.2 Surface plasmons

2.3.2.1 Plasma theory

In principle, all matter in the explored universe can be divided into four types of states: solid, liquid, gaseous, and plasma. The vocabulary plasma originates from Greek and denotes something molded. The first official application of the word plasma dates back to 1929 by Tonks and Langmuir, which was applied to describe the inner region of a glowing ionized gas produced by electric discharge in a tube, the ionized gas as a whole remaining electrically neutral[52]. When the thermal kinetic energy exceeds the molecular binding energy, the binding between atoms will be broken and a molecular gas gradually dissociates into an atomic gas. At sufficiently elevated temperatures an increasing fraction of the atoms will further possess enough kinetic energy to overcome, by collisions, the binding energy of the outermost orbital electrons, resulting in an ionized gas or plasma. Therefore, plasma is applied to define numerous macroscopically neutral substances comprising lots of interacting ionized atoms or molecules and free electrons, enabling collective behavior based on long-range coulomb forces. In a metal, free electrons can be regarded as an electron plasma with the hypothesis of the positive ions fixed in their locations. Furthermore, a plasmon is a quasi-particle resulting from the quantization of plasma oscillations of the free electron gas. The relationship between plasmon and plasma is in analogy to photon to light. The plasma frequency ω_p is defined as[53]

$$\omega_p = \sqrt{\frac{n \cdot q^2}{\mathrm{m}_e^* \cdot \varepsilon_0}} \tag{2.43}$$

Such plasma theory can be applied to explain the optical properties of metals. Reflection occurs at the frequency of the incident light below the plasma frequency, as the electrons inside the metal shield the electric field of the incident light. In contrast, incident light with frequency higher than the plasma frequency is transmitted, since the electrons cannot respond such fast to screen it. The plasma frequency of most metals lies in the ultra-violet region, thus reflecting visible light. For some metals with particular electronic band structure inter-band absorption in the visible range make them appear correspondingly colored.

2.3.2.2 Surface plasmon polariton

In 1957 Ritchie proposed the concept of surface plasmons in the context of electron energy loss in thin metal films[54] and the experimental verification followed two years later by Powell and Swan [55,56]. Ten years later the explanation and repeated optical excitation of surface plasmons were reported almost simultaneously by Otto[57] as well as Kretschmann

Die approbierte gedruckte Originalversion dieser Dissertation ist an der TU Wien Bibliothek verfügbar.
The approved original version of this doctoral thesis is available in print at TU Wien Bibliothek.
TU Bibliothek WIEN Your knowledge hub

and Raether[58]. Surface plasmon polaritons (SPPs), electromagnetic surface waves propagating along an insulator/conductor interface, are excited when an incoming electromagnetic field is coupled to the oscillations of the electron plasma in the conductor. This only happens when the wavevector of the incoming light matches that of the SPP for the same angular frequency. A classical model with respect to the SPP generation at the metal/dielectric interface (i.e. z = 0) is introduced (**Figure 2.16a**).

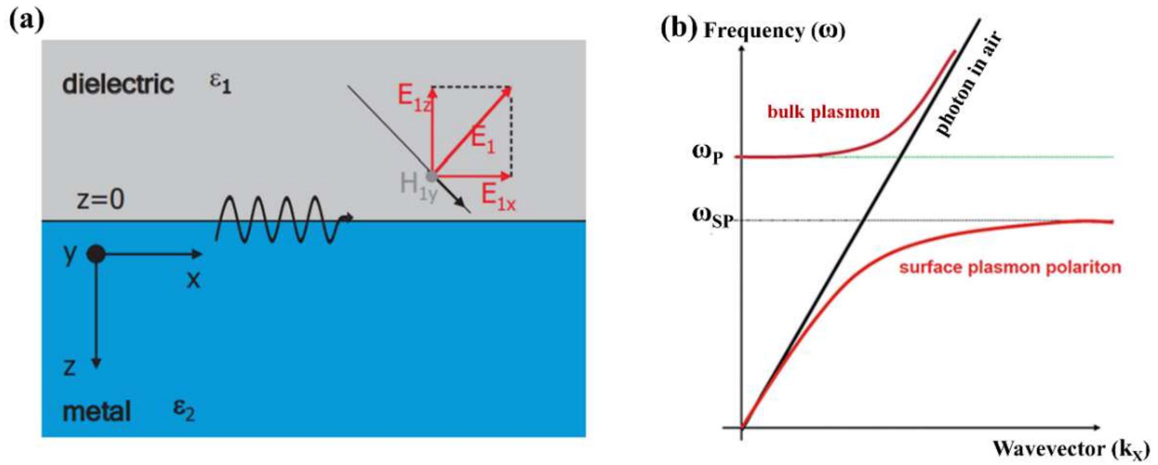

Figure 2.16 (a) Schematic diagram demonstrating the excitation and propagation of SPPs at a metal/dielectric interface. (b) The dispersion relation of bulk plasmon and surface plasmon. Images adapted from Luo M. R.[59].

Maxwell's equations can be applied to describe this case

$$\nabla \times H_i = E_i \frac{1}{c}\frac{\partial}{\partial t} E_i \quad (2.44)$$

$$\nabla \times E_i = -\frac{1}{c}\frac{\partial}{\partial t} H_i \quad (2.45)$$

$$\nabla \cdot (\varepsilon_i E_i) = 0 \quad (2.46)$$

$$\nabla \cdot H_i = 0 \quad (2.47)$$

where the subscript i represents the material: i = 1 at z < 0 for the metal, and i = 2 at z > 0 for the dielectric. To solve Maxwell's equations s- and p-polarized electromagnetic modes are considered, including p-polarized one and s-polarized one, corresponding to the component of the electric field oriented parallel and perpendicular to the interface, respectively. In order to realize a travelling wave propagating along the interface, the electric field component needs to be parallel to the interface, therefore the s-polarized surface oscillation can be excluded. Afterward, the p-polarized one can be expressed as

TU WIEN Bibliothek Your knowledge hub
Die approbierte gedruckte Originalversion dieser Dissertation ist an der TU Wien Bibliothek verfügbar.
The approved original version of this doctoral thesis is available in print at TU Wien Bibliothek.

$$E_i = \left(E_{i_x}, 0, E_{i_z}\right) e^{-k_i|z|} e^{i(q_i x - \omega t)} \tag{2.48}$$

$$H_i = \left(0, E_{i_y}, 0\right) e^{-k_i|z|} e^{i(q_i x - \omega t)} \tag{2.49}$$

with q_i the component of a wavevector along the interface. Introducing **Eq. 2.48** and **Eq. 2.49** into the Maxwell's equations (**Eq. 2.44-2.47**), leads to

$$i\, k_1 H_{1_y} = +\frac{\omega}{c} \varepsilon_1 E_{1_x} \tag{2.50}$$

$$i\, k_2 H_{2_y} = +\frac{\omega}{c} \varepsilon_2 E_{2_x} \tag{2.51}$$

and

$$k_i = \sqrt{q_i^2 - \varepsilon_1 \frac{\omega^2}{c^2}} \tag{2.52}$$

As the boundary conditions should be continuous, **Eq. 2.50** and **Eq. 2.51** result in

$$\frac{k_1}{\varepsilon_1} H_{1_y} + \frac{k_2}{\varepsilon_2} H_{2_y} = 0 \tag{2.53}$$

$$H_{1_y} - H_{2_y} = 0 \tag{2.54}$$

Further, assuming the determinant is zero, the surface-plasmon condition can be derived as

$$\frac{k_1}{\varepsilon_1} + \frac{k_2}{\varepsilon_2} = 0 \tag{2.55}$$

If **Eq. 2.55** is introduced into **Eq. 2.52**, the surface-plasmon condition can also be derived as

$$q(\omega) = \frac{\omega}{c} \sqrt{\frac{\varepsilon_1 \varepsilon_2}{\varepsilon_1 + \varepsilon_2}} \tag{2.56}$$

with ω/c representing the magnitude of the light wavevector.

Figure 2.16b depicts the dispersion relations of bulk plasmons, photons in air and surface SPPs. The linear curve in the middle represents the dispersion relation of light in air, normally denoted as a light line. The upper-left non-linear curve describes the dispersion of the free electron gas inside the metal, also referred to as bulk plasmon. As can be seen, for $\omega < \omega_p$ the propagation of transverse electromagnetic waves is forbidden inside the metal plasma. For $\omega > \omega_p$ however, the plasma supports transverse waves propagating with a group velocity $v_g = d\omega/dk < c$. Furthermore, the lower-right non-linear curve demonstrates the dispersion relation of a surface plasmon, which is lower than the light line, due to the bound nature[60].

2.3.2.3 Plasmon coupling

As depicted in **Figure 2.16b,** the distinct gap between the light line ($\omega = c\cdot q$) and the surface plasmon polariton line (the lower red line) indicates a momentum mismatch between free space light and an SPP. Therefore, light cannot directly excite surface plasmons on a flat metal

TU Bibliothek WIEN Your knowledge hub
Die approbierte gedruckte Originalversion dieser Dissertation ist an der TU Wien Bibliothek verfügbar.
The approved original version of this doctoral thesis is available in print at TU Wien Bibliothek.

surface. For the same reason, SPPs cannot be out-coupled directly into the free space either. **Figure 2.17** shows some special techniques for exciting SPPs.

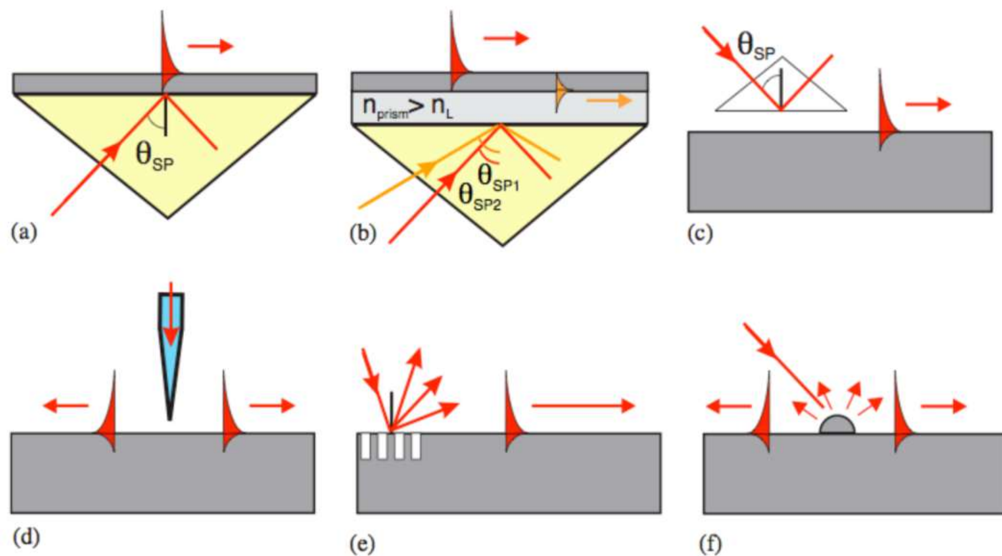

Figure 2.17 Various methods for exciting SPPs, including (a) Kretschmann geometry, (b) two-layer Kretschmann geometry, (c) Otto geometry, (d) excitation by a nearfield scanning optical microscopy probe, (e) diffraction on a grating, and (f) diffraction on a surface defect. (from Maier S. A.[60]).

Figure 2.17a depicts the schematic diagram of the so-called Kretschmann-Raether configuration, where a metal layer is directly deposited on a glass block, typically a prism. The light impinging the prism excites SPPs at the outer side of the metal layer, as the evanescent wave can penetrate through the metal film. **Figure 2.17b** illustrates a typical configuration where an additional dielectric film with a higher dielectric constant is added between the metal layer and the prism. Attenuated total reflection occurs at the interface between the prism and the dielectric layer, resulting in an evanescent field exciting the SPPs at both interfaces of the metal film. **Figure 2.17c** shows the Otto configuration, wherein attenuated total reflection inducts inside a prism. In order to excite SPPs on the surface, a thin metal film (e.g. gold) needs to be close enough to the prism, leading to the interaction between the evanescent wave and the plasma waves on the surface.

A near-field probe tip, as a point source providing a series of wave vectors, is also a common tool to excite SPPs (see **Figure 2.17d**).

Structuring the metal is another approach to overcome the momentum mismatch. **Figure 2.17e** shows a grating in the structure of shallow grooves, which can support additional wavevectors

Die approbierte gedruckte Originalversion dieser Dissertation ist an der TU Wien Bibliothek verfügbar.
The approved original version of this doctoral thesis is available in print at TU Wien Bibliothek.
TU Bibliothek Your knowledge hub WIEN

via scattering, thereby meeting the momentum conservation. For the same reason, surface roughness can excite SPPs as well (**Figure 2.17f)**.

2.3.2.4 Plasmon waveguiding

SPPs can be simply classified into two types (i.e. localized and propagating plasmons), depending on the size and shape of the metallic structures. Localized optical modes are generated when SPPs are confined to nanoparticles. Propagating surface plasmons are evanescent electromagnetic waves bounded to smooth metal-dielectric interfaces, which can serve as plasmonic waveguides, even if the minimum dimension thereof does not exceed the light wavelength. **Figure 2.18a** shows schematically the intensity distribution and the electromagnetic field components of a propagating SPP supported by a metal-dielectric interface. In order to excite a bound or propagating SPP, the necessary condition is

$$Re\{\varepsilon_m(\omega)\} < -\varepsilon_d \tag{2.57}$$

with ε_m and ε_d the relative permittivity of the metal and the dielectric, respectively. For most metals and dielectrics, this condition is satisfied in the visible (if the wavelength is not too short) and infrared regions.

The real part of the SPP wavevector controls the SPP wavelength

$$\lambda_{SPP} = \frac{2\pi}{Re(k_{SPP})} \tag{2.58}$$

which is always smaller than the light wavelength in the dielectric

$$\lambda_{SPP} < \frac{\lambda}{\sqrt{\varepsilon_d}} \tag{2.59}$$

where λ is the wavelength of light in the vacuum.

Due to inevitable losses, the damping of the SPP propagation is given by the imaginary part of the plasmon wavevector k_{SPP}

$$I_{SPP}(x) = I_0 e^{-2Im(k_{spp})x} \tag{2.60}$$

where I_0 is the initial intensity of the SPP. The propagation length of SPPs denotes the distance at which the intensity drops to 1/e of the initial intensity, then be defined as

$$L_{SPP} = \frac{1}{Im(2k_{SPP})} \tag{2.61}$$

Die approbierte gedruckte Originalversion dieser Dissertation ist an der TU Wien Bibliothek verfügbar.
The approved original version of this doctoral thesis is available in print at TU Wien Bibliothek.
TU WIEN Bibliothek Your knowledge hub

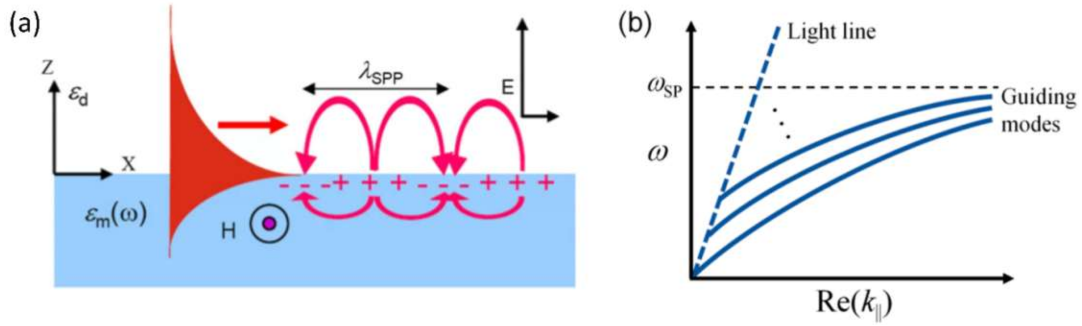

Figure 2.18 (a) The intensity distribution of an SPP along a metal-dielectric interface. (b) The dispersion relations in different guiding modes in a metal waveguide. Images adapted from Wei H. et al.[61].

In analogy to the definition of the refractive index for a material, an effective refractive index of a plasmonic waveguide can also be denoted as

$$n_{eff} = \frac{Re(k_{SPP})}{k_0} = \frac{\lambda_0}{\lambda_{SPP}} \tag{2.62}$$

where k_0 and λ_0 denote the wavevector and wavelength in vacuum, respectively. The effective refractive index n_{eff} is related to the fields distributed inside the metal. That means, the larger confinement of the SPP modes corresponds to a higher n_{eff}. As both the effective refractive index n_{eff} and the wave vector k_{SPP} are frequency dependent, **Figure 2.18b** illustrates the impact of different guiding models on the dispersion relations of SPPs. It indicates the universal trade-off between confinement and loss of SPPs. In particular, larger n_{eff} represents higher confinement and thus higher ohmic losses and a shorter propagation length. For example, the guiding mode inside a metallic nanowire varies with the wavelength of SPPs and the diameter of the nanowire[61], suggesting different confinements of SPPs inside the nanowire, further resulting in altered ohmic loss during the propagation of SPPs. Generally, longer wavelength and larger diameter correspond to smaller ohmic loss and longer propagation length. Aside from Ohmic damping, **Figure 2.19** shows typical losses for SPP propagation.

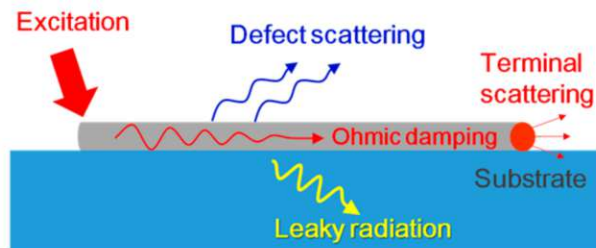

Figure 2.19 The possible mechanisms for losses of SPPs while propagating along a metal waveguide. Images adapted from [61].

Die approbierte gedruckte Originalversion dieser Dissertation ist an der TU Wien Bibliothek verfügbar.
The approved original version of this doctoral thesis is available in print at TU Wien Bibliothek.
TU WIEN Bibliothek Your knowledge hub

The main mechanisms are leaky plasmon modes, ohmic damping and scattering by surface roughness in realistic structures. To avoid leaky radiation, an additional thin dielectric layer of high refractive index can be added increasing the confinement of the plasmon mode. But too high confinement can lead to an inevitable decrease in the propagation length due to enhanced ohmic losses. In addition, the scattering by surface roughness, defects, or the bending of the waveguide also contributes to plasmon losses. For example, the scattering losses can originate from surface roughness and the polycrystalline structure of top-down fabricated nano-waveguides. If a plasmon waveguide is sharply bent, scattering loss always happens at the bending corner as geometrical symmetry is broken and the SPPs couple to light at the corner. Furthermore, the decay of SPP intensity perpendicular to the direction of propagation is another important feature. The penetration depths of the SPP electric field in the dielectric δ_d and metal δ_m are used to describe the behavior, which is given by

$$\delta_{d(m)} = \frac{\lambda_{SPP}}{2\pi} \cdot \sqrt{-\frac{\varepsilon_m + \varepsilon_d}{\varepsilon_{d(m)}^2}} \tag{2.63}$$

so that $\varepsilon_d \delta_d = |\varepsilon_m| \delta_m$. The latter relation implies that the field penetration in the metal is typically much shorter than that in the dielectric. It is interesting that the penetration depth in metals depends rather weakly on the wavelength staying at the level of a few tens of nanometers, while that in dielectrics increases fast and nonlinearly with the wavelength[60].

2.3.2.5 Radiative and non-radiative decay of SPPs

Figure 2.20 illustrates two decay mechanisms of localized surface plasmons (i.e. radiative decay and non-radiative decay).

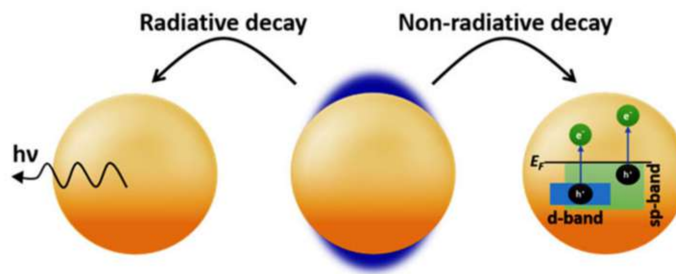

Figure 2.20 Radiative or non-radiative decay mechanisms of localized SPPs. Image adapted from Ahlawat M. et al.[62].

Via radiative decay, plasmons can emit photons[63]. In non-radiative decay, electron-hole pairs are created through Landau damping, as the plasmon-induced electric field can excite electrons

Die approbierte gedruckte Originalversion dieser Dissertation ist an der TU Wien Bibliothek verfügbar.
The approved original version of this doctoral thesis is available in print at TU Wien Bibliothek.
TU Bibliothek WIEN Your knowledge hub

from occupied to unoccupied states. The time-dependent dynamics of the non-radiative decay and the dissipation of hot carriers are illustrated in **Figure 2.21**.

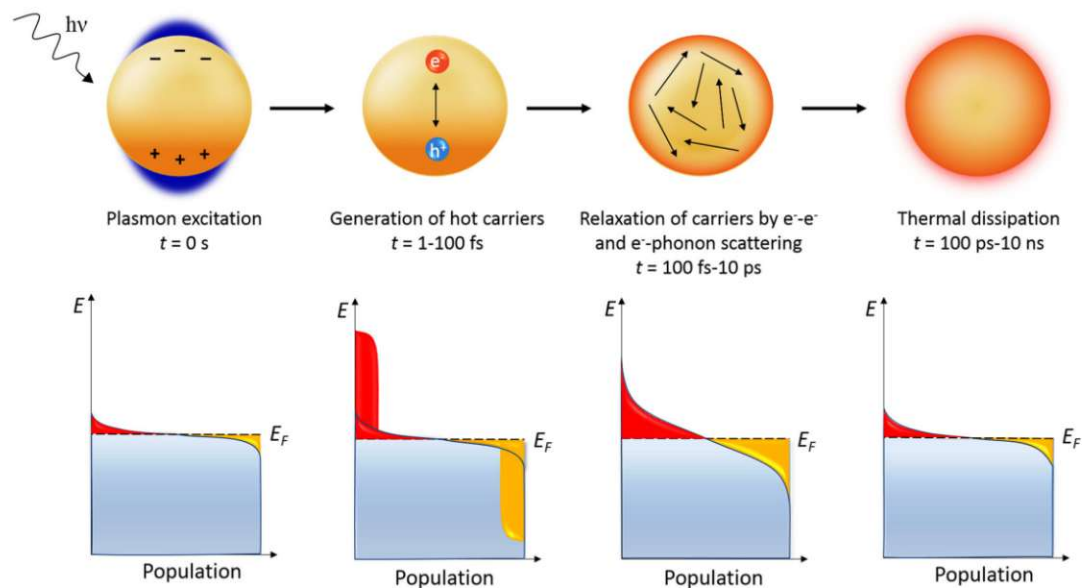

Figure 2.21 Non-radiative decay mechanisms. The upper panels show the dynamics of plasmon decay. The lower panels show the distribution of hot carriers resulting from non-radiative decay of SPPs. Images adapted from [62].

After plasmon excitation and charge carrier generation during plasmon delay within a short time of 1–100 fs, the charge carriers undergo successively electron–electron relaxation, electron–phonon relaxation and finally phonon–phonon relaxation. Primarily, a hot electron–hole pair generated from plasmon decay dissipates its energy via electron–electron scattering on a 100–1000 fs timescale. During the subsequent electron–phonon scattering on a 1–10 ps timescale, the electrons interact with the metal's ionic lattice causing heating of the nanoparticle, as well as phonon–phonon scattering stimulating vibrations in the metal lattice on a 100 ps – 10 ns timescale. This finally results in the heating of the local surrounding environment.

2.3.2.6 Energy distribution of hot carriers from non-radiative plasmon decay

The energy and momentum distribution of hot charge carriers arising from the non-radiative decay of plasmons depends on the size of the nanostructure[64], the symmetry of the plasmon modes[64] as well as the electronic structure and DOS of the material [65]. In other words, a thorough understanding of the aforementioned enables the estimation of hot carrier

Die approbierte gedruckte Originalversion dieser Dissertation ist an der TU Wien Bibliothek verfügbar.
The approved original version of this doctoral thesis is available in print at TU Wien Bibliothek.
TU WIEN Bibliothek Your knowledge hub

distribution, as depicted in **Figure 2.22**. The top panels annotate the permissible transitions for individual metals at selected energies.

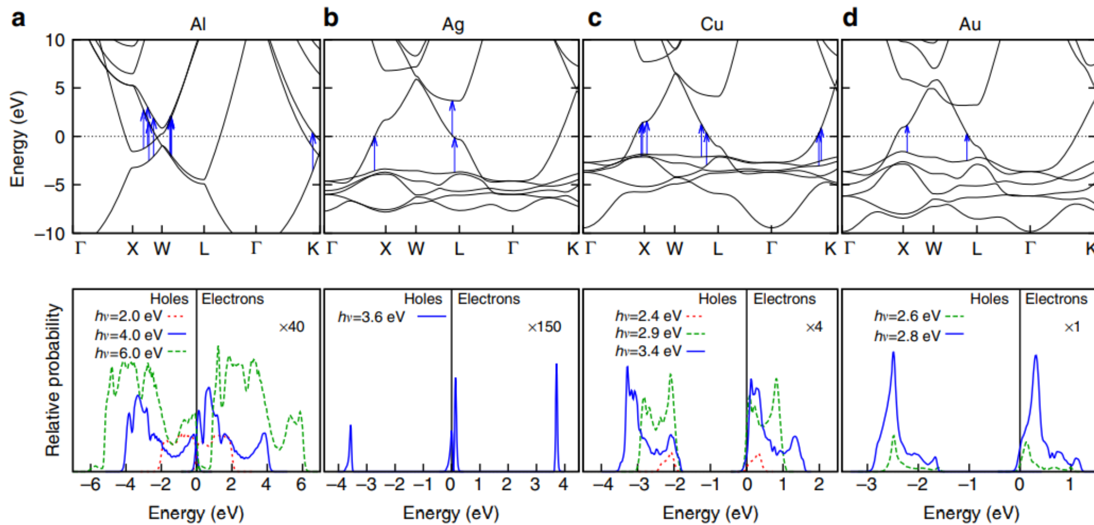

Figure 2.22 The permitted transitions in the band structure (see upper panels) for (a) aluminum, (b) silver, (c) copper and (d) gold. The bottom panels illustrate the energy distribution of hot electrons and hot holes, which are excited via various photon energies hν. Images adapted from Sundararaman R. et al.[65].

For Al, in the vicinity of the W point the band-crossing points lie near the Fermi level, allowing continuous interband transitions in the energetic range from the Fermi level to hν below it. Consequently, both hot electrons and holes from such non-radiative decay are continuously distributed in the energy region from zero energy to the plasmon energy hν, as depicted in the bottom panel of **Figure 2.22a**.

In the case of Ag, low energy interband transitions are observed arising mainly from the d bands at the X and L points, along with the Fermi level at the L point, all of which appear at almost 3.6 eV. Therefore, the simulation depicts bimodal energy distributions for both the electrons and holes, see **Figure 2.22b.**

With respect to Cu and Au, the permissible interband transitions are located close to the X and L points for both metals, along with the K point for Cu, as illustrated in **Figure 2.22c,d**. It is noteworthy that all these transitions originate from the d bands, situated approximately 2 eV below the Fermi level, resulting preferentially in hot holes for Cu and Au.

Die approbierte gedruckte Originalversion dieser Dissertation ist an der TU Wien Bibliothek verfügbar.
The approved original version of this doctoral thesis is available in print at TU Wien Bibliothek.
TU WIEN Bibliothek Your knowledge hub

2.4 Optoelectronic sensors

2.4.1 Basic photodetection mechanisms

Generally, the electrical conductivity of a semiconductor in the dark can be expressed as

$$\sigma_d = q(n_0\mu_0 + p_0\mu_{p0}) \tag{2.64}$$

Under irradiation, due to light absorption of the semiconductor, the conductivity would be altered as

$$\sigma_{ph} = \sigma_d + \sigma_{ph} \tag{2.65}$$

where $\Delta\sigma$ denotes the photoconductivity. For the sake of simplicity, photodetection will be explored for n-type semiconductors, where electrons are the majority carriers.

The conductivity σ_{ph} under irradiation is then given by

$$\sigma_{ph} = \sigma_d + \Delta\sigma = q(n_0 + \Delta n)(\mu_0 + \Delta\mu) \tag{2.66}$$

which takes into account that both the carrier density Δn and the carrier mobility $\Delta\mu$ may change with light irradiation. Then the light-induced change of the conductivity is given by

$$\Delta\sigma = q\mu_0\Delta n + (n_0 + \Delta n)q\Delta\mu \tag{2.67}$$

with Δn the change of the charge carrier density, which follows

$$\Delta n = g\tau_n \tag{2.68}$$

with g the generation rate ($m^{-3} \cdot s^{-1}$) of hot electrons and τ_n the electron lifetime. Therefore, the photoconductivity becomes

$$\Delta\sigma = q\mu_0 g\tau_n + (n_0 + \Delta n)q\Delta\mu = q\mu_0 g\tau_n + n_1 q\Delta\mu \tag{2.69}$$

with n_0 and n_1 the total electron density in the dark and under irradiation, respectively.

Further also the electron lifetime may depend on the generation rate $\tau_n(g)$. In this respect, at least three possible cases can be distinguished

(i) Lifetime τ_n is independent on increased carrier density. The photoconductivity is

$$\Delta\sigma = q\mu_0 g\tau_n \tag{2.70}$$

Thereby, the photoconductivity $\Delta\sigma$ is linearly dependent on the generation rate g. If plotting $\Delta\sigma$ as a function of g in a log-log graph, a slope of the curve is 1.

(ii) Lifetime τ_n depends on increased carrier density, i.e. $\tau_n(g)$. The photoconductivity can be expressed as

$$\Delta\sigma = q\mu_0 g\tau_n(g) \tag{2.71}$$

Assuming the electron lifetime varies exponentially as the generation rate (i.e. $\tau_n(g) \propto g^{\gamma-1}$), the photoconductivity $\Delta\sigma$ changes in proportion to g^{γ}. If $\gamma < 1$, the lifetime decreases as the generation rate increases, denoted as 'sublinear'. If $\gamma > 1$, the lifetime increases as the

TU Bibliothek WIEN Your knowledge hub
Die approbierte gedruckte Originalversion dieser Dissertation ist an der TU Wien Bibliothek verfügbar.
The approved original version of this doctoral thesis is available in print at TU Wien Bibliothek.

generation rate inclines, referred to as 'superlinear'[66].

(iii) Light-induced change of the carrier mobility, so that

$$\Delta\sigma = nq\Delta\mu \tag{2.72}$$

This behaviour can be explained by the following possible mechanisms

(a) Scattering of hot electrons from charged imperfections may be altered under irradiation, due to the changed density of changed imperfections or an altered scattering cross section thereof[66].

(b) For a polycrystalline material, the intergrain potential barriers at the boundary is significant. In this respect, light irradiation may decrease the height of such the intergrain potential barriers and the depletion width between the adjacent grains, thereby resulting in the increase of charge carrier mobility.

(c) Light irradiation may enable the excitation of charge carriers from one band to another with different mobility.

2.4.2 Characteristic parameters of photodetectors

Some relevant characteristics of photodetectors are listed below

Responsivity (R) A parameter is commonly used to quantify the response efficiency of a photodetector with respect to the optical signal. This parameter defines the photocurrent generated per unit power of the incident light in the effective region of the photodetector in unit time

$$R = \frac{I_{ph}}{P} \tag{2.73}$$

where I_{ph} is the photocurrent generated by the photodetector, P is the effective light power. The responsivity reflects the optoelectronic conversion capacity of photodetectors from the optical signal to an electrical signal, and the unit thereof is $A \cdot W^{-1}$.

The external quantum efficiency (EQE) For common photodetectors, not all the incident photons can be absorbed and subsequently converted into free electrons and hole pairs. In addition, because of the recombination of charge carriers, the photogenerated carriers cannot completely be converted into a photocurrent. EQE is defined as the ratio of output charge carriers to the number of incident photons per unit time, which reflects the luminous efficiency of the whole detector. The specific expression is as follows

$$EQE = \frac{I_{ph/e}}{P/h\nu} = \frac{R}{\lambda} \times \frac{hc}{e} \approx \frac{R}{\lambda} \times \left(1240\ W \cdot \frac{nm}{A}\right) \tag{2.74}$$

where e is the fundamental charge, h is Planck's constant, and ν and λ represent the frequency

Die approbierte gedruckte Originalversion dieser Dissertation ist an der TU Wien Bibliothek verfügbar.
The approved original version of this doctoral thesis is available in print at TU Wien Bibliothek.
TU Bibliothek Your knowledge hub WIEN

and wavelength of the incident light, respectively.

Detectivity (D*) The detectivity takes into account the responsivity and noise of a photodetector. The higher detectivity means the better performance, which is defined as

$$D^* = \frac{(S\Delta f)^{\frac{1}{2}}}{I_{noise}} \tag{2.75}$$

where S is the effective area of the detector, Δf is the electrical bandwidth, and I_{noise} is the total noise current of the detector, including thermal noise, shot noise, generation-recombination (G-R) noise, and 1/f noise[67].

Response time The rise time (τ_r) and fall time (τ_f) of the photocurrent signal are used to characterize the response time of the photodetector to the optical signal. Among them, τ_r(τ_f) defines the rise(fall) time from 10%(90%) to 90%(10%) of the maximum current. In the frequency domain, another parameter named "The 3-dB bandwidth (f_{3dB})" is commonly used to characterize the transient response capacity of the photodetector. In actual experiments, there is no significant difference between these two methods of calculating response time[68]. The 3-dB bandwidth (f_{3dB}) is the frequency at which the detector's photocurrent drops to half of its initial value. The carrier transit time and the RC time constants are two important factors in determining f_{3dB} bandwidth[67].

2.4.3 Internal photoemission

Attempts to quantify internal photoemission were made by R. H. Fowler and W. E. Spicer[69]. Spicer intuitively described the internal photoemission process from a metallic photocathode proceeding via several consecutive steps. Using **Figure 2.23**, the process of internal photoemission in a metal-semiconductor-metal heterostructure is discussed in five steps. In step 1, hot electrons are generated in the metal through the absorption of a photon. In this process, electrons are lifted from states below the Fermi level E_F by the pertinent photon energy hν. The generated hot carriers are assumed to behave as free electrons and that their initial momentum is random. The latter is a reasonable assumption based on the large mismatch between the wave vectors of the light/surface plasmon and the generated hot electron. In step 2, half of the generated hot electrons will move toward the metal/semiconductor interface. Only some of them can arrive at the interface without losing energy in inelastic collisions. The hot electrons arriving at the metal/semiconductor interface with kinetic energy exceeding the barrier Φ_b have a certain probability of being injected into the semiconductor (step 3). This injection probability tends to be small as reflections naturally occur as a result of the large

Die approbierte gedruckte Originalversion dieser Dissertation ist an der TU Wien Bibliothek verfügbar.
The approved original version of this doctoral thesis is available in print at TU Wien Bibliothek.
TU WIEN Bibliothek Your knowledge hub

wave-vector contrast (i.e., impedance mismatch) between electrons in the metal contact and the semiconductor. The electrons that get injected into the semiconductor will move to the opposite electrode and contribute to the current (step 4). Finally, the hot electrons are injected into the opposing metal contact (step 5). However, even at this interface reflections can occur again due to an impedance mismatch.

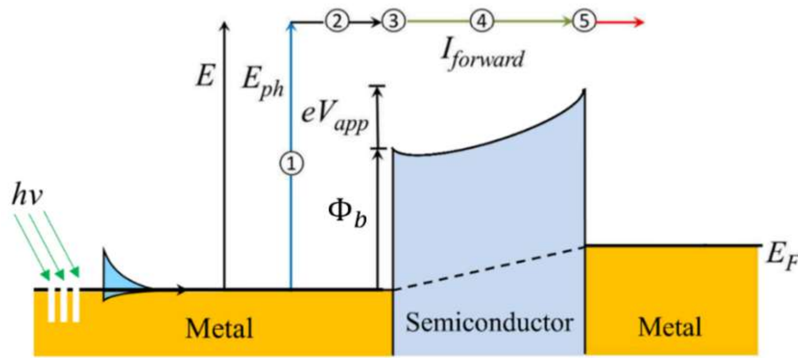

Figure 2.23 Hot electrons transport through a metal-semiconductor-metal back-to-back Schottky diode. It shows the left metal/semiconductor interface with a Fermi level E_F, the barrier height Φ_b. It also illustrates the barrier can be tuned if applying a positive bias voltage V_{app} on the left electrode. Image adapted from Chalab H. et al.[22].

In order to quantify the transmission probability for hot electrons to surmount the Schottky barrier at the metal/semiconductor contact, deriving the momentum of such hot electrons is a necessary step. In principle, knowing the dispersion relationship of metal, the momentum of hot electrons can be calculated from the kinetic energy. With a simplified parabolic approximation, the kinetic energy of hot electrons quadratically depends on momentum, which is given by

$$E_{Kin,m} = E_{F,m} + E = \frac{\hbar^2}{2m_e^*}\left(k_{m,x}^2 + k_{m,y}^2\right) \tag{2.76}$$

where m_e* is the effective mass of hot electrons. $k_{m,x}$ and $k_{m,y}$ are the momenta of hot electrons inside the metal in the x and y directions, respectively (see **Figure 2.24**). This formula is applied to describe the kinetic energy of hot electrons in the step 1 and 2 of **Figure 2.23**. For free hot electrons with a certain energy, their direction is random. In order to involve all the possibility for the momenta of such hot electrons, a circle energy contour is applied (see **Figure 2.24**). Generally, one momentum can be split into the horizontal and perpendicular components in the x and y directions respectively, thus

$$k_m^2 = k_{m,x}^2 + k_{m,y}^2 \tag{2.77}$$

Die approbierte gedruckte Originalversion dieser Dissertation ist an der TU Wien Bibliothek verfügbar.
The approved original version of this doctoral thesis is available in print at TU Wien Bibliothek.
TU Bibliothek WIEN Your knowledge hub

In step 3 of **Figure 2.23**, where hot carriers are injected into the semiconductor, due to the mismatch of dielectric constant, both the kinetic energy and momentum of hot carriers would alter. The changed kinetic energy of such injected hot carriers in the semiconductor can be expressed as

$$E_{kin,s} = E - \Phi_b = \frac{\hbar^2}{2m_e^*}\left(k_{s,x}^2 + k_{s,y}^2\right) \tag{2.78}$$

with $E_{Kin,s}$ the kinetic energy of hot electrons in the semiconductor, $k_{s,x}$ and $k_{s,y}$ are the momenta of hot electrons inside the semiconductor in the x and y directions, respectively.

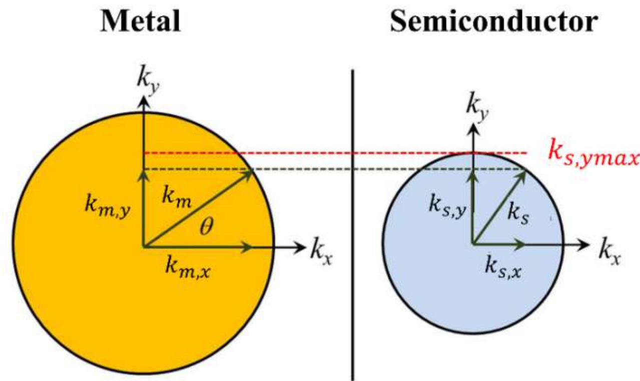

Figure 2.24 The injection of hot electrons from the metal to the semiconductor requires momentum conservation. The circle contour represents all the possible directions of hot electron momenta. The different sizes of the metal and semiconductor is contributed to the mismatch of the dielectric constant. Image adapted from [22].

Similarly, the total momentum of the hot carrier in the semiconductor is given by

$$k_s^2 = k_{s,x}^2 + k_{s,y}^2 \tag{2.79}$$

Only an electron with kinetic energy higher than the Schottky barrier can be injected into the semiconductor, i.e. $E_{kin,s} = E - \Phi_b > 0$. In analogy to the behaviours of the photons at a diffraction interface, the perpendicular component of the electron momentum should be unchanged while hot electrons are injected from the metal to the semiconductor (i.e. $k_{m,y} = k_{s,y} \equiv k_y$)[22]. However, the horizontal component of the hot electrons is different (i.e. $k_{m,y} \neq k_{s,y}$), due to the mismatch of dielectric constant between the metal and the semiconductor. In this respect, only the hot electrons moving the proper direction can be injected. Further, the group of the allowed direction is referred to as the escape cone (see **Figure 2.24**). Only hot electrons within the escape cone have the possibility to be injected into the semiconductor, otherwise would be reflected back.

Die approbierte gedruckte Originalversion dieser Dissertation ist an der TU Wien Bibliothek verfügbar.
The approved original version of this doctoral thesis is available in print at TU Wien Bibliothek.
TU Wien Bibliothek Your knowledge hub

Therefore, the escape possibility P_{esc} can be given by

$$P_{esc} = \frac{2\pi sin\theta d\theta}{4\pi} = \frac{k_y dk_y}{2k_m\sqrt{k_m^2 - k_y^2}} \tag{2.80}$$

with θ the angle sinθ = k_y/k_m. Further, the transmission probability across the left metal-semiconductor interface can be derived as

$$\mathcal{T}_1 = \frac{4k_{m,x}k_{s,x}}{(k_{m,x}+k_{s,x})^2} = \frac{\sqrt[4]{(k_m^2-k_y^2)(k_s^2-k_y^2)}}{\left(\sqrt{k_m^2-k_y^2}+\sqrt{k_s^2-k_y^2}\right)^2} \tag{2.81}$$

Consequently, the total probability in step 3 in **Figure 2.23** is then given by

$$P_1 = \int_0^{K_s(E)} \frac{\sqrt[4]{(k_m^2-k_y^2)(k_s^2-k_y^2)}}{\left(\sqrt{k_m^2-k_y^2}+\sqrt{k_s^2-k_y^2}\right)^2} \frac{k_y}{2k_m\sqrt{k_m^2-k_y^2}} dk_y \tag{2.82}$$

The probability that an electron entering the semiconductor film makes it across the semiconductor via drift or diffusion is assumed as P_2 (see step 4 in **Figure 2.23**).

After moving across the semiconductor, the kinetic energy of these electrons will change, and the magnitude is determined by the applied bias, which is given by

$$E_{kin,s'} = E - \Phi_b + eV = \frac{\hbar^2}{2m_e^*}\left(k_{m',x}^2 + k_{m',y}^2\right) \tag{2.83}$$

Like the left interface, the injection of these hot electrons will occur again at the right interface (see step 5 in **Figure 2.23**). Therefore, kinetic energy of these electrons allowed to pass the right interface should meet

$$E_{kin,m'} = E_F + E + eV = \frac{\hbar^2}{2m_e^*}\left(k_{m',x}^2 + k_{m',y}^2\right) \tag{2.84}$$

Further, a transmission probability is given by

$$P_3 = \int_0^{K_{s'}(E)} \frac{\sqrt[4]{(k_{s'}^2-k_y^2)(k_{s'}^2-k_y^2)}}{\left(\sqrt{k_{s'}^2-k_y^2}+\sqrt{k_{s'}^2-k_y^2}\right)^2} \frac{k_y}{2k_{s'}\sqrt{k_{s'}^2-k_y^2}} dk_y \tag{2.85}$$

Simplifying the model by assuming the non-occurrence of multiple reflections of hot electrons between two interfaces, the total transmission probability becomes

$$P_{tot}(E) = P_1 P_2 P_3 \tag{2.86}$$

Furthermore, as only hot electrons with the energy E exceeding the barrier energy Φ_b can surmount the barrier, the internal quantum efficiency is given by

$$\eta_i(E_{ph}) = \frac{1}{E_{ph}} \int_{\Phi_b}^{E_{ph}} P_{tot}(E)\, dE \tag{2.87}$$

Die approbierte gedruckte Originalversion dieser Dissertation ist an der TU Wien Bibliothek verfügbar.
The approved original version of this doctoral thesis is available in print at TU Wien Bibliothek.
TU Bibliothek WIEN Your knowledge hub

Chapter 3

Experimental techniques

This chapter covers the methods applied in the device fabrication and the electrical and electro-optical measurements for metal-semiconductor-metal heterostructure devices. The first section depicts the top-down process for fabricating metal-semiconductor-metal heterostructures and their integration in back-gated FET architectures. Furthermore, the second part of the chapter introduces the electrical measurement setups for characterizing the FETs. Finally, the electro-optical measurements are discussed, including scanning photocurrent microscopy and a modified pump-probe cross-correlation technique.

Die approbierte gedruckte Originalversion dieser Dissertation ist an der TU Wien Bibliothek verfügbar.
The approved original version of this doctoral thesis is available in print at TU Wien Bibliothek.
TU WIEN Bibliothek Your knowledge hub

3.1 Device fabrication

A standard top-down technique was employed to fabricate monolithic metal-semiconductor-metal heterostructure devices. The main processing steps for device fabrication are depicted in **Figure 3.1**.

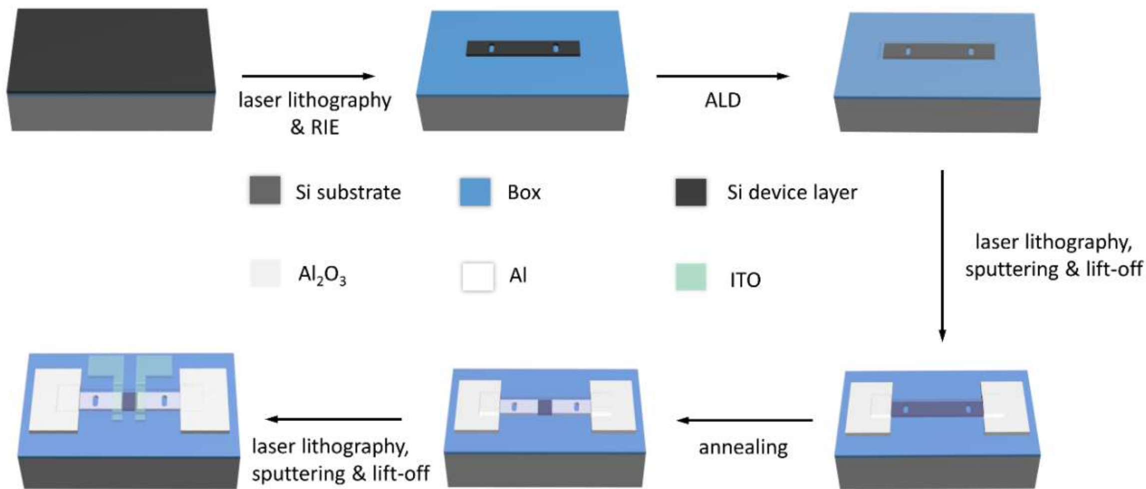

Figure 3.1 Schematic diagram shows the process flow for the fabrication of the Al-Si-Al heterostructure device.

The detailed fabrication steps are described below

Step 1: The sample, cut from a commercial SOI wafer, is coated with photoresist (AZ5214E) at the rotation speed of 6000 rpm for 40 s, and then a softbake is carried out at 374 K for 60 s. The pattern - micro-ribbons with two oval shaped trenches - is transferred by laser lithography and subsequent reactive ion etching (RIE). The RIE step was performed in an Oxford PlasmaPro 100 Cobra ICP etching system at 309 K for 150 s. The gas flow rates of SF_6 and O_2 are set as 50 sccm and 10 sccm, respectively. Afterward, the sample is rinsed with acetone and isopropanol, then treated by oxygen plasma etching to carefully remove the residues of the photoresist.

Step 2: a 12 nm thick Al_2O_3 is deposited on the patterned sample via atomic layer deposition (ALD) at 474 K. This Al_2O_3 layer passivates the surface of Si microbars, and further serves as the gate dielectric for the split gates.

Step 3: Al contact pads are patterned using laser lithography again. Before Al deposition, the sample is immersed in BHF (7:1) for 30 s to remove the Al_2O_3 and the native SiO_2 at the contact area. Then the sample is immediately inserted in the sputtering machine to avoid reoxidation. The metallization is finalized by 125 nm thick Al sputter deposition and lift-off in acetone at

Die approbierte gedruckte Originalversion dieser Dissertation ist an der TU Wien Bibliothek verfügbar.
The approved original version of this doctoral thesis is available in print at TU Wien Bibliothek.
TU WIEN Bibliothek Your knowledge hub

329 K for 1 h.

Step 4: Rapid thermal annealing at T = 774 K in a forming-gas atmosphere (90% N_2/10% H_2) induces the substitution of Si by Al, which enables to control the Si channel length by the annealing duration. During the Al-Si exchange the oval-shaped trenches originally etched in the Si micro-ribbons become oval recesses in the crystalline Al feed lines.

Step 5: 125 nm thick ITO split-gates are realized using laser lithography, ITO sputtering and lift-off techniques.

It is worthwhile to mention that such standard CMOS-compatible process can be applied to fabricate Al-Ge-Al heterostructures as well, based on a GeOI wafer substrate. In the etching process for Ge, the buffered HF needs to be replaced by hydrogen iodide (HI) acid. Further, the annealing temperature triggering the Al-Ge exchange only requires 674 K.

Die approbierte gedruckte Originalversion dieser Dissertation ist an der TU Wien Bibliothek verfügbar.
The approved original version of this doctoral thesis is available in print at TU Wien Bibliothek.
TU WIEN Bibliothek Your knowledge hub

3.2 Electrical characterization techniques

3.2.1 Output measurements

The heterostructure devices fabricated on GeOI or SOI resemble back-gated SBFETs[70], with the highly doped handle wafer acting as the common back-gate and the two Al pads as the source and drain electrodes, respectively. For electrical measurements the sample is mounted to a Cu slide using silver conductive paint. In addition, a glass slide was employed as the global substrate carrying the small Cu slide with the overall sample and a PCB, all glued by an epoxy resin-based adhesive. To realize electrical contacts, it requires bonding of the two Al pads of the heterostructure device as well as the Cu slide to the PCB via Au wires, as depicted in **Figure 3.2**.

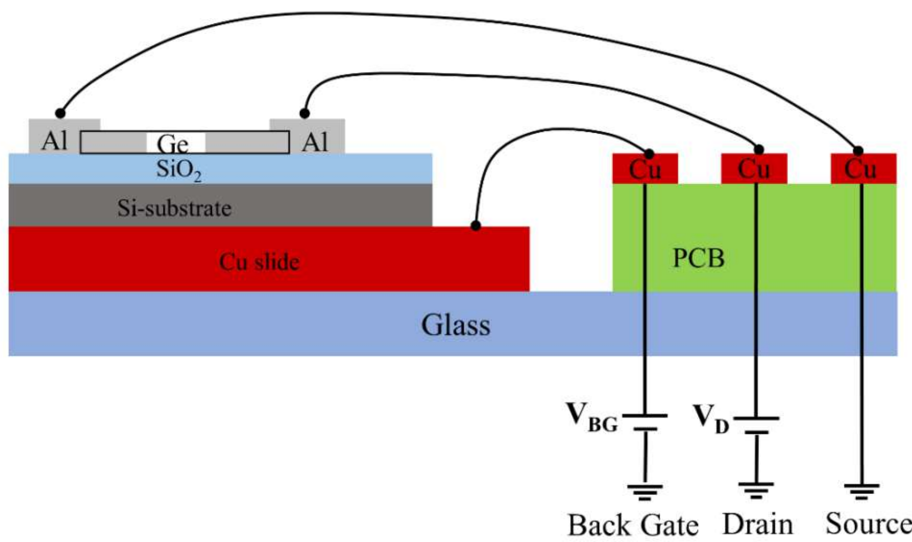

Figure 3.2 Schematic diagram of the electrical measurement setup for current/voltage measurements of an Al-Ge-Al heterostructure device.

Consequently, the contact pads on the PCB were connected to source measure units (SMU) of a semiconductor analyzer (Keysight B1500A). To investigate the contact properties and resistivity of heterostructure devices, two terminal current/voltage (I/V) sweeps were performed. In order to simplify the analysis process for distinguishing hot electrons and hot holes, the grounded electrode is always defined as source. A positive drain bias V_D thus generates a positive drain current I_D, suggesting electrons moving toward the side of the drain electrode as well. Another crucial point of concern is the allowed maximum voltage, which is limited by the breakdown field strength of Ge (i.e. $E_{Ge,max} = 10$ mV·nm^{-1} [71]) and Si (i.e. $E_{Si,max} = 30$ mV·nm^{-1} [71]).

Die approbierte gedruckte Originalversion dieser Dissertation ist an der TU Wien Bibliothek verfügbar.
The approved original version of this doctoral thesis is available in print at TU Wien Bibliothek.
TU WIEN Bibliothek Your knowledge hub

3.2.2 Transfer measurements

As mentioned above, the heterostructure devices shown in **Figure 3.2** resembles a back-gated SBFET. To ensure reliable measurements, the currents I_S, I_D and I_{BG} were recorded simultaneously. The transfer characteristic of a SBFET present a plot of input back-gate voltage V_{BG} as the function of output drain current I_D. On the count of some Al-Ge-Al heterostructure devices with ultra-short Ge segment (e.g. below 1 μm), the applied drain voltage V_D ranges typically between 1 mV and 100 mV. In contrast, Al-Si-Al heterostructure devices are designed to have a long Si segment, providing enough space for split gates. Therefore, a large drain voltage, even V_D = 1 V, is allowed to applied on the Al-Si-Al heterostructures. In order to diminish the charging effects originated from parasitic capacities, the initial hold time and the delay time among the adjacent points were set as 5 s and 250 ms, respectively. So-called double sweeps comprising the forward- and reverse direction were employed to characterize the hysteresis effects originated from charge carrier trapping.

3.2.3 Temperature dependent electrical measurements

Temperature-dependent measurements were performed to derive the Schottky barrier height Φ_{SB} for the SBFETs. A probe station (Lake Shore Cryotronics) with a temperature controller was employed. Needle probes directly connected to the drain and source electrodes of the SBFET as well as the Cu slide for the back gate contact. The typical temperature range was set between 273 K and 380 K. Before starting electrical measurements, it required waiting for 10 min making the temperature stable.

Richardson plotting is a common and convenient technique, used to extract Schottky barrier height. One demonstration of deriving the Schottky barrier height from temperature-dependent current-voltage curves of an Al-Ge-Al heterostructure device is shown in **Figure 3.3**. **Figure 3.3a** demonstrates I/V curves of an Al-Ge-Al SBFET at various temperatures at the back-gate voltage of V_{BG} = 0 V. It can be clearly seen that higher temperature inducts larger drain current I_D for all the drain bias V_D. The thermionic theory is often applied to extract the Schottky barrier height. Thermionic emission current density J_{TE} follows

$$J_{TE} = A^{*}T^{2}\, exp\, exp\left(-\frac{q\Phi_{SB}}{kT}\right) \quad (3.1)$$

where T is the applied temperature, A∗ is the effective Richardson constant, k is the Boltzmann constant.

Die approbierte gedruckte Originalversion dieser Dissertation ist an der TU Wien Bibliothek verfügbar.
The approved original version of this doctoral thesis is available in print at TU Wien Bibliothek.
TU WIEN Bibliothek Your knowledge hub

As the precise value of the Richardson constant for the Al-Ge-Al heterostructure, the previous equation needs to be reformulated as

$$ln\left(\frac{J_{TE}}{T^2}\right) = -\frac{q\Phi_{SB}}{kT} + ln\,(A^*) \tag{3.2}$$

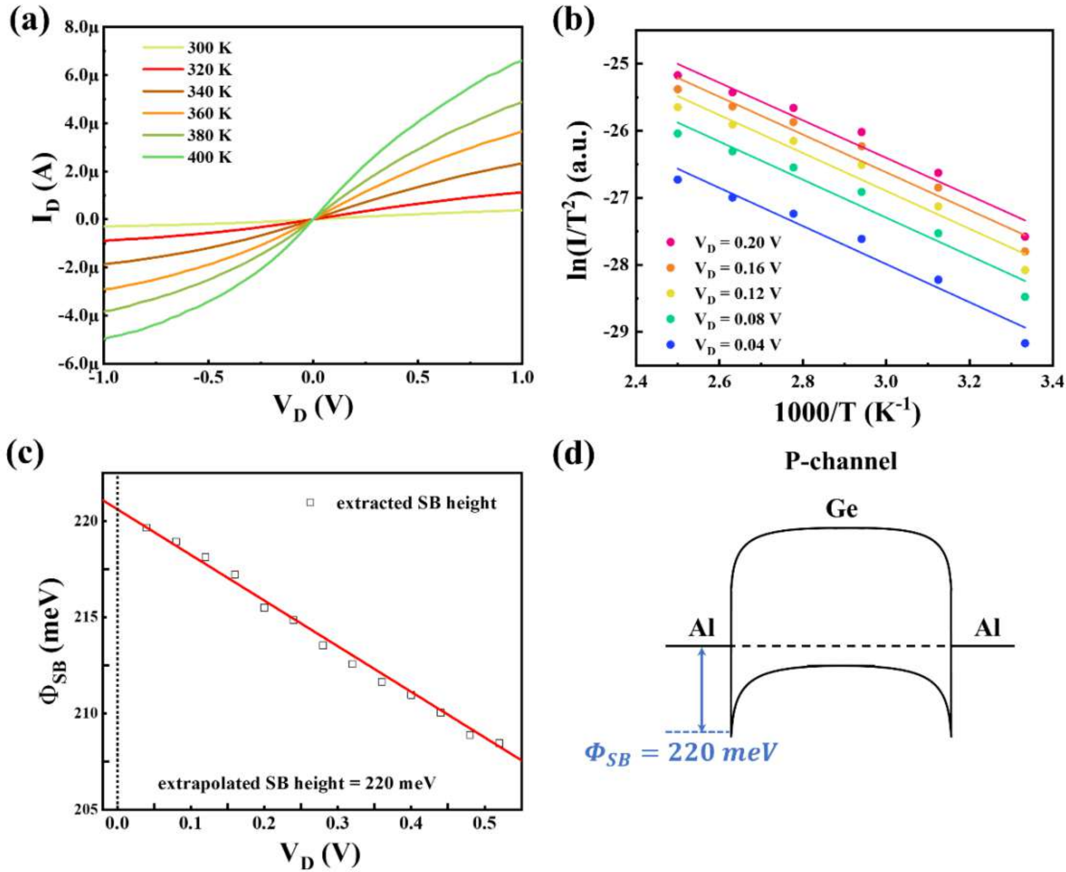

Figure 3.3 (a) I/V curves of one Al-Ge-Al heterostructure measured at various temperatures and the back-gate voltage of $V_{BG} = 0$ V. (b) Richardson plots under different drain bias V_D. (c) Derived Schottky barrier height at different drain bias V_D. The Schottky barrier height Φ_{SB} can be obtained by the linear fitting and then extracted from the value at a drain bias of $V_D = 0$ V. (d) Band diagram of back-to-back Schottky barrier diode.

Afterward the Schottky barrier height Φ_{SB} can be derived from the slope of a linear fitting if plotting ln (J_{TE}/T^2) as the function of 1000/T (i.e. Richardson plot) at certain drain voltage V_D (**Figure 3.3b**). Subsequently, the Schottky barrier height Φ_{SB} is further plotted as the function of the applied drain voltage V_D (**Figure 3.3c**). Finally, the linear fitting is applied again to extrapolate the points to $V_D = 0$ V, producing an effective barrier height of 220 meV at the back-gate voltage of $V_{BG} = 0$ V. **Figure 3.3d** illustrates the energy band of Al-Ge-Al heterostructure at $V_{BG} = 0$ V, demonstrating a Fermi level close to the valence band.

Die approbierte gedruckte Originalversion dieser Dissertation ist an der TU Wien Bibliothek verfügbar.
The approved original version of this doctoral thesis is available in print at TU Wien Bibliothek.
TU Bibliothek Your knowledge hub WIEN

3.3 Optoelectronic characterization

3.3.1 Characterization of photodetectors

A µ-Raman microscopy system (Witec Alpha 300) with a frequency doubled Nd: YAG laser (λ = 532 nm) and a near-infrared He/Ne laser (785 nm) was used as the light source. The high-resolution microscopy allowed precise alignment of the light spot with the target part of the heterostructure device (e.g. the plasmon antenna). The standard photodetection characterization mainly involved two types, namely light power dependent and wavelength dependent measurements. The output power of both laser sources can be adjusted from 0.1 µW to 10 mW, which is calibrated by a commercial Si photodiode. In the IR region, the light power was calibrated by a commercial Ge photodiode. For wavelength dependent measurements, a tunable-wavelength laser (SuperK Extreme, NKT) assisted with a monochromatic system (NKT SuperK Select acoustic-optical tunable filter), ranging from 500 nm to 1600 nm, was coupled into the microscope. In order to keep the same light density for all the wavelength, the light power was normalized to the area of the light spot.

3.3.2 Scanning photocurrent microscopy technique

Scanning photocurrent microscopy (SPCM) is commonly applied to characterize the local optoelectronic features of semiconductor nanostructures. The scanning photocurrent microscopy setup mainly relies on a commercial µ-Raman microscopy system (Witec Alpha 300), which involves a piezo stage, a high-resolution objective (Zeiss 100x) and a synchronous signal recording management software. **Figure 3.4** depicts the setup of scanning photocurrent microscopy. The heterostructure device was fixed on a moveable sample holder, which was further mounted on the piezo stage. The piezo stage can move in two motorized axes (i.e. x and y axis) with a maximum range of 50 µm and be automatically controlled by the software of Witec Alpha 300 system when running the SPCM measurement. Due to the good light confining ability of the Zeiss 100x objective, a light beam with a diameter of 865 nm can be realized via the 532 nm laser. The generated photocurrent was amplified and meanwhile converted into a voltage signal, which finally was recorded as a function of the position. To modulate the gate voltage, a DC power supply (Keithley 2635A system sourcemeter) was used to control gate biasing.

TU Bibliothek. WIEN Your knowledge hub
Die approbierte gedruckte Originalversion dieser Dissertation ist an der TU Wien Bibliothek verfügbar.
The approved original version of this doctoral thesis is available in print at TU Wien Bibliothek.

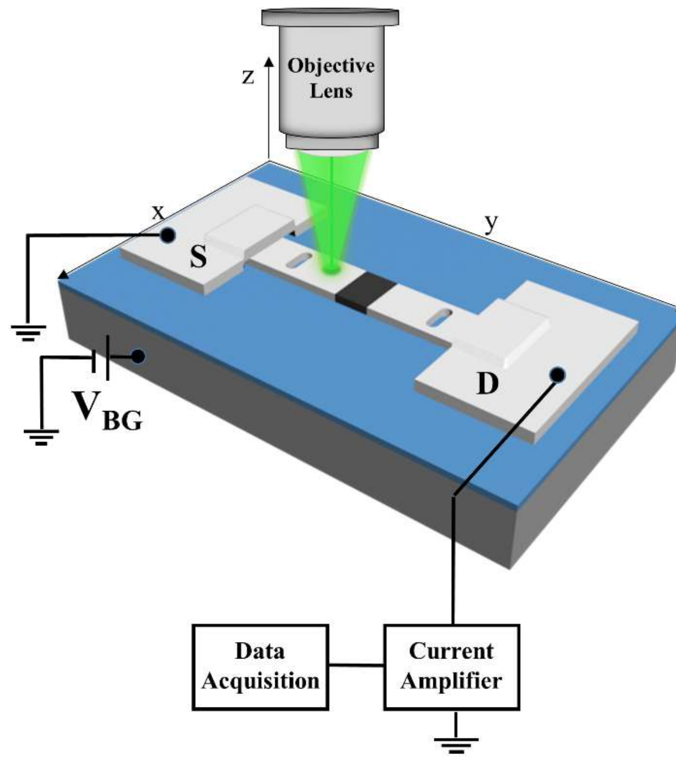

Figure 3.4 Schematic diagram of the scanning photocurrent measurement setup.

3.3.3 Pump-probe cross-correlation measurement

Pump-probe cross-correlation spectroscopy is widely applied to investigate the ultrafast dynamics of charge carriers in semiconductors. Generally, this technique requires splitting of an ultrashort laser pulse into two portions. One light beam called the pump would excite charge carriers to a non-equilibrium state, subsequently, the other one (probe) is applied to display the pump-induced difference of the optical constants (e.g. absorption or reflectivity). Normally the measured pump-probe spectroscopy measures the changes of the optical parameter as a function of the time delay between the arrival of pump and probe pulses, indicating the dispersion of electronic states in the semiconductor material. In the conventional pump-probe setup, it needs a highly sensitive photodiode as an optical receiver to detect the light passed through (or reflected from) the semiconductor sample. In this work, a modified pump-probe setup was used, in which the Al-Ge-Al heterostructure was directly employed as the optical receiver. **Figure 3.5** illustrates schematically the pump-probe cross-correlation setup.

Die approbierte gedruckte Originalversion dieser Dissertation ist an der TU Wien Bibliothek verfügbar.
The approved original version of this doctoral thesis is available in print at TU Wien Bibliothek.
TU Bibliothek Your knowledge hub WIEN

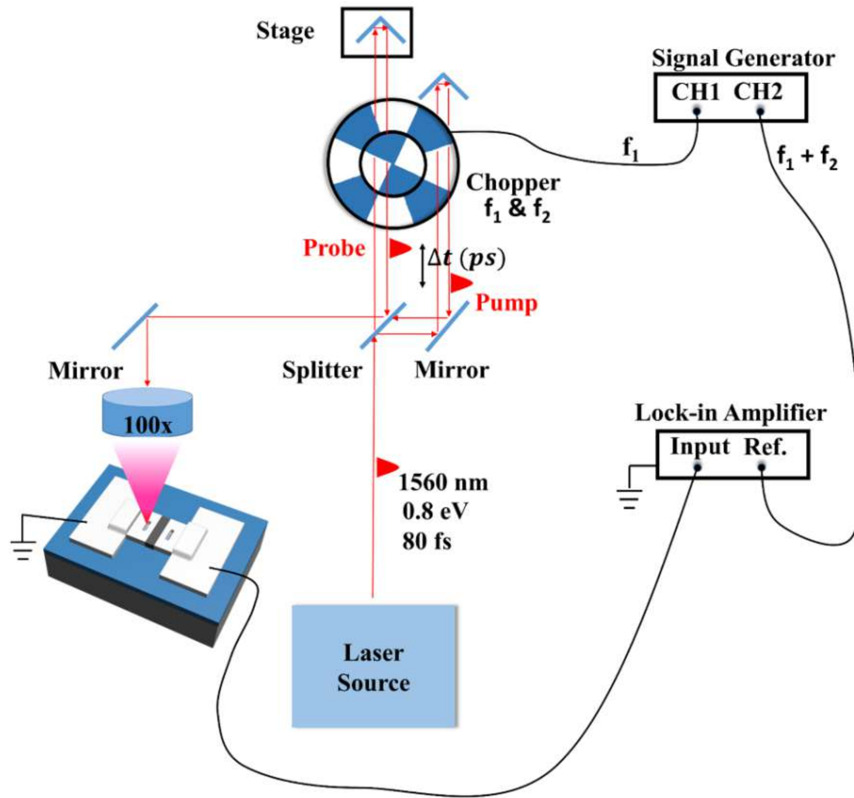

Figure 3.5 Schematic diagram of the modified pump-probe cross-correlation setup, in which the change of electrical signal of the hot-carrier photodetectors is directly recorded.

In the pump-probe setup, a femtosecond laser (Toptica FemtoFiber Pro) with the wavelength of 1560 nm and the pulse width of 90 fs is employed as a laser source, which can generate a pulse train with a repetition rate of 80 MHz, corresponding to the interval duration between two adjacent pulses of 12.5 ns. Subsequently, a 50/50 beam splitter is used to split the pulse train into two beams. To simplify the description such two pulse trains in the remaining text are named as pump pulse and probe pulse trains. Subsequently, both the pump pulse and probe pulse trains pass through a mechanical chopper (Thorlabs M2000 optical chopper) having two different chopping sections with frequencies f_1 and f_2, respectively, thus pulse trains are amplitude modulated at different frequencies f_1 and f_2 that are phase locked. While the pump pulse train travels a consistent distance, the traveling distance of the probe pulse train would be modulated via a mechanical delay line. It enables a delay time from zero to 300 ps with a resolution of 66 fs. Then, these two pump and probe pulse trains are merged again in an optical fiber and focused on the target region of the Al-Ge-Al heterostructure device by using a high-resolution microscopy (Witec Alpha 300 equipped with Nikon 100x objective). Finally, a digital lock-in amplifier (Model SR830 DSP Lock-in Amplifier) was inducted to process detector signal, to enhance the signal-to-noise ratio. The corresponding frequency for a lock-

Die approbierte gedruckte Originalversion dieser Dissertation ist an der TU Wien Bibliothek verfügbar.
The approved original version of this doctoral thesis is available in print at TU Wien Bibliothek.
TU Bibliothek Your knowledge hub WIEN

in amplifier is set to $f_1 \pm f_2$ to record the pump-probe signal. The related working principle of the pump-probe cross-correlation measurement is illustrated in **Figure 3.6**.

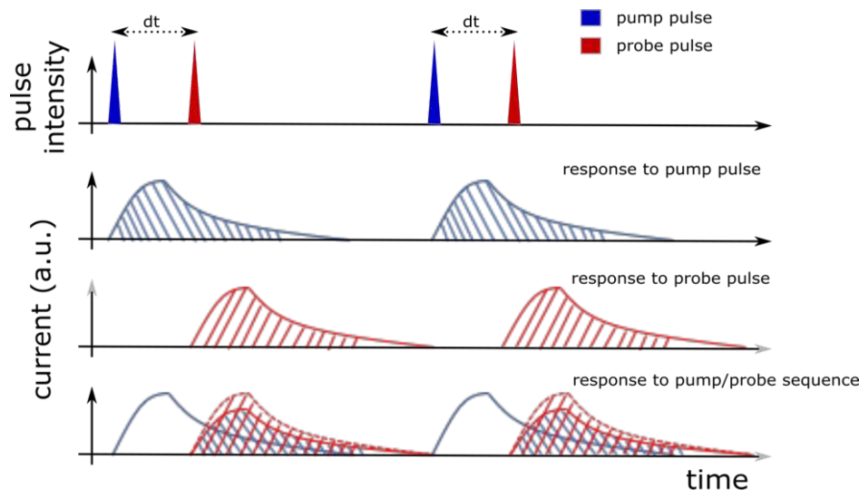

Figure 3.6 The working principle of pump-probe cross-correlation measurement.

Generally, it allows two different modes in which light pulses can interact with a detector (i) the two pump and probe pulses simultaneously irradiate a detector. In other words, they completely overlap with each other in the time domain. Therefore, two pulses can be regarded as one pulse, and the intensity is the sum of two individual pulses. Compared to the single pulse, the detector responds to the combined electric field of the two pulses. However, if the resulting intensity of the pulses is too high, the response of photodetector becomes non-linear; (ii) each pulse irradiates a detector at different time instances. In this case, there is no overlap of two pulses in the time domain. Interestingly, the pump probe as the first one interacts with an initial detector without any perturbation from light, while the probe pulse as the second one interacts with a perturbed detector. The amount of perturbation is determined by the time delay between two pulses, as well as the recovery speed for the detector returning to the steady state after being excited by the pump pulse.

In principle, when the pump pulse interacts with an unperturbed detector in the steady-state, the induced electrical signal S_D is comprised of several contributors (i), due to various independent processes in the device, which can be expressed as

$$S_D(t) = \sum_i A_i \cdot \left(1 - exp\left(-\frac{t}{\tau_{Ri}}\right)\right) \cdot exp\left(-\frac{t}{\tau_i}\right) \tag{3.3}$$

with A_i the magnitude of the individual contributor, τ_{Ri} the rise time and τ_i the decay time of each process.

Die approbierte gedruckte Originalversion dieser Dissertation ist an der TU Wien Bibliothek verfügbar.
The approved original version of this doctoral thesis is available in print at TU Wien Bibliothek.
TU Bibliothek Your knowledge hub WIEN

Subsequently, the probe pulse impinges the perturbed detector which did not yet recover back to the steady state, normally generating a weaker response. With the assumption of the first approximation, the response can be described as

$$S'_D(t) = \sum_i \left(A_i - \Delta A_i(\Delta t_{pp})\right) \cdot \left(1 - exp\left(-\frac{t}{\tau_{Ri}}\right)\right) \cdot exp\left(-\frac{t}{\tau_i}\right) \qquad (3.4)$$

with Δt_{pp} the time delay between the pump and probe pulses and ΔA_i an effective reduction of the detector response with the preceding pump pulse. In the case of a photon detector, the restoration of the intrinsic response is reached when the energy deposited by a light pulse is removed from the detector volume. It includes the removal of photogenerated electrons and holes, the dissipation of generated phonons to a heat sink, and the restoration of charge neutrality in the detector total volume including the detector terminals.

Therefore, the pump-probe cross-correlation technique characterizes the difference between $S_D(t)$ and $S'_D(t)$

$$\Delta S_D(t, \Delta t_{pp}) = \sum_i \Delta A_i(\Delta t_{pp}) \cdot \left(1 - exp\left(-\frac{t}{\tau_{Ri}}\right)\right) \cdot exp\left(-\frac{t}{\tau_i}\right) \qquad (3.5)$$

and its change as a function of the time delay Δt_{pp} between pump and probe pulses. Noteworthy is, that it carries the same signal dynamics as the original detector response.

Instead of ultrafast sampling of the detector signal on its terminals with a ps time resolution is integrated as the function of time by a lock-in amplifier. Thereby, the obtained signal is proportional to ΔA_i and it decreases with the increasing time delay Δt_{pp} between the pump and probe pulses. Formally, it can be expressed as

$$S_{LIA}(\Delta t_{pp}) \propto \sum_i S_i \cdot exp\left(-\frac{t_{pp}}{\tau_i}\right) \qquad (3.6)$$

so as a sum of several exponential decays reflecting all time-inertial processes in the detector. Additionally, it is necessary to prove the overall temporal resolution limitation of this pump-probe setup, and the result is depicted in **Figure 3.7**.

Die approbierte gedruckte Originalversion dieser Dissertation ist an der TU Wien Bibliothek verfügbar.
The approved original version of this doctoral thesis is available in print at TU Wien Bibliothek.
TU Bibliothek WIEN Your knowledge hub

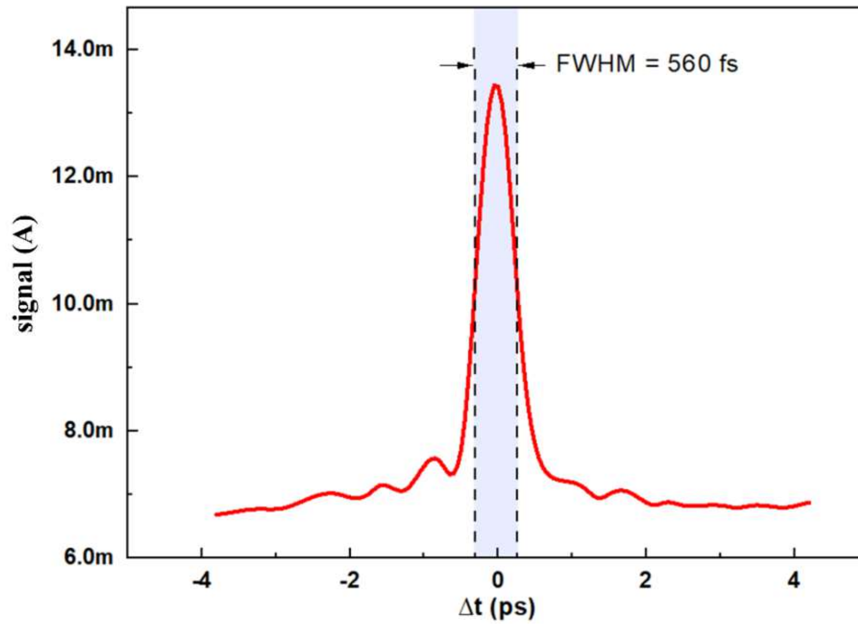

Figure 3.7 The resolution limitation of the pump-probe setup, determined by an autocorrelation measurement of a commercial InGaAs ultrafast photodiode.

To estimate the length of the excitation pulses directly at the photodetector, an autocorrelation measurement[72] was inducted with an ultrafast InGaAs ultrafast photodiode (Thorlabs APD430C) placed below the microscope objective. The measured signal corresponds to the non-linear combination of the intensity of two pulses. Extraction of the full width at half maximum (FWHM) of about ~560 fs indicates the broadening of the laser pulses (with FWHM of 90 fs) mainly due to the dispersion in lenses and beam splitters in the microscope. The value of 560 fs can thus be considered as the maximum achievable time resolution of our pump-probe setup unless an optical non-linear process in the detector is involved.

TU Bibliothek WIEN Your knowledge hub
Die approbierte gedruckte Originalversion dieser Dissertation ist an der TU Wien Bibliothek verfügbar.
The approved original version of this doctoral thesis is available in print at TU Wien Bibliothek.

Chapter 4

Results and Discussion

In this chapter, according to the two material systems investigated, the main experimental results obtained within this PhD thesis will be divided into two parts: Al-Ge-Al and Al-Si-Al heterostructure. Both parts will be introduced sequentially, starting with the heterostructure formation, followed by a discussion of the basic electrical properties, and finally focused on their device application. The Al-Ge-Al heterostructure are applied for polarization-sensitive and ultrafast photodetection. Further for rather unconventional physical phenomena, including negative photoconductance and hot-carrier detection following a superlinear current-power law. The Al-Si-Al heterostructure device exhibits the ability to modulate the injection of SPP-induced hot carriers, which demonstrates considerable potential for the realization of on-chip photovoltaics.

Die approbierte gedruckte Originalversion dieser Dissertation ist an der TU Wien Bibliothek verfügbar.
The approved original version of this doctoral thesis is available in print at TU Wien Bibliothek.
TU WIEN Bibliothek Your knowledge hub

4.1 Al-Ge-Al heterostructures

4.1.1 The formation of Al-Ge-Al heterostructure devices

A standard CMOS-compatible fabrication process, already mentioned in the experiment section (please see **Chapter 3.1**), is employed to resemble the Al-Ge-Al heterostructure. The GeOI wafer applied in this case comprises a 75 nm thick intrinsic Ge device layer, a thermal SiO_2 layer with a thickness of 150 nm and a highly doped handle wafer. Firstly, the device layer of the GeOI is patterned into Ge ribbons via standard photolithography and RIE. Afterwards, two Al pads are deposited on the terminals of the Ge nanosheets by photolithography, sputtering and lift-off techniques. Finally, rapid thermal annealing in forming gas at 673 K induces a thermal-activated Al-Ge exchange reaction, resulting in Al-Ge-Al heterostructures. **Figure 4.1a** shows the initial device with a Ge channel length of 5.9 µm with Al pads deposited via plasma-enhanced sputtering.

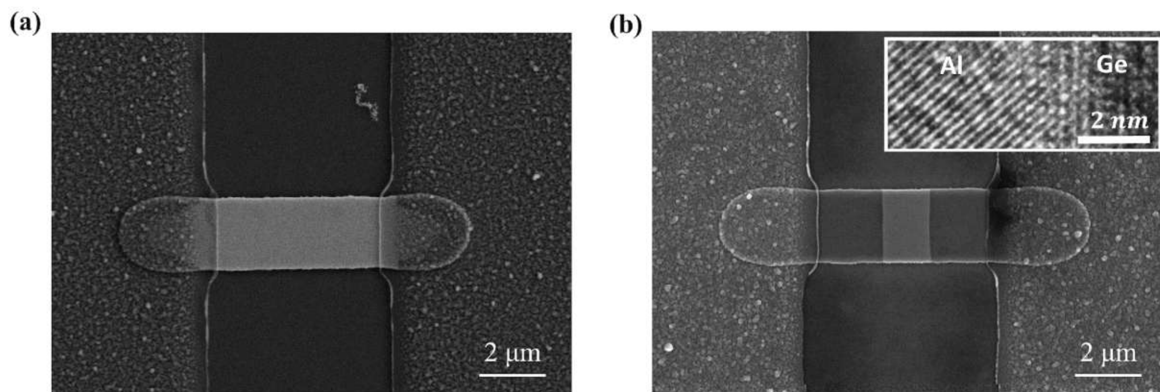

Figure 4.1 (a) SEM image of the initial Ge nanosheet with sputter-deposited Al pads and (b) the resulting heterostructure after annealing at 673 K for 5 min. The right-upper inset shows a TEM image of the Al/Ge interface.

For thus fabricated devices, the active device channel length is determined by photolithography, therefore an advanced processing is required to achieve ultra-short channel lengths. **Figure 4.1b** depicts the fabricated Al-Ge-Al heterostructure device with a reduced channel length of L_{Ge} = 1.4 µm after annealing at 673 K for 300 s. Generally, for a conventional metal/semiconductor contact, an abrupt interface is required to minimize the impact of interface states on the electrical properties of the Schottky contact. Here, an atomically abrupt interface is obtained via the Al-Ge exchanged reaction as shown in the TEM image in the inset of **Figure 4.1b**. According to the previous report[73], during the exchange reaction, Ge from the interface diffuses through the Al into the large deposited contact pads and Al atoms diffuse into the Ge

Die approbierte gedruckte Originalversion dieser Dissertation ist an der TU Wien Bibliothek verfügbar.
The approved original version of this doctoral thesis is available in print at TU Wien Bibliothek.
TU WIEN Bibliothek Your knowledge hub

segment occupying the initial position of Ge atoms. The diffusion mainly runs in one direction, due to the distinctly different diffusion coefficients of Ge in Al and vice versa[74,75]. Thus, the channel length depends on the annealing time, which can even be scaled down below L_{Ge} = 100 nm[76].

As previously stated, implementing the Al/Ge exchange process is a practical approach to form Al-Ge-Al heterostructure SBFETs with a reduced channel length, compared to the channel length determined by photolithographic restrictions[73]. **Figure 4.2** illustrates different designs with various channel lengths determined by photolithography, as well as the resulting Al-Ge-Al heterostructure after implementing the Al/Ge exchange process.

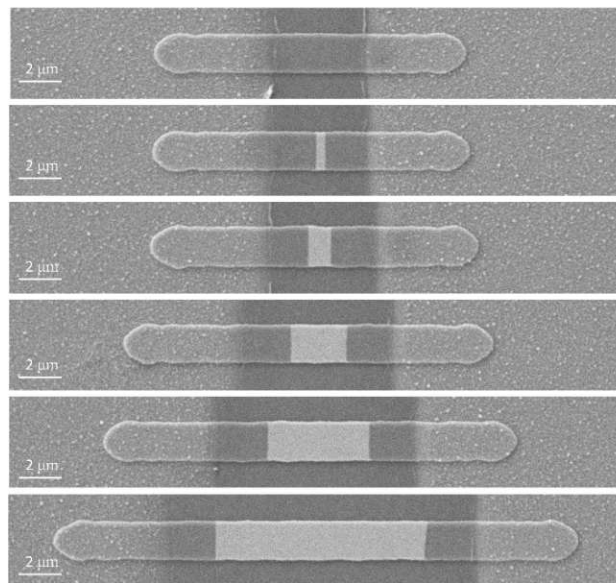

Figure 4.2 SEM images of Al-Ge-Al heterostructure device with different channel lengths L_{Ge}.

As the diffusion length of Al is determined by the annealing time, varying the predesigned lengths of devices on the same chip can result in the different lengths of the remaining Ge segment L_{Ge} after the thermally induced exchange reaction. However, if the predesigned length is too short, Ge will be completely substituted by Al, resulting in complete exchange and thus a continuous Al film (see uppermost SEM image in **Figure 4.2**). In order to investigate the impact of annealing, the surface roughness for the different parts of the Al-Ge-Al heterostructure devices is characterized via the atomic force microscopy, including the sputtered Al pads, Al feed line formed during the exchange reaction and the remaining Ge segment (see **Figure 4.3**).

Die approbierte gedruckte Originalversion dieser Dissertation ist an der TU Wien Bibliothek verfügbar.
The approved original version of this doctoral thesis is available in print at TU Wien Bibliothek.
TU WIEN Bibliothek Your knowledge hub

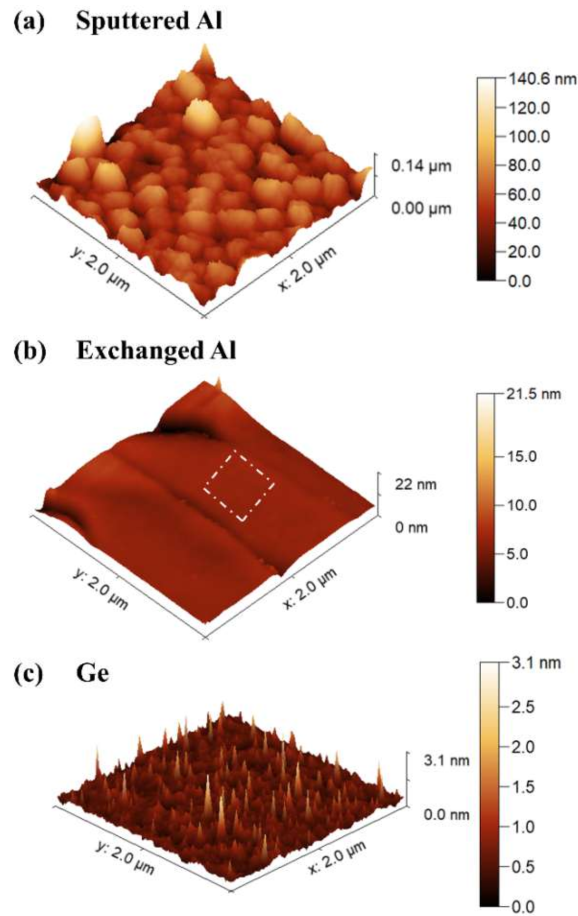

Figure 4.3 AFM topography plot showing the surface roughness of sputtered Al pad (a), exchanged Al feed line (b) and Ge segment (c). The dashed box in panel **b** highlights the region used to calculate RMS.

Sputterred Al pads feature an RMS of almost 20 nm. The surface of Ge is extremely flat (RMS = 0.23 nm). The Al feed lines origin from the Al/Ge exchange show an overall low RMS roughness of 0.25 nm in the region excluding the grain boundaries (dashed box in **Figure 4.3b**), much smoother than sputtered Al. Grain boundaries may be expected as the exchange of wider Ge sheets (>300 nm) results in polycrystalline Al feed lines[76].

Die approbierte gedruckte Originalversion dieser Dissertation ist an der TU Wien Bibliothek verfügbar.
The approved original version of this doctoral thesis is available in print at TU Wien Bibliothek.
TU WIEN Bibliothek Your knowledge hub

4.1.2 Basic electrical properties of Al-Ge-Al heterostructures

4.1.2.1 Current/voltage characteristics

As already mentioned in the experimental section, the Al-Ge-Al heterostructure fabricated on a GeOI substrate resembles a SBFET with two Al pads, the Ge channel, the buried SiO_2, and highly doped handle wafer as the drain/source electrodes, the semiconductor channel, gate dielectric, and the back gate, respectively. **Figure 4.4a** depicts the I/V curves of an Al-Ge-Al SBFET with a channel length of L = 0.6 μm measured at various back-gate voltages.

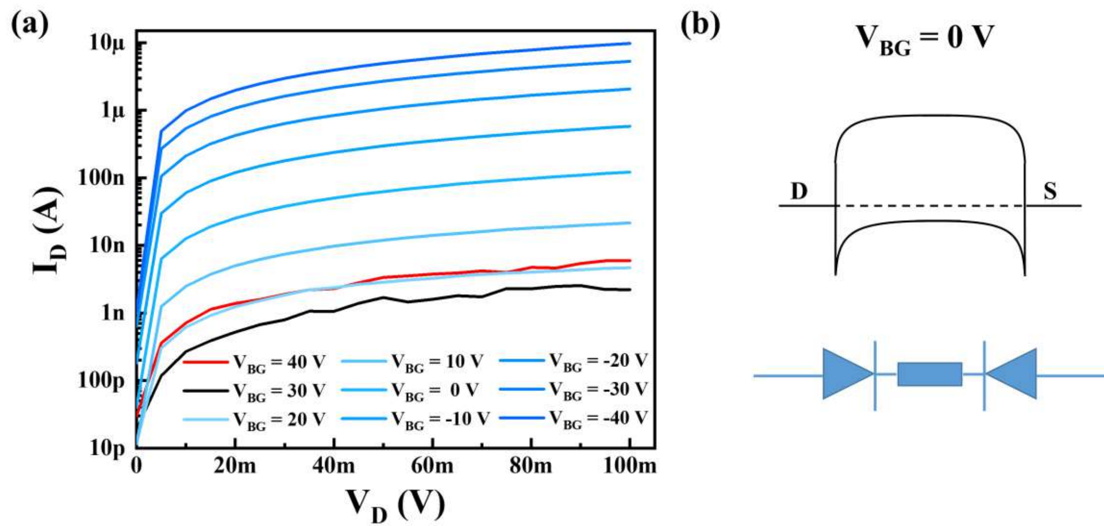

Figure 4.4 (a) I/V curves of an Al-Ge-Al SBFET with a channel length of L_{Ge} = 0.6 μm measured at various back-gate voltages. (b) Band diagram of the Al-Ge-Al heterostructure device at the back-gate voltage of V_{BG} = 0 V. The lower panel shows the equivalent circuit of a back-to-back Schottky type device.

An Al-Ge-Al heterostructure can be considered as two back-to-back Schottky diodes in series with the Ge channel, in which the applied bias loads on the Schottky junction at two Al/Ge interfaces and the Ge channel (please see **Figure 4.4b**). Under positive drain voltage V_D, one Schottky diode is forward-biased whereas the other one is reverse-biased, limiting the current to pass. Generally, the back-gate electrode modulates the effective barrier height, thereby altering the drain current I_D. While the back-gate voltage V_{BG} increases from -40 V (the deep blue curve in **Figure 4.4**) to 30 V (the black curve in **Figure 4.4**), the drain current I_D decreases, resulting in an on/off ratio of 4.4×10^3 at V_D = 100 mV. Further increase of V_{BG} to +40 V induces to further increase of the drain current. Furthermore, to clarify the contribution of the Ge channel and the reverse-biased Schottky junction to the total current, the I/V characteristics of Al-Ge-Al SBFETs with different channel lengths are measured (see **Figure 4.5a)**.

Die approbierte gedruckte Originalversion dieser Dissertation ist an der TU Wien Bibliothek verfügbar.
The approved original version of this doctoral thesis is available in print at TU Wien Bibliothek.
TU Wien Bibliothek Your knowledge hub

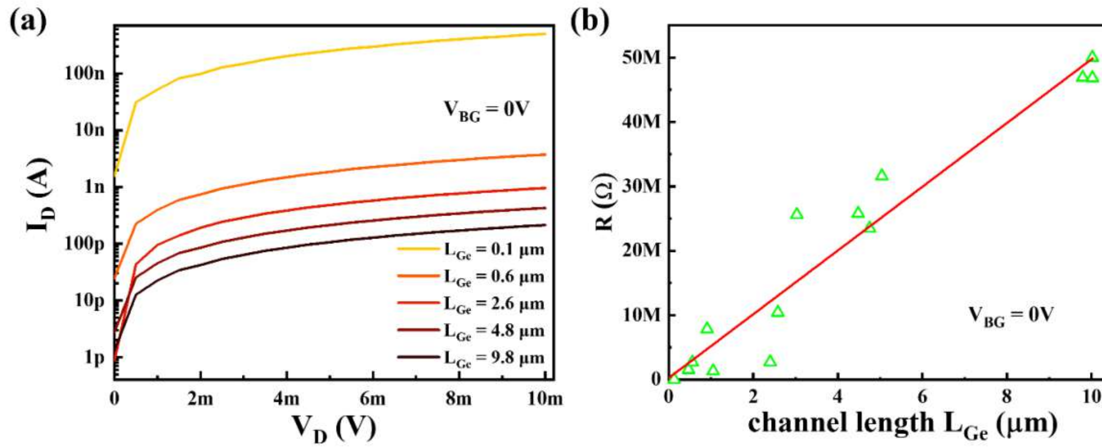

Figure 4.5 (a) I/V characteristics of Al-Ge-Al heterostructure devices with different channel lengths L_{Ge} measured at back-gate voltage of V_{BG} = 0V. (b) Resistance R of the Al-Ge-Al heterostructure as the function of channel length L_{Ge} at the back-gate voltage of V_{BG} = 0V.

The whole Al-Ge-Al heterostructure device is assumed as a regular resistor, following Ohm's law

$$R = \frac{V_D}{I_D} = \rho \frac{L_{Ge}}{S_{cs}} \tag{4.1}$$

where R is the electrical resistance, L_{Ge} is the Ge channel length, S_{cs} is the cross-sectional area of the Ge channel (i.e. $S_{cs} = 1.5 \times 10^{-8}$ cm^2 in **Figure 4.4**) and ρ is the resistivity. From the slope of the I/V curves in **Figure 4.5a** one can calculate the resistance and thereof according to **Eq. 4.1** the resistivity ρ = 677 Ω·cm. **Figure 4.5b** shows the resistance R as a function of the Ge channel length L_{Ge}. Extrapolating the points to the channel length of L_{Ge} = 0, the contact resistance is calculated as 0.25 MΩ, corresponding to the reverse-biased Schottky junction. Taking the device with the channel length of L_{Ge} = 1.0 μm for an example, the resistance of the Ge channel is calculated as 5.2 MΩ. Thus, even a higher bias is loaded on the Ge channel, compared to the reverse-biased Schottky junction, which will be discussed in **Section 4.1.2.3**.

Die approbierte gedruckte Originalversion dieser Dissertation ist an der TU Wien Bibliothek verfügbar.
The approved original version of this doctoral thesis is available in print at TU Wien Bibliothek.
TU WIEN Bibliothek Your knowledge hub

4.1.2.2 Transfer characteristics of Al-Ge-Al heterostructure devices

The transfer curve is a typical measurement for characterizing a SBFET, in which the drain current I_D is plotted as the function of the back-gate voltage V_{BG}. **Figure 4.6** illustrates transfer (I_D-V_{BG}) characteristics of an Al-Ge-Al SBFET with a channel length of L = 600 nm.

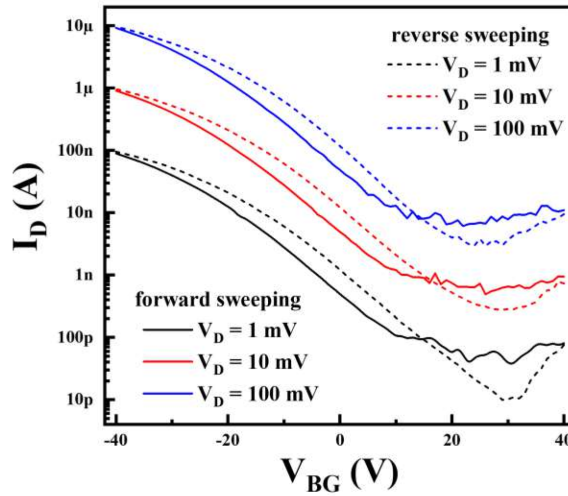

Figure 4.6 Transfer characteristics of an Al-Ge-Al SBFET with a channel length of L_{Ge} = 0.6 μm measured at different drain bias V_D. Solid lines and dashed lines represent forward and reverse sweeping, respectively.

For a drain voltage of V_D = 1 mV, the Al-Ge-Al SBFET with a channel length of L_{Ge} = 0.6 μm exhibits a significant on/off ratio of ~ 1.9×10^3 (for forward sweeping). The SBFET apparently works like a p-channel transistor, as a sharp rise of drain current I_D shows up at negative back-gate voltages. Such p-type characteristic is not a consequence of unintentional Al doping in the Ge channel during the annealing but is a common phenomenon for unpassivated Ge transistors due to effective surface doping[77]. For the same reason, inevitable hysteresis phenomena appear when sweeping the gate voltage from V_{BG} = -40 V to +40 V and then back down to -40 V again. The applied drain voltage V_D modulates the transfer characteristics of the SBFET, that is, the shape maintains the same but the magnitude is linearly proportional to the applied drain bias V_D.

Die approbierte gedruckte Originalversion dieser Dissertation ist an der TU Wien Bibliothek verfügbar.
The approved original version of this doctoral thesis is available in print at TU Wien Bibliothek.
TU WIEN Bibliothek Your knowledge hub

4.1.2.3 Effective barrier height of Al-Ge junction

In this chapter, the back-gate voltage-dependent effective Schottky barrier height Φ_{EB} of a monolithic Al-Ge junction will be discussed. **Figure 4.7** shows the temperature-dependent transfer characteristics of the Al-Ge-Al SBFET.

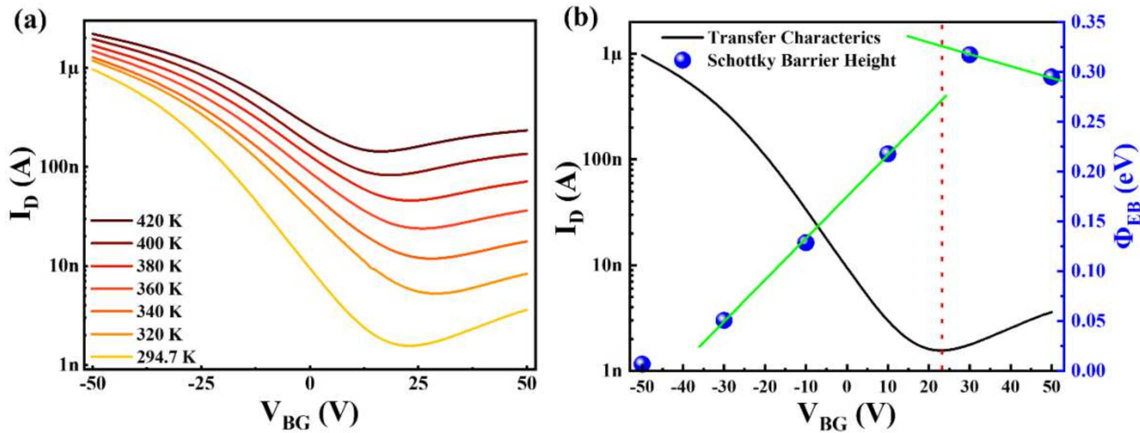

Figure 4.7 Gate controlled effective barrier height Φ_{EB} for an Al-Ge-Al heterostructure SBFET with a channel length of L_{Ge} = 0.6 µm. The drain voltage is V_D = 10 mV. (a) Temperature-dependent transfer curves. (b) drain current I_D and effective Schottky barrier height Φ_{ESB} as the function of applied back-gate voltage V_{BG}.

At all back-gate voltages V_{BG}, the drain current I_D increases with temperature. The method based on the Richardson plots (please see **Chapter 3.2.3**) is employed to determine Φ_{EB} as a function of back-gate voltage, and the corresponding results are illustrated in **Figure 4.7b**. Sweeping the back-gate voltage from from -50 V to +50 V, the effective barrier height Φ_{EB} will increases to the maximum at V_{BG} = 23 V and then decreases, which is reversed to the tendency of the transfer curve. **Figure 4.8** demonstrates the corresponding band diagram of the Al-Ge-Al heterostructure SBFET under characteristic back-gate voltages.

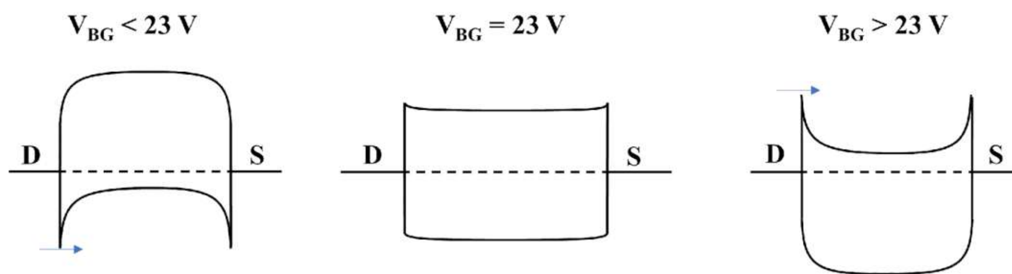

Figure 4.8 Band diagram showing gate-controlled effective barrier height Φ_{EB} modulation for Al-Ge-Al heterostructure SBFETs.

Die approbierte gedruckte Originalversion dieser Dissertation ist an der TU Wien Bibliothek verfügbar.
The approved original version of this doctoral thesis is available in print at TU Wien Bibliothek.
TU WIEN Bibliothek Your knowledge hub

In the region of V_{BG} < 23 V, the Ge segment performs like a p-type FET, as the Fermi level E_F aligns close to the valance band making the band bend upward, thus resulting in a lower effective Schottky barrier height Φ_{ESB} for holes. While the applied back-gate voltage reduces to -40 V, the Fermi level E_F shifts toward the valence band, leading to the shaper curvature of the band bending near the Al/Ge interface. The shaper bending reduces the width of the depletion region, resulting in a lower effective barrier height and a higher drain current. In contrast, at the back-gate voltage of V_{BG} > 23 V the n-type characteristic shows up. The Fermi level E_F shifts close to the conduction band reducing effective barrier height for electrons, thereby enabling the higher drain current. At the back-gate voltage of V_{BG} = 23 V, the Fermi level E_F locates mid-gap of the Ge bandgap, causing a maximum barrier height for electrons/holes, thereby the minimum drain current I_D appears.

Die approbierte gedruckte Originalversion dieser Dissertation ist an der TU Wien Bibliothek verfügbar.
The approved original version of this doctoral thesis is available in print at TU Wien Bibliothek.
TU WIEN Bibliothek Your knowledge hub

4.1.3 Plasmonic applications of Al-Ge-Al heterostructure devices

4.1.3.1 Photodetector with tunable positive or negative photoconductivity

4.1.3.1.1 The impact of gate voltage

Under irradiation, the generation of additional charge carriers alters the carrier concentration or the mobility of a semiconductor, thereby changing the total conductivity. Most commonly, a positive-photoconductivity (PPC) effect is observed, due to an enhanced carrier concentration. However, also negative-photoconductivity (NPC) effect may be induced due to the photo-gating effect. This section will demonstrate that photoconductivity of the compact Al-Ge-Al heterostructure device can be tuned from positive to negative. **Figure 4.9a** shows the schematic of the measurement setup in which the green laser beam is focused directly on the Ge segment. **Figure 4.9b** demonstrates a typical SEM image of an Al-Ge-Al heterostructure with a channel length of 200 nm.

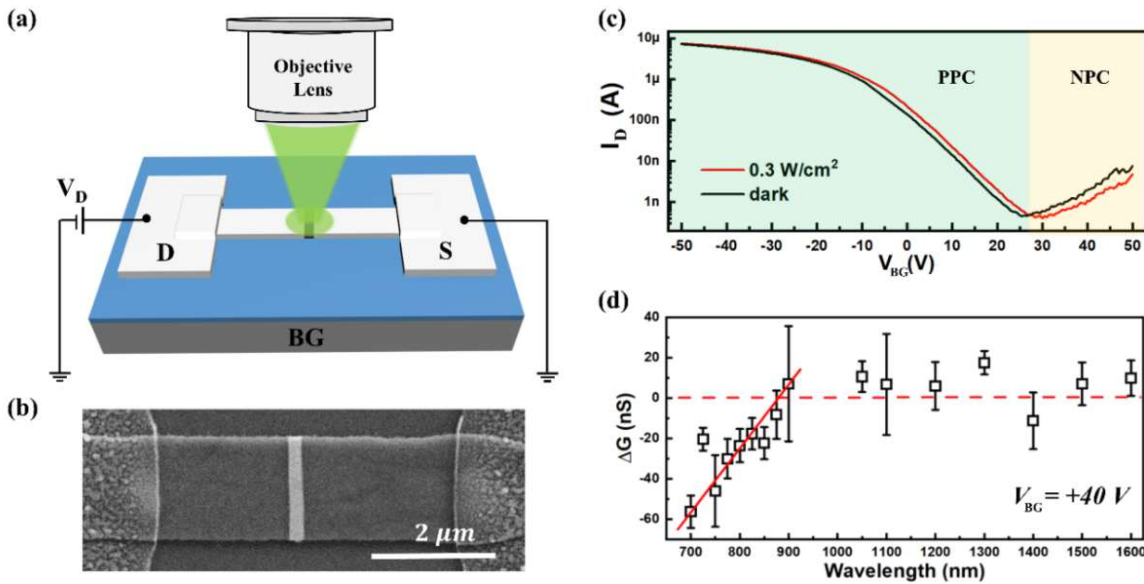

Figure 4.9 (a) The measurement setup of the Al-Ge-Al heterostructure SBFET under laser irradiation. (b) The SEM image of an ultra-short Al-Ge-Al heterostructure with channel length of L_{Ge} = 200 nm. (c) The comparison of transfer characteristics of the Al-Ge-Al heterostructure transistor with a channel length of L_{Ge} = 200 nm measured in the dark and under laser irradiation. The drain bias V_D and light density are set as 10 mV and 0.3 W/cm^2, respectively. (d) Wavelength-dependent photoconductance ΔG ($\Delta G = G_{ph} - G_d$, where G_{ph} is the conductance of Ge channel under light, G_d is the conductance measured in the dark) at a back gate voltage of V_{BG} = +40 V.

Die approbierte gedruckte Originalversion dieser Dissertation ist an der TU Wien Bibliothek verfügbar.
The approved original version of this doctoral thesis is available in print at TU Wien Bibliothek.
TU WIEN Bibliothek Your knowledge hub

Figure 4.9c shows the respective transfer curves measured in the dark and under laser illumination of the Al-Ge-Al heterostructure device with the ultra-short Ge channel length of L_{Ge} = 200 nm. In the dark, the drain current I_D increases for negative gate voltages, indicating a p-channel enhancement mode transistor functionality. The p-type performance, despite the Ge segment is intrinsic, originates from surface doping[77]. As the Ge layer is rather thin (t = 75 nm), surface traps play an important role determining the electric properties of the Al-Ge-Al heterostructure device. Fast traps at the GeO_x/Ge interface and slow traps inside the GeO_x may capture electrons[78]. The filling of the traps is thereby determined by the position of the Fermi level and thus the back gate voltage. **Figure 4.9c** shows that the position of the Fermi level E_F can be effectively adjusted by the back-gate voltage. Increasing the back-gate voltage the Fermi level E_F moves from the valance band towards the conduction band and thus firstly reduces the accumulation of holes resulting in an initial decrease of the drain current. At the back-gate voltage of approximately 27 V, the Ge channel is depleted, corresponding to the minimum point of the transfer curve. Further increase of the back gate voltage results in a slight increase of the drain voltage now driven by the electrons. However, changing the back gate voltage also influences the population of traps. To prove that traps can alter the electrical properties, different sweeping rates have been applied for two double-sweeping transfer tests (see **Figure 4.10a**). It can be seen that the higher sweeping rate results in weaker hysteresis, although the hysteresis is inevitable.

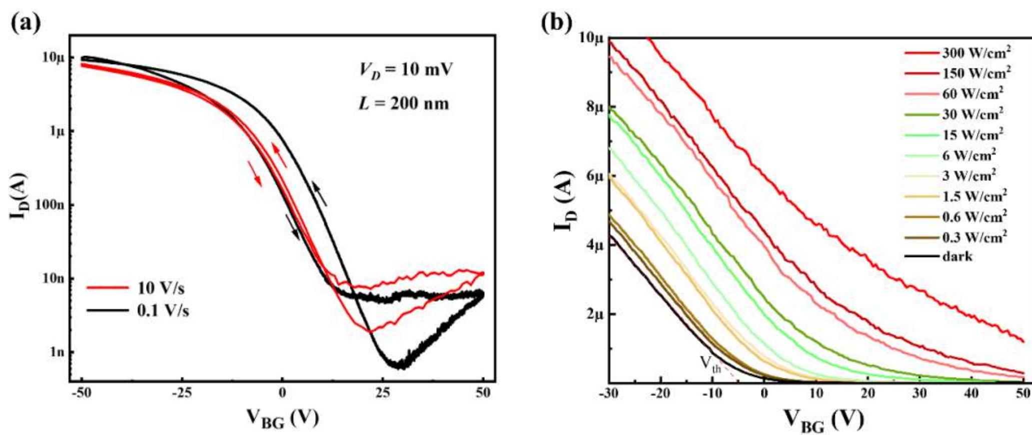

Figure 4.10 (a) Transfer characteristics of Ge SBFET with a channel length of L_{Ge} = 200 nm under different sweeping directions and sweeping rates. The drain voltage V_D is 10 mV. (b) Light intensity modulated transfer characteristics of the Al-Ge-Al heterostructure transistor with a channel length of L_{Ge} = 200 nm at a drain voltage of V_D = 10 mV.

Die approbierte gedruckte Originalversion dieser Dissertation ist an der TU Wien Bibliothek verfügbar.
The approved original version of this doctoral thesis is available in print at TU Wien Bibliothek.
TU WIEN Bibliothek Your knowledge hub

At the back-gate voltage of V_{BG} = -50 V (see **Figure 4.9c**), a huge PPC leads to a large responsivity of 424 A/W, corresponding to a gain factor of 1.4×10^3. As the applied wavelength is λ = 532 nm, the corresponding photon energy (2.33 eV) is much larger than the Ge bandgap (0.67 eV). Therefore, highly energetic photogenerated electrons may occupy traps near the GeO_x/Ge interface and also inside the native oxide GeO_x. As the thickness of Ge device layer is only 75 nm, such negatively charged traps can work as an effective local gate, affecting the threshold voltage and thus the photocurrent. The photocurrent is thus given by[79]

$$I_{ph} \approx g_m \cdot \Delta V_{th} \tag{4.2}$$

with the transconductance $g_m = dI_D/dV_{BG}$ and ΔV_{th} the shift of the threshold voltage.
As shown in **Figure 4.9c** under particular biasing conditions and laser power, the polarity of the photocurrent becomes negative at the back-gate voltage $V_{BG} \geq 27$ V (see the yellow marked region of **Figure 4.9c**). This is the regime where the device performs like an n-type FET and the decrease of the photocurrent is referred to as NPC. Fundamentally, the NPC behavior of n-type semiconductors may be attributed to two factors: (1) reduced mobility due to severe carrier scattering under irradiation[80] and (2) lower carrier concentration owing to the light induced depletion for the semiconductor channel[81–83]. With increasing light power, the transfer curves maintain the overall shape but are shifting toward higher gate voltages (see **Figure 4.10b**), which is the typical behavior induced by the photogating[32]. The constant slope in the linear region of the transfer curves under various light power excludes that laser illumination have a significant impact on the mobility of the charge carriers.
The traps filled by photogenerated electrons will be negatively charged, and further work as a negative local gate that counteracts the applied positive back gate, resulting in a smaller effective gate voltage V_{BG}^{eff}, which can be expressed as[82]

$$V_{BG}^{eff} = V_{BG} - \frac{|Q_{trap}|}{C} \tag{4.3}$$

with C the capacitance of the surface oxide and Q_{trap} the charge of the filled traps. These effective negative local gate induces a shift of the transfer curve toward higher positive gate voltages, without significantly influencing the mobility in the channel. This shift of the transfer curve to higher gate voltages leads, as can be seen in **Figure 4.10b**, to NPC in the electron dominated transport regime.
In order to investigate how filling of traps depends on the energy of photogenerated electrons, the Al-Ge-Al heterostructure SBFET was measured at different wavelength of the irradiating laser. **Figure 4.9d** shows the photoconductivity as a function of the wavelength of the incident

Die approbierte gedruckte Originalversion dieser Dissertation ist an der TU Wien Bibliothek verfügbar.
The approved original version of this doctoral thesis is available in print at TU Wien Bibliothek.
TU Bibliothek WIEN Your knowledge hub

light measured at a back-gate voltage of V_{BG} = 40 V. In particular, the ΔG is defined as

$$\Delta G = G_{ph} - G_d \quad (4.4)$$

with G_{ph} the conductance under irradiation and G_d the conductance in dark. The magnitude of the photoconductance, starting at a wavelength of 700 nm, exhibits a continuous decrease as the wavelength increases. This trend continues until it reaches a point around a wavelength of 900 nm, corresponding to an energy of 1.34 eV. Thus, NPC behavior only occurs at the photon energy of >1.34 eV. In other words, it suggests filling the traps requires the photogenerated electrons to overcome an equivalent activation barrier.

Figure 4.11 shows schematically the impact of traps on the polarity of the photoconductance. In the p-type region, in dark the Fermi level situates near the valance band, thereby resulting in the filling of these traps situated below the Fermi level.

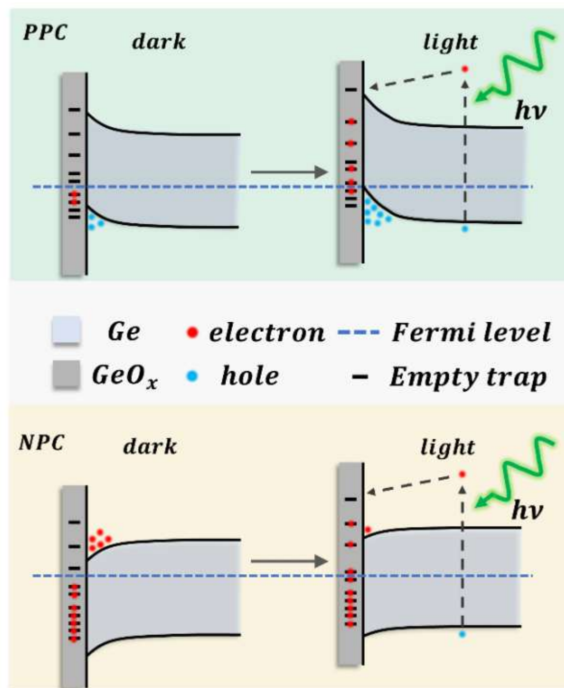

Figure 4.11 Band diagrams applied to schematically explain PPC and NPC phenomena. The upper and lower panels illustrate the positive and negative photoconductance, respectively. Inside each panel, the left and right diagram demonstrate the situation in dark and under irradiation, respectively.

Filled traps, serving as supplementary negative local gate, induces an upward bending of the conduction and valance bands of Ge. Thus, fostering the accumulation of holes resulting in the typical p-type like behaviour is commonly attained in unpassivated Ge channels. Under

Die approbierte gedruckte Originalversion dieser Dissertation ist an der TU Wien Bibliothek verfügbar.
The approved original version of this doctoral thesis is available in print at TU Wien Bibliothek.
TU WIEN Bibliothek Your knowledge hub

irradiation, the photo-generated hot electrons occupy traps above the Fermi level, hence strengthening the negative local gate as well as the bending of the bands. As a result, the accumulation of holes is enhanced, leading to increased conductivity and the observed PPC.

In contrast, in the n-type region (lower panel in **Figure 4.11**) i.e. at high positive gate voltages, in the dark the Fermi level is shifted towards the conduction band, giving rise to the downward bending of the Ge bands and the accumulation of electrons. Upon exposure to laser irradiation, again traps located above the Fermi level are filled by high energetic photo-generated electrons. Such filled traps act like a negative local gate, which counteracts the positive back gate. Therefore, electrons will be repelled and the channel conductivity decreases, which consequently manifests itself in the observed NPC.

4.1.3.1.2 The impact of light intensity

Aside from the control of the back-gate voltage, the power of the incident light can efficiently adjust the polarity of photoconductance *ΔG* as well. **Figure 4.12a** shows the photoconductance as a function of different light intensities.

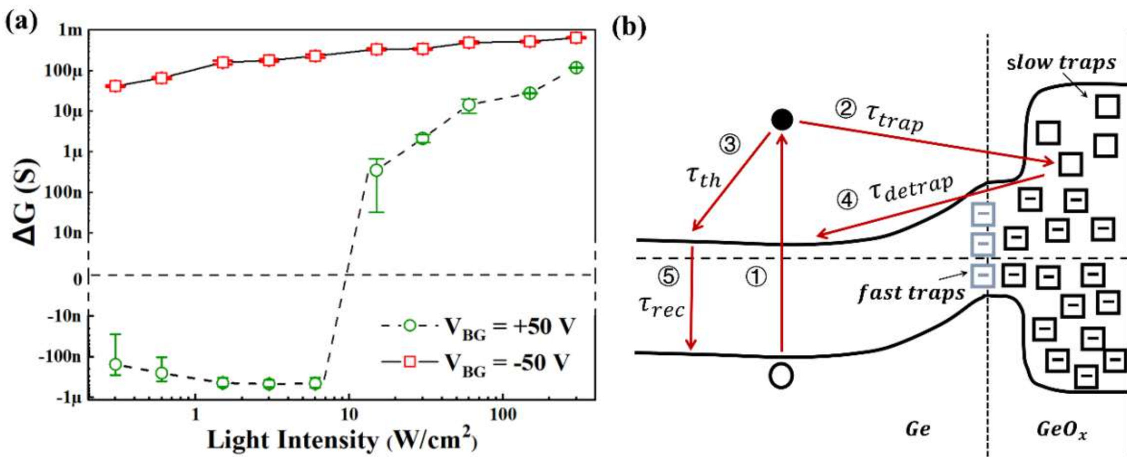

Figure 4.12 (a) Light intensity dependent photoconductance ΔG for two characteristic back-gate voltages of -50 V and +50 V. The channel length of Ge SBFET is L_{Ge} = 200 nm and the drain voltage is V_D = 10 mV. (b) The working mechanism related to the hot-carrier trapping model.

At a gate voltage of V_{BG} = -50 V, PPC is observed in the entire range of light intensity. However, at the gate voltage of V_{BG} = +50 V, NPC was observed at low light intensities of ≤ 6 W/cm^2, whereas ΔG turns to be positive at higher light intensities of > 6 W/cm^2. The hot-carrier trapping model, proposed by *Y. Yang et al*[81], can account for this observed polarity change

Die approbierte gedruckte Originalversion dieser Dissertation ist an der TU Wien Bibliothek verfügbar.
The approved original version of this doctoral thesis is available in print at TU Wien Bibliothek.
TU Bibliothek WIEN Your knowledge hub

of photoconductance ΔG as a function of light intensities.

The band diagram of the Ge and GeO_x, as depicted in **Figure 4.12b**, provides insight into the underlying mechanism of the switch from NPC to PPC. Under irradiation with a photon energy larger than the bandgap energy of Ge, light absorption generates hot charge carriers with a rate of g. This results in a particular density of hot electrons n_{hot} and hot holes p_{hot} (step ①). The hot electrons may release their energy arriving at the conduction band edge via thermalization (step ③) with a time constant of τ_{th}; or may be captured by empty traps inside GeO_x (step ②) with the time constant of τ_{trap}. Afterwards the filled traps may release the electrons to the conduction band edge (step ④) with the time constant of τ_{detrap}. Finally, both the thermalized electrons at the conduction band edge and detrapped electrons may recombine with hot holes in the valance band by the band-to-band recombination with the time constant τ_{rec} (step ⑤).

From a mathematical perspective, the hot-carrier trapping model gives

$$\frac{dn_{hot}}{dt} = g - \frac{n_{hot}}{\tau_{th}} - \frac{n_{hot}}{\tau_{trap}}\left(1 - \frac{n_{trap}}{N_{trap}}\right) \tag{4.5}$$

$$\frac{dn_{trap}}{dt} = \frac{n_{hot}}{\tau_{trap}}\left(1 - \frac{n_{trap}}{N_{trap}}\right) - \frac{n_{trap}}{\tau_{detrap}} \tag{4.6}$$

$$\frac{d\Delta n}{dt} = \frac{n_{hot}}{\tau_{th}} - \frac{\Delta p}{\tau_{rec}} + \frac{n_{trap}}{\tau_{detrap}} \tag{4.7}$$

$$\frac{dp_{hot}}{dt} = g - \frac{p_{hot}}{\tau_{th}} \tag{4.8}$$

$$\frac{d\Delta p}{dt} = \frac{p_{hot}}{\tau_{th}} - \frac{\Delta p}{\tau_{rec}} \tag{4.9}$$

with the respective parameters listed in **Table 4.1**.

Die approbierte gedruckte Originalversion dieser Dissertation ist an der TU Wien Bibliothek verfügbar.
The approved original version of this doctoral thesis is available in print at TU Wien Bibliothek.
TU WIEN Bibliothek Your knowledge hub

Table 4.1 Parameters utilized in the hot-carrier trapping model

parameter	lifetime
n_{trap}	density of trapped electrons
n_{hot}	density of hot electrons
p_{hot}	density of hot holes
Δn	density of electrons at the band edge
Δp	density of holes at the band edge
g	generation rate of hot electrons
N_{trap}	overall number of trap states
τ_{th}	thermalization time of hot electrons
τ_{rec}	hot electron lifetime due to band-to-band recombination
τ_{trap}	trapping time of hot electrons
τ_{detrap}	detrapping time of hot electrons

Regarding the dynamics of the photoconductivity two extreme scenarios may be distinguished:

Case I: At ultralow light intensities, only a few traps are filled ($n_{trap} \ll N_{trap}$). The photoconductivity ΔG is then given by

$$\Delta\sigma = (\Delta n + n_{hot})q\mu_n = qg\mu_n\left(\tau_{rec} - \frac{\tau_{th}\tau_{detrap}}{\tau_{trap}}\right) \tag{4.10}$$

For the trapping of electrons at the Ge-GeO$_x$ interface a trapping time τ_{trap} is reported on the scale of 100 ns to 10 ns[84], whereas the detrapping time τ_{detrap} can last for several minutes[28]. Additionally, the thermalization time of hot carriers is in the order of picoseconds[85]. Therefore, based on **equation 4.14** and the parameters listed in **Table 4.2**, $\frac{\tau_{th}\tau_{detrap}}{\tau_{trap}}$ should exceed 1 ms.

Table 4.2 Parameters applied to calculate NPC

parameter	lifetime
τ_{th}	*1 ps*
τ_{rec}	*1 ms*
τ_{trap}	*10 ns*
τ_{detrap}	*60 s*

Die approbierte gedruckte Originalversion dieser Dissertation ist an der TU Wien Bibliothek verfügbar.
The approved original version of this doctoral thesis is available in print at TU Wien Bibliothek.
TU Bibliothek WIEN Your knowledge hub

For Ge the lifetime of hot electrons before recombination τ_{rec} should be no longer than 1 ms[36]. Thus $\frac{\tau_{th}\tau_{detrap}}{\tau_{trap}}$ is larger than the lifetime of hot electrons in Ge and thus NPC appears under low light power.

Case II: Under high light intensity, almost all trap states may be occupied ($n_{trap} \approx N_{trap}$) and $\Delta\sigma$ is given by

$$\Delta\sigma \approx q\mu_n\left(G\tau_{rec} - N_{trap}\right) \tag{4.11}$$

Without proper passivation, the density of trap states D_{trap} at the Ge-GeO$_x$ interface exceeds 10^{15} cm^{-2}[22]. The channel surface area of the actual Al-Ge-Al photodetector is about S = 6.8×10^{-9} cm^2. According to $N_{trap} = D_{trap} \cdot S$ the total number of traps N_{trap} is thus about 10^6.

Furthermore, the photoexcitation rate g is related to the number of photons absorbed in the Ge segment which is given by

$$\frac{dN}{dt} = \frac{P\mathcal{O}A}{h\nu} \tag{4.12}$$

with P the light power, $\mathcal{O}$ the overlap area of the Ge channel and laser spot, $h\nu$ the photon energy and A the absorbance. Assuming a Gaussian laser beam shape and perfect center-to-center alignment, numerically integrating the center of the two-dimensional distribution function over the rectangular area of the Ge segment yields the overlap area

$$\mathcal{O} = \int_{-\frac{L}{2}}^{\frac{L}{2}} \int_{-\frac{W}{2}}^{\frac{W}{2}} \frac{1}{2\pi\zeta^2} exp\, exp\left(-\frac{x^2+y^2}{2\zeta^2}\right) dxdy = erf\left(\frac{W}{2\sqrt{2}\cdot\zeta}\right) \cdot erf\left(\frac{L}{2\sqrt{2}\cdot\zeta}\right) \tag{4.13}$$

with L the channel length, W the channel width and $erf(x)$ the error function. ζ denotes the variance of the Gaussian function for the objective lens

$$\zeta = 0.22\lambda/NA \tag{4.14}$$

with λ the wavelength of the incident light and NA the numerical aperture of the objective.

A Zeiss 4X objective with the numerical aperture of NA = 0.1 is applied, resulting in a variance ζ of 1.17 µm. Using the parameters listed in **Table 4.3** results in an overlap of $\mathcal{O}$ = 0.043.

Die approbierte gedruckte Originalversion dieser Dissertation ist an der TU Wien Bibliothek verfügbar.
The approved original version of this doctoral thesis is available in print at TU Wien Bibliothek.
TU Bibliothek WIEN Your knowledge hub

Table 4.3 Parameters used in the calculation

Parameter	Value
W	$2 \times 10^{-6}\ m$
L	$2 \times 10^{-9}\ m$
NA	0.1
ζ	$1.17 \times 10^{-6}\ m$
$erf\left(W/(2\sqrt{2}\cdot\zeta)\right)$	0.61
$erf\left(L/(2\sqrt{2}\cdot\zeta)\right)$	0.07
$\mathcal{O}$	0.043

According to the Beer-Lambert law, the attenuation of light passing through a sample is given by

$$I(x) = I_0 e^{-\alpha x} \tag{4.15}$$

where I_0 is the initial light intensity at the surface ($x = 0$), $I(x)$ the light intensity at the depth of x and α the absorption coefficient. Referring to the absorption coefficient table of Ge[86], the absorption coefficient is $\alpha = 5.57 \times 10^5\ cm^{-1}$ at the wavelength of λ = 532 nm. In this case, cross sections of the Ge segment are homogeneous for all depths, the transmittance T is given by

$$T = \int_0^d \frac{1}{d} exp\ (-\alpha x)\ dx \tag{4.16}$$

Neglecting reflection, the absorbance A becomes

$$A = 1 - T \tag{4.17}$$

For the 75 nm thick Ge channel, A can be calculated as 66.5%. Furthermore, the number of photons absorbed per second under different light intensities is calculated and depicted in **Table 4.4**.

Die approbierte gedruckte Originalversion dieser Dissertation ist an der TU Wien Bibliothek verfügbar.
The approved original version of this doctoral thesis is available in print at TU Wien Bibliothek.
TU Bibliothek WIEN Your knowledge hub

Table 4.4 Absorbed photons per second under a certain power density

Light intensity (W/cm²)	The number of photons absorbed per second
0.3	6.86×10^{9}
3	6.86×10^{10}
30	6.86×10^{11}
300	6.86×10^{12}
3000	6.86×10^{13}

For a light intensity of 30 W/cm², the corresponding generation rate g can exceed 10^{11}, even when using a small internal quantum efficiency of IQE = 50% for converting photons to electrons. The recombination lifetime τ_{rec} of carriers inside the semiconductors depends also on the doping concentration. It has been experimentally proven that the recombination lifetime τ_{rec} is at the level of 0.1 ms for an n-type Ge with a doping density of 10^{13} cm^{-3}. Consequently, $g\tau_{rec}$ (~10^{7}) exceeds N_{trap} (~10^{6}) resulting in PPC. In conclusion, the carrier-trapping model provides an explanation for the transition from NPC to PPC at high light intensity. To confirm the generality of the polarity change, light intensity dependent photoconductivity is measured for Al-Ge-Al SBFETs with different channel lengths (see **Figure 4.13**).

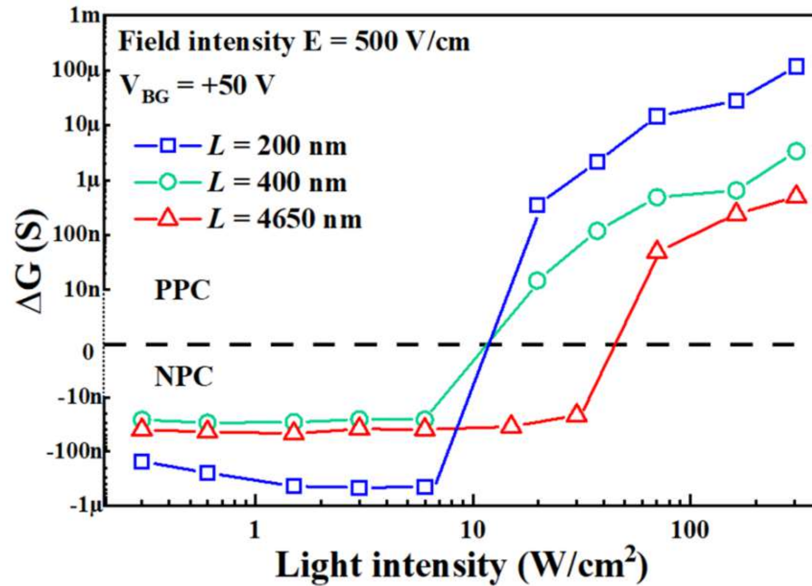

Figure 4.13 The impact of channel length on the polarity of the photoconductance ΔG at a gate voltage of V_{BG} = 50 V. Electrical field strength is 500 V/cm.

TU Bibliothek Your knowledge hub WIEN
Die approbierte gedruckte Originalversion dieser Dissertation ist an der TU Wien Bibliothek verfügbar.
The approved original version of this doctoral thesis is available in print at TU Wien Bibliothek.

For different channel lengths, the gate voltage is fixed at V_{BG} = +50 V, and the drain voltage V_D is adapted to the channel length to achieve the same field strength of 500 V/cm in all three devices. All three devices exhibit a transition from NPC to PPC at high light intensities. In an Al-Ge-Al SBFET with a shorter channel length, photo-generated charge carriers will experience less scattering while moving from one side of the Ge channel to another, resulting in a higher photocurrent.

Die approbierte gedruckte Originalversion dieser Dissertation ist an der TU Wien Bibliothek verfügbar.
The approved original version of this doctoral thesis is available in print at TU Wien Bibliothek.
TU Bibliothek Your knowledge hub WIEN

4.1.3.2 Plasmon-assisted polarization-sensitive photodetector

Prior to surveying plasmon-assisted on-chip photodetectors, here a polarization sensitive photodetector is presented. Several reports have confirmed that metallic gratings with periods less than the light wavelength can generate SPPs from TM-polarized light, thus enabling polarization-dependent functionality[87–91]. Furthermore, some related works found ultra-scaled Ge photodetectors performing polarization-dependent response, as the nanoscale monolithic electrodes can serve as a plasmon antenna[92–94]. In these cases, two metallic nanoribbons separated by an ultra-short Ge segment may work like plasmonic dimers (see **Figure 4.14a**), allowing us to investigate localized surface plasmons below diffraction limit.

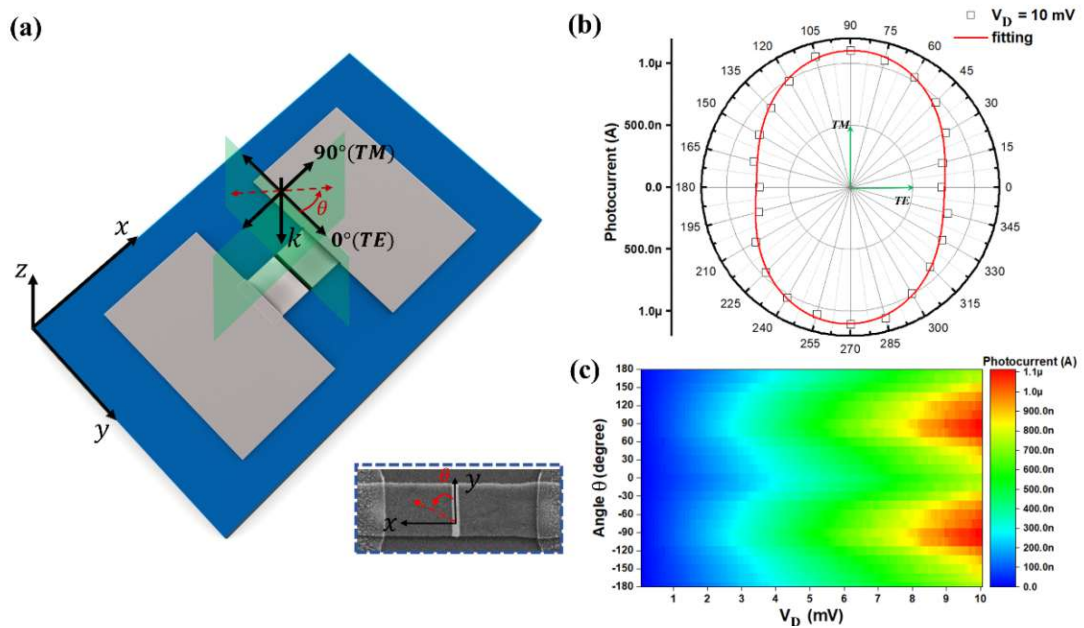

Figure 4.14 (a) Schematic of the setup for polarization-dependent measurement. The inset depicts the SEM image of the Al-Ge-Al heterostructure with the polarization angle θ. The polarization angle 0° and 90° correspond to the electric component of the polarized light parallel and perpendicular to the Ge channel, referred to as TE and TM, respectively. (b) Polar plot of the photocurrent as a function of the polarization angle θ. (c) Photocurrent map as a function of the drain voltage V_D and polarization angle θ. The measurements related to panel **b** and **c** were conducted at a gate voltage V_{BG} = 0 V, V_D = 10 mV and a light intensity of 30 W/cm^2, respectively.

As shown in **Figure 4.14a**, a linearly polarized laser with the wavelength of λ = 532 nm is directly focused on the ultra-small Ge segment with a channel length of 200 nm and a width of 2 µm. **Figure 4.14b** shows the respective polarization-dependent photocurrent measured at a

Die approbierte gedruckte Originalversion dieser Dissertation ist an der TU Wien Bibliothek verfügbar.
The approved original version of this doctoral thesis is available in print at TU Wien Bibliothek.
TU Bibliothek WIEN Your knowledge hub

drain voltage of V_D = 10 mV. The polarization angle φ denotes the angle between the Al/Ge interface and the electric field component of the light. The maximum photocurrent is observed at a polarization angle of θ = 90º and θ = 270º, corresponding to the polarization direction where the electric field of the incident light is polarized normal to the Al/Ge interface. Furthermore, **Figure 4.14b** indicates measured data follows the sinusoidal function and the polarization rate can be derived as ~1.5 times at drain voltage of V_D = 10 mV. The inset of **Figure 4.14a** shows the SEM image of the ultra-scaled Ge photodetector. Such an ultra-short Ge segment can be viewed as a semiconductor nanowire with a length of 2 µm, a thickness of only 75 nm and a width of 200 nm. Normally, owing to the dielectric mismatch effect[95], semiconductor nanowires should induct the maximum photocurrent if the polarization of the electric field of the incident light is oriented parallel to their nanowire, which is the TE direction in **Figure 4.14a**. As the real part of permittivity for metals is negative, the plasmon maximum for metallic nanowires is formed in the direction where the polarization of the electric field of the incident light is oriented normal to the nanowire[95]. However, for the actual device layout this dielectric mismatch effect is overcompensated by the plasmon antenna effect. Furthermore, **Figure 4.14c** shows that the maximum photocurrent always appears for the TM direction for all the drain voltages. It suggests drain voltage V_D only alters the magnitude of the plasmon current and has no impact on the plasmon antenna effect.

Die approbierte gedruckte Originalversion dieser Dissertation ist an der TU Wien Bibliothek verfügbar.
The approved original version of this doctoral thesis is available in print at TU Wien Bibliothek.
TU WIEN Bibliothek Your knowledge hub

4.1.3.3 Plasmon-induced hot-carrier detector

In this chapter a plasmon-induced hot-carrier detector is discussed based on the Al-Ge-Al heterostructure device (see **Figure 4.15**). The overall working principle is as follows: When the TM polarized light impinges the optical diffraction grating (i.e. the oval trenches in the Al feed line), additional momentum k would be provided by the grating supporting the momentum conservation and thus generating surface plasmons in the Al feed line.

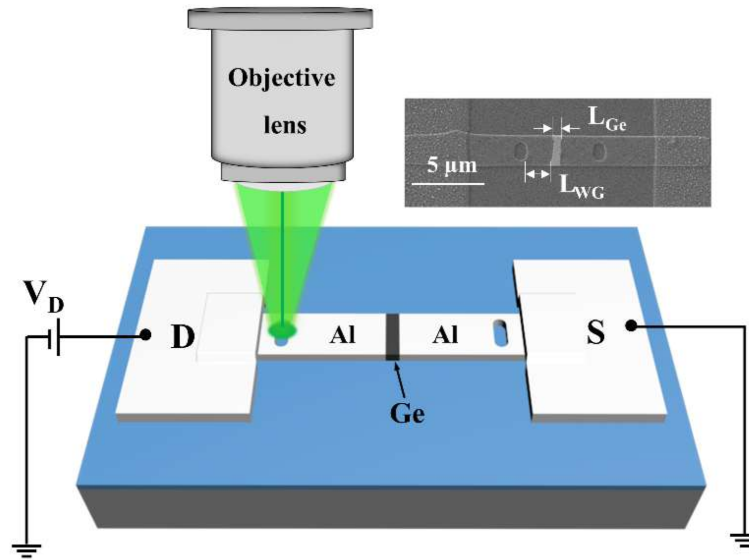

Figure 4.15 The layout of a plasmonic antenna-coupled Al-Ge-Al heterojunction used for plasmon-induced hot-carrier detector. The inset shows an SEM image of the Al-Ge-Al heterojunction device with two oval-shaped trenches. The annotations L_{WG} and L_{Ge} denote the length of the SPP waveguide and Ge channel, respectively.

Thus generated SPPs propagate in both directions (i.e. toward and away from the Ge segment). While SPPs move from the plasmon coupler to the Al/Ge interface, they are damped following an exponential decay law, determined by the imaginary part of the refractive index of the metal[61]. The distance at which the magnitude becomes 1/e of its initial value refers to as "propagation length", characterizing the capability of Al feed lines to guide SPPs. Aside of scattering at surface imperfections of the Al waveguide intrinsic Landau damping[96] is a main loss mechanism resulting in hot electron-hole pairs. The energy distribution of these electrons and holes originated from the non-radiative decay of SPPs is thereby determined by the electronic structure and density of states of the material[97,98].

However, under a rigorous treatment accounting for the electron dispersion in the metal, only some of the hot carriers within the distance of the mean free path will arrive at the Al-Ge

Die approbierte gedruckte Originalversion dieser Dissertation ist an der TU Wien Bibliothek verfügbar.
The approved original version of this doctoral thesis is available in print at TU Wien Bibliothek.
TU Bibliothek WIEN Your knowledge hub

interface without undergoing inelastic collisions. Afterward, only the hot electrons with proper momentum and sufficient energy can surpass the Schottky contact and will be injected into the adjacent Ge segment. Those hot electrons without sufficient energy would be reflected back and dispersed by the scattering with free electrons or phonons in Al. However, hot carriers injected into the Ge segment will be accelerated by the external electric field and collected at the opposite electrode.

Thus, it can assume that the current measured in the Al-Ge-Al device is proportional to the plasmon intensity at the Al-Ge interface and also the laser light intensity. However as will be shown, one has to take into account the nonlinearity of the Ge photodetectors due to the plasmon-gating effect. Before discussing the plasmon-gating effect, the impact of the dimension of the Al-Ge-Al heterostructure (Ge segment as well as Al SPP waveguide) on the plasmonic properties is discussed. **Figure 4.16** shows the plasmon current I_{pl} as a function of the Ge channel length under laser irradiation with λ = 532 nm and λ = 785 nm at the same excitation laser power of 500 μW at a drain bias of V_D = 100 mV and V_{BG} = 0 V.

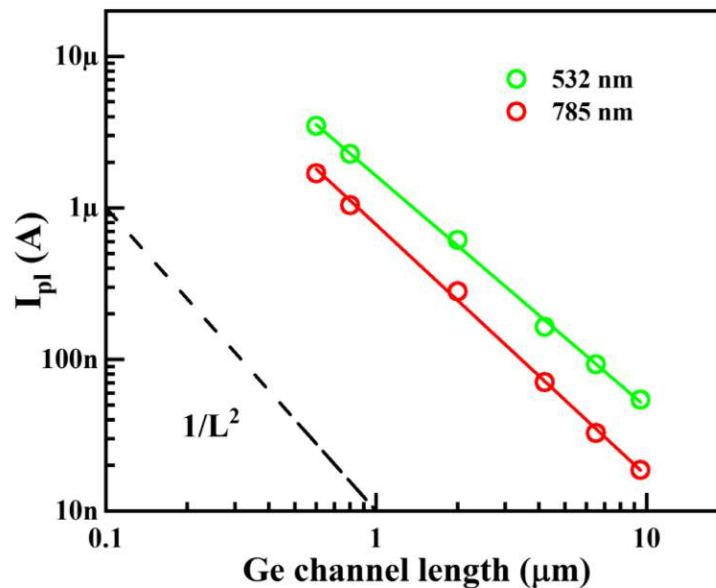

Figure 4.16 Plasmon current I_{pl} as a function of the Ge channel length measured for the green (λ = 532 nm) and red (λ = 785 nm) laser excitation. The measurements required a constant SPP waveguide length (i.e. L_{WG} = 3 μm) and various channel lengths L_{Ge}. The applied light power is 500 μW. The drain and back-gate voltages are V_D = 100 mV and V_{BG} = 0 V, respectively.

Die approbierte gedruckte Originalversion dieser Dissertation ist an der TU Wien Bibliothek verfügbar.
The approved original version of this doctoral thesis is available in print at TU Wien Bibliothek.
TU Bibliothek WIEN Your knowledge hub

Again in analogy to a common photodetector, the plasmon current I_{pl} follows[37]

$$I_{pl} \propto \frac{\tau_l}{\tau_{tr}} \tag{4.18}$$

with τ_l and τ_{tr} the effective lifetime of the SPP-induced carriers and the transit time of the carriers through the Ge channel, respectively. The carrier transit time can be derived according to $\tau_{tr} = L_{Ge}^2/(\mu \cdot V_D)$ with μ the carrier mobility and V_D the applied drain bias. Thus, the plasmon current appears to be inversely proportional to the square of the channel length, as depicted in **Figure 4.16**.

Notably the effective carrier lifetime τ_l does not simply denote the lifetime of the injected hot carriers before recombination, but rather the lifetime related to the traps inducing plasmon-gating[99]. This also explains the higher plasmon current observed for green laser irradiation, inducing the injection of higher energetic electrons into the Ge segment. More hot electrons can surpass the barrier and thus more and higher energetic traps are filled increasing the plasmon-gating and thus I_{pl}. For the device with 3 μm long SPP waveguide and the shortest Ge channel of L_{Ge} = 650 nm, an external quantum efficiency of EQE = 2.5% can be derived. Although no optimization with respect to effective plasmon coupling or waveguiding has been done yet, this is quite remarkable since for other electrical plasmon detectors EQEs of less than 1% have been reported[94,100].

For all these measurements on devices with different Ge channel lengths, the Al feed lines were kept constant and short to minimize losses in the plasmon propagation. It is reasonable to assume that the number of the injected hot carriers linearly depends on the amount of SPPs approaching the Al/Ge interface. However, due to the plasmon-gating effect of the Ge photodetector, the relationship between the injected hot carriers and the plasmon current I_{pl} is non-linear. In order to investigate this non-linear relationship, requires light power dependent measurement. The inset of **Figure 4.17** demonstrates that the plasmon current I_{pl} follows the function $I_{pl} \propto P^{0.61}$ within the investigated regime. After a respective calibration, **Figure 4.17** shows the plasmon current as the function of the lengths of the Al waveguide for green (532 nm) and red (785 nm) laser illumination of the plasmon coupler for a constant Ge segment length of 3 μm). With the linear fitting in the log-log plot, the propagation length L_p of the monolithic Al feed lines is calculated as 1.64 μm and 3.08 μm at the exciting wavelength of λ = 532 nm and λ = 785 nm, respectively.

Die approbierte gedruckte Originalversion dieser Dissertation ist an der TU Wien Bibliothek verfügbar.
The approved original version of this doctoral thesis is available in print at TU Wien Bibliothek.
TU WIEN Bibliothek Your knowledge hub

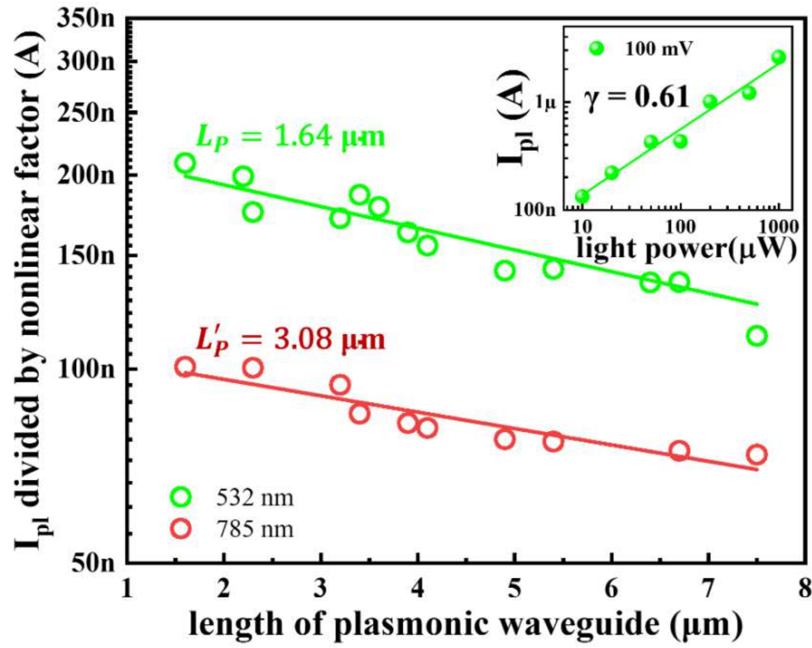

Figure 4.17 Propagation length of SPPs on the monolithic Al feed line measured for the green (λ = 532 nm) and red (λ = 785 nm) laser excitation. The measurement requires devices with different lengths of the plasmonic waveguide, but the Ge channel lengths were always kept constant (i.e. L_{Ge} = 3 µm in this case). The inset demonstrates the plasmon current as a function of the light power for an Al-Ge-Al heterostructure transistor with a 3 µm long SPP waveguide and a 600 nm long Ge channel.

Die approbierte gedruckte Originalversion dieser Dissertation ist an der TU Wien Bibliothek verfügbar.
The approved original version of this doctoral thesis is available in print at TU Wien Bibliothek.
TU Wien Bibliothek Your knowledge hub

4.1.3.4 Plasmon-gating effect

4.1.3.4.1 The impact of gate voltage on plasmon-gating effect

As shown in **Chapter 4.1.3.1**, the electrical behavior of Al-Ge-Al heterostructure devices is significantly influenced by surface traps in the Ge channel, inducing e.g. NPC or PPC. Here we will investigate whether this control of the occupation of the traps and thus modulated electrical performance can also be induced plasmonically. In order to survey if traps can capture the SPP-induced hot carriers, an Al-Ge-Al transistor with a channel length of L = 600 nm and width of W = 2.5 μm is investigated (see **Figure 4.18a**). **Figure 4.18b** depicts its transfer characteristics measured in dark and under laser irradiance (λ = 532 nm) of the plasmon coupler at various light power.

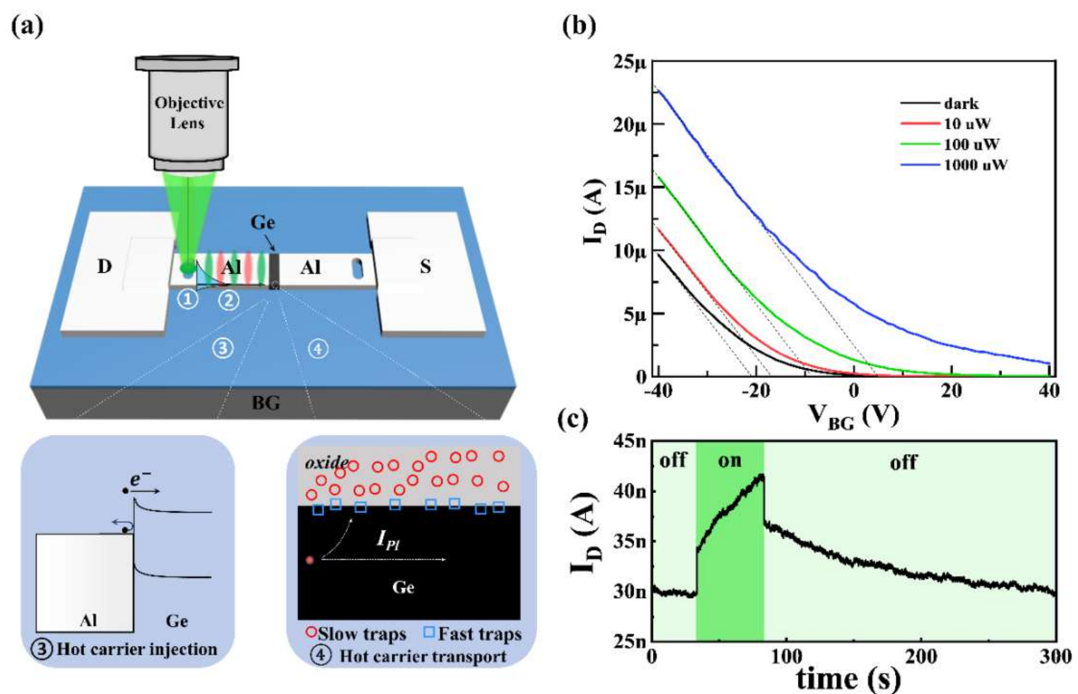

Figure 4.18 (a) The diagram schematically describes the working principles of plasmon-gating, including excitation of SPPs at the plasmon coupler, propagation of SPPs along the Al feed line, and hot carriers transport in the Ge channel. The right-upper inset depicts the SEM image of an Al-Ge-Al heterostructure with two plasmon couplers. (b) The comparison of the transfer curves of the Al-Ge-Al heterostructure SBFET in dark and under irradiation of one plasmonic coupler with various light power. Drain voltage is V_D = 100 mV. (c) Transient response to a laser pulse at $V_D = V_{BG}$ = 0 V.

Die approbierte gedruckte Originalversion dieser Dissertation ist an der TU Wien Bibliothek verfügbar.
The approved original version of this doctoral thesis is available in print at TU Wien Bibliothek.
TU Bibliothek Your knowledge hub WIEN

As already discussed above, the Al-Ge-Al SBFET behaves in the dark like a p-channel enhancement mode transistor with the characteristic sharp increase of the drain current of negative gate voltages. Notably, such p-type behavior does not originate from unintentional Al doping of Ge segment induced by the Al diffusion, but is commonly observed for unpassivated Ge-based devices due to effective surface doping[77]. For the actual 75 nm thick Ge channel, negatively charged surface states at the GeO_x/Ge interface and traps in the native oxide determine the electronic response[30].

Under laser irradiance the overall shape of the transfer characteristic remains essentially the same, but somewhat shifted toward more positive gate voltages. This shift of the threshold voltage is reflected in an increase of the drain current in the hole accumulation and depletion regime, referred further as plasmon-gating effect. Unlike common photogating[70,101] with light directly exciting the semiconductor, in this case the photogating may be originated from SPPs generated at the plasmonic coupler. In particular, hot charge carriers arising from the non-radiative decay of these SPPs at the Al-Ge interface may fill the above-mentioned, localized surface states and traps. These now negatively charged traps localized in close proximity to the current-carrying channel of the Al-Ge-Al SBFET act as a very effective local gate and cause the observed shift in threshold voltage. The strength of this plasmon-gating effect becomes clear at even higher irradiation powers where shifts in the threshold voltage of several tens of volts occur (see **Figure 4.18b**).

Although there are many reports on the common photogating effect when the semiconductor is directly exposed to light, the particular properties of SPP-induced hot carrier trapping are actually unexplored. The injection of hot charge carriers induced by the decay of SPP at the Al-Ge interface may change both the carrier density Δn as well as the carrier mobility $\Delta\mu$ and thus modify the conductivity $\Delta\sigma$ of the SBFET according to

$$\Delta\sigma = q\mu_0 \Delta n + nq\Delta\mu \qquad (4.19)$$

with q the elementary charge, μ_0 the initial carrier mobility and n the initial carrier density. According to **Figure 4.18b** the carrier mobility remains unchanged up to the highest irradiation power thus **Eq. 4.19** can be written as

$$\Delta\sigma = q\mu_0 \Delta n = q\mu_0 g \tau_l(g) \qquad (4.20)$$

with g the SPP induced injection rate of hot electrons equivalent to the photoexcitation rate and τ_l the effective lifetime of the hot carriers. The effective lifetime must also be assumed to be dependent on the injection rate g which in turn may depend on the power P of the excitation laser.

Die approbierte gedruckte Originalversion dieser Dissertation ist an der TU Wien Bibliothek verfügbar.
The approved original version of this doctoral thesis is available in print at TU Wien Bibliothek.
TU WIEN Bibliothek Your knowledge hub

Under light power modulated measurement in **Figure 4.19**, the plasmon current I_{pl} follows a current-power law

$$I_{pl} \propto b \cdot P^{\gamma} \tag{4.21}$$

with b a scaling factor, P the light power and γ the dimensionless exponent of the power law[102]. Light power-dependent measurements are carried out at various back-gate voltages and the resulting data are depicted in **Figure 4.19**. The sublinear relation gradually transfers to superlinear while the gate voltage increases from V_{BG} = -40 V to V_{BG} = 40 V.

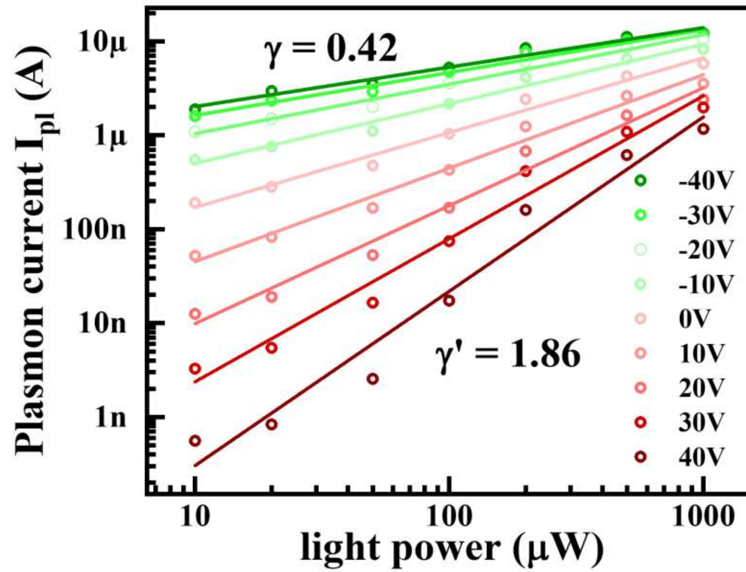

Figure 4.19 Plasmon current as a function of light power measured at various gate voltages V_{BG}. The drain voltage is set at V_D = 100 mV and the applied laser wavelength is 532 nm.

A superlinear relationship indicates that the device is more sensitive to SPPs with excitation power ascending, due to the longer effective carrier lifetime under higher light power. The superlinear law is also referred to as photo-sensitization[103,104] describing a process of enhancing the sensitivity of a photodetector. The superlinear behaviour is a typical phenomenon originating from the two-center recombination effect[103].

Before discussing the transition from sublinear to superlinear response behaviour, the differences of the one-center and two-center recombination models are briefly discussed:

(1) The one-center recombination model. In **Figure 4.20a**, regarding to the definition of the lifetime $\tau_l = \frac{1}{N \cdot \beta}$ (where N is the number of empty trap states and β the capture cross section), an electron has the minimum lifetime when all the imperfections are empty.

Die approbierte gedruckte Originalversion dieser Dissertation ist an der TU Wien Bibliothek verfügbar.
The approved original version of this doctoral thesis is available in print at TU Wien Bibliothek.
TU Bibliothek WIEN Your knowledge hub

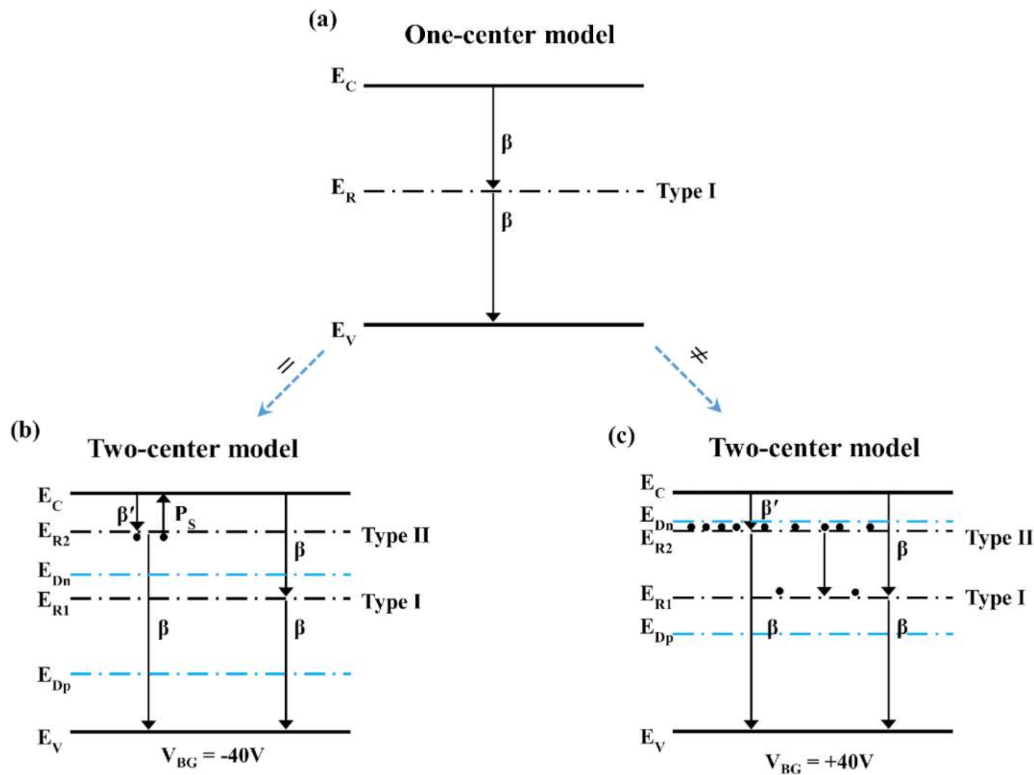

Figure 4.20 Schematic illustration of non-radiative recombination models: (a) a common model containing only one recombination center; (b) the introduction of type II centers located above E_{Dn} does not affect the condition of (a); (c) when the location of type II centers becomes below E_{Dn}, these centers will become activators, sensitizing the photoconductor and increasing its photoconductivity. E_{Dn} and E_{Dp} are the demarcation level of electrons and holes, respectively. E_R is the trap energy level. E_{R1} and E_{R2} are the trap energy level for type I and type II, respectively. β and β′ are the capture cross-section for the type I and type II center, respectively

(2) The two-center recombination model. Generally, a captured carrier at an imperfection may do one of two things: (i) recombine with a carrier of the opposite type, or (ii) be thermally re-excited to the nearest energy band before recombination occurs[66]. In the latter case the imperfection is referred to as a trap, and the capture and release processes are denoted as trapping and detrapping. The corresponding imperfections that allow the captured carrier to carry out these two types of behaviors are denoted as recombination centers and sensitizing centers, respectively. The actual action of an imperfections is determined by the position of demarcation levels for electrons and holes. The electron demarcation level E_{Dn} is defined as energy level where an electron has an equal probability of being thermally excited to the conduction band and recombining with a hole in the valence band, and the similar concept can

Die approbierte gedruckte Originalversion dieser Dissertation ist an der TU Wien Bibliothek verfügbar.
The approved original version of this doctoral thesis is available in print at TU Wien Bibliothek.
TU Bibliothek WIEN Your knowledge hub

be applied to the hole demarcation level E_{Dp}. The imperfection works like a recombination center, if located between the electron demarcation level E_{Dn} and the hole demarcation level E_{Dp}, otherwise like a sensitizing center. In a first approximation the demarcation level can be replaced by the quasi-Fermi level E_{Fn}[104,105]. The relationship between the quasi-Fermi level E_{Fn} and the electron demarcation level E_{Dn} can be expressed as

$$E_C - E_{Dn} = (E_C - E_{Fn}) - kT \cdot ln\left[(m_h^*/m_e^*)/(\beta_p/\beta_n)\right] \quad (4.22)$$

with k the Boltzmann constant, T the room temperature, m_e^* and m_h^* the effective masses of electrons and holes, β_p and β_n the capture cross section of electrons and holes, respectively. The electron demarcation level E_{Dn} differs from the quasi-Fermi level E_{Fn} only by a factor of kT times the natural logarithm of the ratio of the capture cross section of electrons and holes. Normally this difference is quite small at room temperature, thus the electron demarcation level E_{Dn} could be regarded as the quasi-Fermi level E_{Fn}[103].

At the back-gate voltage of V_{BG} = -40 V, the type II center E_{R2} lies above the quasi-Fermi level E_{Fn}, acting as a sensitizing center and the captured electrons may be thermally emitted to the conduction band (See **Figure 4.20b**). Subsequently, the trapping and detrapping of electrons at the type II center E_{R2} would realize the thermal equilibrium, thus not affecting the recombination kinetics. Thus, at the back-gate voltage of V_{BG} = -40 V, the two-center recombination model can be regarded as the one-center recombination model.

While increasing the back-gate voltage, the quasi-Fermi level E_{Fn} for electrons would shift toward the conduction band E_C, subsequently being above the type II center E_{R2} (**Figure 4.20c).** Thereby, the type II center E_{R2} will convert from a sensitizing center to a recombination center, taking part in the recombination process. Subsequently, the electrons initially in the type II center E_{R2} are effectively transferred to the type I center E_{R1} due to smaller capture cross section and longer lifetime of electrons in the type II center E_{R2}, thereby decreasing the density of empty states in the type I center E_{R1}. Consequently, the effective carrier lifetime strengthens because free electrons would encounter mostly empty states with a small capture cross-section in the type II center E_{R2} and only a few empty states with a large capture cross-section in the type I center. Overall, this results in a decrease in the rate of recombination and an increase in the effective carrier lifetime.

4.1.3.4.2 The impact of drain voltage on plasmon-gating effect

As the following experiment regarding the transient behaviour of the SBFET are performed at V_{BG} = 0 V. The light power dependence id investigated for the ungated SBFET at different

TU Bibliothek Your knowledge hub WIEN
Die approbierte gedruckte Originalversion dieser Dissertation ist an der TU Wien Bibliothek verfügbar.
The approved original version of this doctoral thesis is available in print at TU Wien Bibliothek.

drain voltages. **Figure 4.21** shows the plasmon current I_{pl} measured at two different drain biases of V_D = 10 mV and V_D' = 100 mV and the gate voltage of V_{BG} = 0 V as a function of the light power of the 785 nm laser impinging on the plasmon coupler.

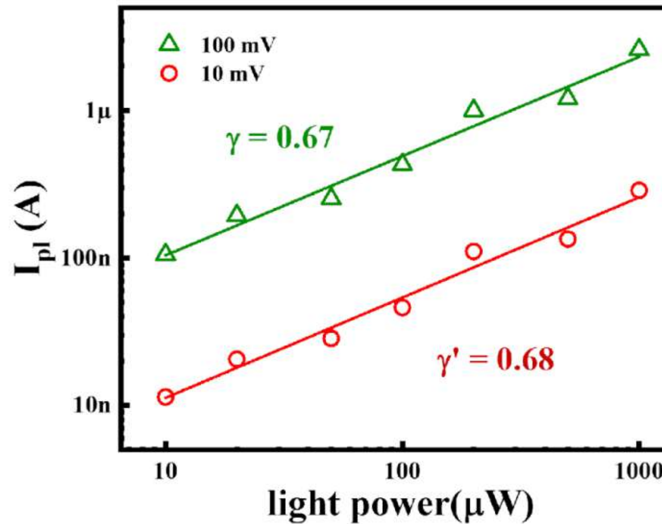

Figure 4.21 Plasmon current I_{pl} as the function of light power under different drain bias. The measurement is carried out at a gate voltage of V_{BG} = 0 with a 785 nm laser impinging the plasmonic trench of the SBFET shown in **Figure 4.18a**.

According to the power-current law (see **Eq. 4.21**), the exponent is fitted as $\gamma = 0.67$ at V_D = 10 mV. The sublinear relationship $I_{pl} \propto P^{0.67}$ derives that the effective lifetime τ_l is inversely proportional to the injection rate G at a gate voltage of V_{BG} = 0 V (i.e. $\tau_l\,(\mathcal{g}) \propto \mathcal{g}^{-0.33}$), demonstrating a shorter effective lifetime τ_l at higher light power. It can be explained well by the one-center recombination theory. Further, the exponent becomes $\gamma' = 0.68$ at a drain voltage of V_D' = 100 mV. At both drain voltages the sublinear relationship between plasmon current I_{pl} and the light power is found to be the same. Therefore, there is obviously no impact of the drain voltage V_D on the capturing of SPP-induced hot electrons injected into the Ge segment.

Die approbierte gedruckte Originalversion dieser Dissertation ist an der TU Wien Bibliothek verfügbar.
The approved original version of this doctoral thesis is available in print at TU Wien Bibliothek.
TU Bibliothek WIEN Your knowledge hub

4.1.3.4 Ultra-fast hot-carrier photodetector

The previous sections have demonstrated the feasibility of a monolithic Al-Ge-Al SBFET with plasmon couplers for generation and waveguiding of SPPs, as well as the detection of hot carriers resulting from the non-radiative decay of SPP at the Al-Ge interface. The ultimate goal was to develop an ultra-fast on-chip photodetection system that is scalable and CMOS compatible. The speed of the advanced nanoscale laser sources and modulators can easily approach tens of GHz[106–108], whereas scalable high-speed photodetectors as the receivers are still a challenge. The efficiency-speed trade-off[109,110] makes it challenging to shrink the channel of semiconductor photodetectors, due to the low absorption below the diffraction limit. Typically, the response speed of a photodetector is determined by the carrier transit time[111] and the RC time constant. As the carrier transit time depends on the charge carrier mobility and the active channel length of the device, the Al-Ge-Al device was finally scaled below the mean free path of electrons in Ge[32], enabling ballistic transport in the Ge channel. A pump-probe cross-correlation technique was employed to demonstrate experimentally the potential of such an ultra-scaled Al-Ge-Al photodetector with ballistic charge carrier transport to handle optical signals around 50 GHz at telecom wavelength and with high responsivity. **Figure 4.22a** illustrates the device architecture of the proposed ultrafast hot-carrier photodetector based on a monolithic Al-Ge-Al heterostructure.

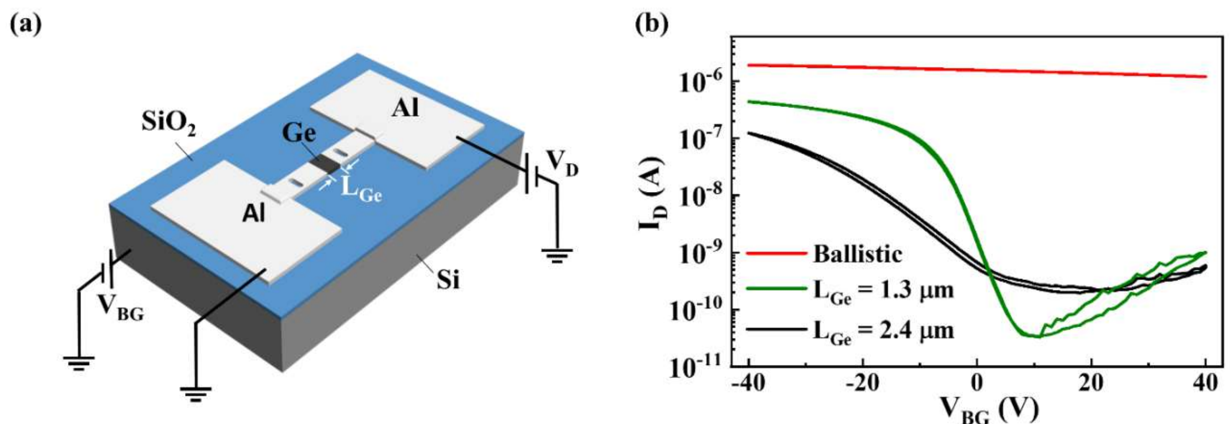

Figure 4.22 (a) The layout of the Al-Ge-Al heterostructure transistor. In this device layout the Ge segment, Al feed lines connected with macroscopic pads, buried gate oxide (150 nm SiO_2) and the doped Si handle wafer serves as the semiconductor channel, source/drain, gate insulator and the common back gate, respectively. (b) Transfer curves measured from Al-Ge-Al heterostructure transistors with various Ge channel lengths. The drain bias is V_D = 10 mV.

Die approbierte gedruckte Originalversion dieser Dissertation ist an der TU Wien Bibliothek verfügbar.
The approved original version of this doctoral thesis is available in print at TU Wien Bibliothek.
TU Bibliothek WIEN Your knowledge hub

The overall fabrication process is similar to the one that is described in the experimental section (see **Chapter 3.1**), further passivated with an 8 nm thick Al_2O_3 layer. In order to investigate the impact of the channel length, three devices with various Ge channel length L_{Ge} are investigated and their corresponding transfer curves are depicted in **Figure 4.22b.** The two longer transistors exhibit apparent bipolar conductance modulated via the back gate. Thus, a hole- and an electron dominated transport regime shows up at $V_{BG} < 0$ V and $V_{BG} > 20$ V, respectively. Compared to un-passivated Ge transistor (see **Figure 4.10a**), these transistors passivated by Al_2O_3 show less hysteresis for double back-gate-sweeping measurements.

Scaling down channel length to $L_{Ge} = 1.3$ µm, both the on-current and the on/off-ratio are enhanced. With further scaling of the transistor, the bipolarity of the SBFET is lost and it can generally no longer be controlled by the back-gate. These device with a Ge channel length close to the mean free path of electrons in Ge (i.e. 45 nm [112]), will be further denoted as ballistic device.

4.1.3.4.1 Scanning photocurrent microscopy

The Al-Ge-Al heterostructure device with the channel length of $L_{Ge} = 1.3$ µm is shown in the SEM image in **Figure 4.23a**. The bottom image shows the spatially dependent photocurrent at zero gate (V_{BG}) and bias (V_D) voltages, which is measured via the scanning photocurrent microscopy with a linearly polarized laser spot at the wavelength of 532 nm and the diameter of 860 nm. The compact light spot enables a high spatial resolution, allowing to figure out the various working mechanism at different local positions of the Al-Ge-Al heterostructure device. Green arrows mark the corresponding locations for Al/Ge interfaces and the plasmon couplers. The magnitude and sign of the photocurrent reflects the individual efficiency and the directions of the hot carriers' movement, respectively.

Die approbierte gedruckte Originalversion dieser Dissertation ist an der TU Wien Bibliothek verfügbar.
The approved original version of this doctoral thesis is available in print at TU Wien Bibliothek.
TU WIEN Bibliothek Your knowledge hub

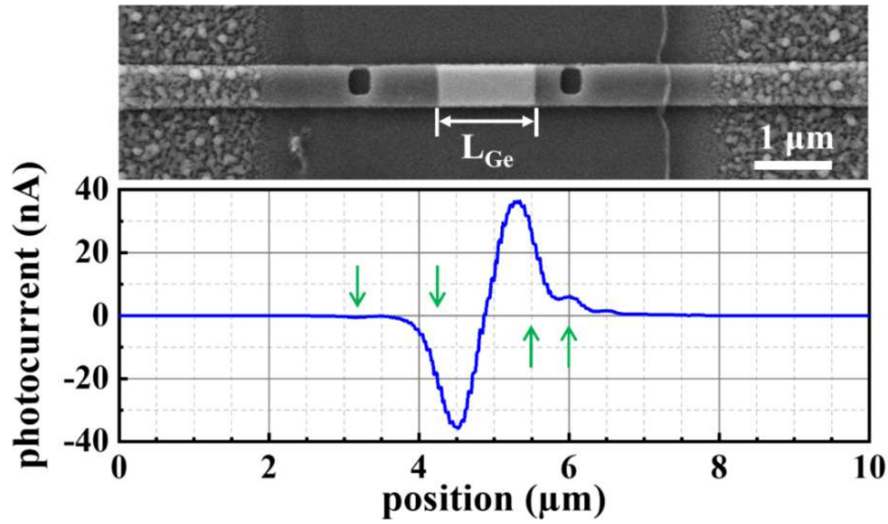

Figure 4.23 Scanning photocurrent measurement of as the Al-Ge-Al SBFET with a Ge segment length of 1.3 µm. The upper and lower panels show the SEM image and the generated photocurrent as a function of the scanning position, respectively. The positions of plasmon couplers and two Al/Ge interfaces are highlighted by the green arrows. The wavelength and light power of the laser beam are 532 nm and 1 µW, respectively. The drain bias and gate voltage are set as V_{BG} = 0 V and V_D = 0 V, respectively.

When the scanning light spot focusses on the Al/Ge interface, a significant photocurrent is generated as the built-in electric field of the Schottky contact induces the drift of photogenerated charge carriers. Further, due to the direction of the built-in electric field, a different polarity of photocurrent results at the two Al/Ge interfaces but their magnitude is similar. The current observed when the laser is atop of the plasmon coupler, originate from the plasmon-induced hot carriers, and the corresponding working principle has been explained before (please see **Chapter 2.4**). The polarity changes for the current generated at the left and right trench, due to the different hot carriers' movement direction. The different magnitude of the plasmon induced current is due to different propagation lengths along the monolithic Al waveguide and thus different losses.

4.1.3.4.2 Spectral responsivity of SBFET detector

Figure 4.24 illustrates the spectrally resolved responsivity R of three Al-Ge-Al heterostructure devices with channel lengths of 2.4 µm, 1.3 µm and ballistic one.

Die approbierte gedruckte Originalversion dieser Dissertation ist an der TU Wien Bibliothek verfügbar.
The approved original version of this doctoral thesis is available in print at TU Wien Bibliothek.
TU Bibliothek WIEN Your knowledge hub

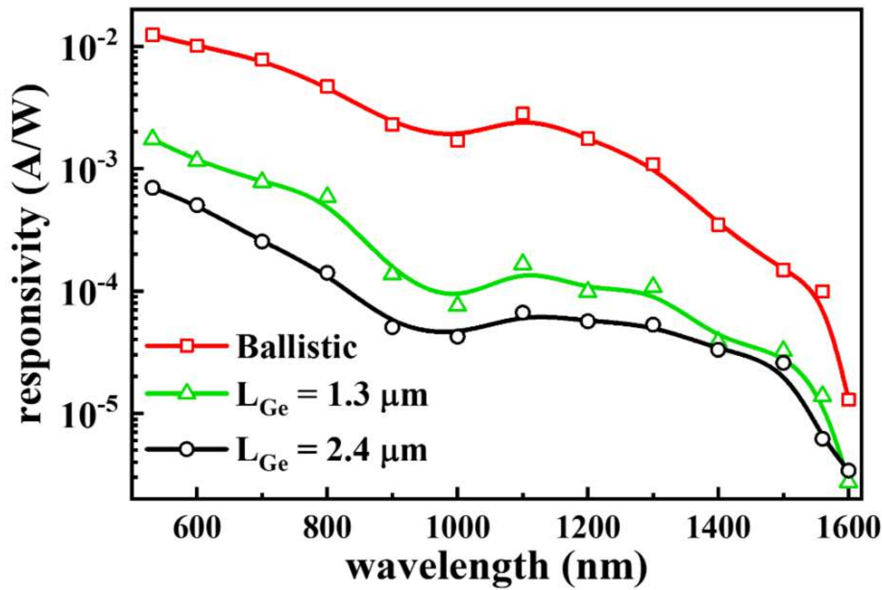

Figure 4.24 Spectral responsivity of Al-Ge-Al heterostructure photodetectors with various Ge channel lengths. Gate voltage and the drain bias are $V_{BG} = 0$ and $V_D = 0$ V, respectively.

All three devices exhibit broad responses covering the visible and near-infrared regions. Notably, the responsivity increases with decreasing channel length, with a maximum responsivity of 12 mA/W at λ = 532 nm and approximately 0.35 mA/W at the telecom wavelength of λ = 1560 nm for the ballistic device. Such remarkable responsivity obtained from the ballistic device can be explained by the undisturbed transport process of hot carriers without any scattering. The distinct responsivity roll-off observed near 1600 nm corresponds to the Ge bandgap optical absorption edge.

4.1.3.4.3 Pump-probe cross-correlation measurements

To determine the time response of the monolithic Al-Ge-Al heterostructure based photodetector, a modified pump-probe cross-correlation technique is used where the electrical signal generated by the Al-Ge-Al SBFET is directly measured. Standard pump-probe technique commonly characterizes the transient change of optical properties of the target materials. A photodetector, in general, features at least two different response mechanisms - an absorption process of photons leading to a generation of free charge carriers, and further the movement of these carriers in the detector inducing the signal current. These take place on very different time scales; photons are absorbed as long as the optical pulse lasts, while photogenerated carriers' movement lags behind the optic pulse due to their mass and distance to travel. Commonly, the later process limits the detector capability to distinguish subsequent

Die approbierte gedruckte Originalversion dieser Dissertation ist an der TU Wien Bibliothek verfügbar.
The approved original version of this doctoral thesis is available in print at TU Wien Bibliothek.
TU Bibliothek WIEN Your knowledge hub

pulses and sets an upper limit for the maximum pulse rate to be detected. **Figure 4.25a** shows cross-correlation signal as a function of time delay Δt between two pulses for the Al-Ge-Al heterostructure devices with the longest channel length of L_{Ge} = 2.4 μm and the laser beam focused on the plasmon coupler.

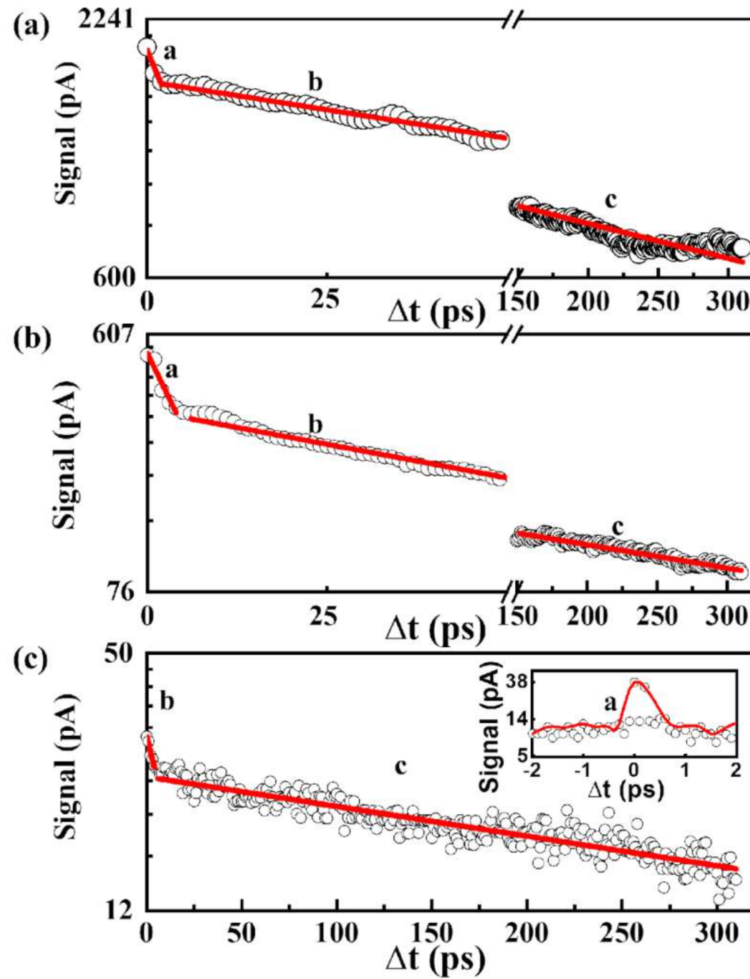

Figure 4.25 The impact of the Ge channel length on the pump-probe signal for SBFET devices with (a) L_{Ge} = 2.4 μm, (b) L_{Ge} = 1.3 μm and (c) the ballistic device (L_{Ge} < 100 nm). The semi-logarithmic plot is employed to fit the individual time constants. The inset of panel **c** demonstrates the enlarged region measured with a high temporal resolution.

It can be clearly seen that the semi-logarithmic plot can be divided into three well distinguished regimes, marked as a, b and c in sequence, corresponding to time constants of signal decay of 11, 172 and 559 ps, respectively.

Region (a) should involve the time taken by the generation and waveguide of SPPs, as well as the injection of hot carriers[113]. The excitation of SPPs in principle is a non-linear process of

Die approbierte gedruckte Originalversion dieser Dissertation ist an der TU Wien Bibliothek verfügbar.
The approved original version of this doctoral thesis is available in print at TU Wien Bibliothek.
TU Bibliothek WIEN Your knowledge hub

transferring the energy of the laser pulse to a coherent oscillation of electrons in the metal. The respective time constant should thus be equal to the pulse width. Due to a short waveguide length of L_{WG} = 1.5 µm, propagation to the Al-Ge interface takes several femtoseconds. The injection of hot electrons at the Al/Ge interface is also known to be a fast process (i.e. on the fs time scale)[114]. Nevertheless, the thermalization process of hot carriers, based on electron-phonon scattering and phonon-phonon scattering, is known as a long event that can endure for several picoseconds[115,116].

Region (b) with the longer time constant of 172 ps is related to the transit of hot charge carriers through the channel. The transit time τ_{tr} results from[37]

$$\tau_{tr} = \frac{L_{Ge}}{v_{eff}} \tag{4.23}$$

where L_{Ge} is the length of the Ge segment and v_{eff} is the effective drift velocity of charge carriers moving inside Ge. As the saturation drift velocity of electrons in bulk Ge is 5×10^6 cm/s[117], the corresponding minimum transit time for electrons moving through the Ge segment with a length of 2.4 µm can be derived as 40 ps, which is apparently shorter than the measured one, suggesting the effective drift velocity v_{eff} in such a monolithic Al-Ge-Al heterostructure device is much less than that in bulk Ge. The reduced effective drift velocity v_{eff} should originate from the enhanced surface scattering of charge carriers when moving in a thin Ge micro-ribbon with a thickness of only 75 nm.

Region (c) features the longest time constant of 559 ps, originating from surface trapping. According to Prasamkumar et al.[118], the carrier relaxation dynamics controlled by the surface trapping effect can last for several nanoseconds. Although a protective Al_2O_3 layer has been deposited atop of the Ge micro-ribbons to enhance the reliability and reproducibility of photodetectors' electrical performances, a thin native GeO_x layer with trapping states may still exist between the Ge micro-ribbon and the Al_2O_3 layer, causing the unintentional change of the channel conductivity.

The related pump-probe cross-correlation curves for the device with a shorter channel length of L_{Ge} = 1.3 µm is depicted in **Figure 4.25b** and the thereof determined time constants are listed in **Table 4.5**. Compared to the longer Al-Ge-Al heterostructure device, this device exhibits similar behaviour with similar time constants for thermalization (i.e. region a) and the interaction with surface traps (i.e. region c). No surprisingly, according to **Eq. 4.23**, the transit time becomes half when the channel length L_{Ge} is scaled down to half of the initial value.

Die approbierte gedruckte Originalversion dieser Dissertation ist an der TU Wien Bibliothek verfügbar.
The approved original version of this doctoral thesis is available in print at TU Wien Bibliothek.
TU Bibliothek WIEN Your knowledge hub

Table 4.5 Time constants for SBFET devices with different channel lengths.

Channel length L_{Ge}	Time constant τ (ps)		
	Region a	Region b	Region c
2.4 µm	11 ± 3	172 ± 2	559 ± 11
1.3 µm	8 ± 1	92 ± 1	529 ± 7
(<100 nm)	0.6	23 ± 5	369 ± 65

Finally, the pump-probe results for the ballistic device are depicted in **Figure 4.25c**. The duration of region (a) is ultra-short. **Figure 4.25c** mainly illustrates region b and c with the time duration of approximately 23 ps and 369 ps, respectively. The inset of **Figure 4.25c** shows the measurement at a higher time resolution of 0.1 ps. It indicates an ultra-short time constant of only 0.6 ps, close to the temporal resolution of this modified pump-probe setup (see **Figure 3.7**). Such ultra-fast sub-picosecond process results from the fast generation of hot carriers and the related quasi-ballistic transport.

Die approbierte gedruckte Originalversion dieser Dissertation ist an der TU Wien Bibliothek verfügbar.
The approved original version of this doctoral thesis is available in print at TU Wien Bibliothek.
TU Bibliothek WIEN Your knowledge hub

4.2 Al-Si-Al heterostructure

4.2.1 The formation of Al-Si-Al heterostructure devices

The actual fabrication scheme is overall the same as that for the Al-Ge-Al heterostructures, although here, of course, an SOI wafer is used as substrate material and the temperature for the solid-state exchange between Al-Si is somewhat higher. **Figure 4.26a** shows an optical image of a 110 nm thick and 2.5 µm wide Si nanosheet overlapped with two sputtered Al pads, forming a predesigned channel length of 25 µm. Because of the close proximity of Al and Si in the periodic table of elements, SEM images would display an exceedingly low degree of contrast of Al and Si regions, making them indistinguishable. Therefore, optical images captured by high-resolution microscopy are depicted here.

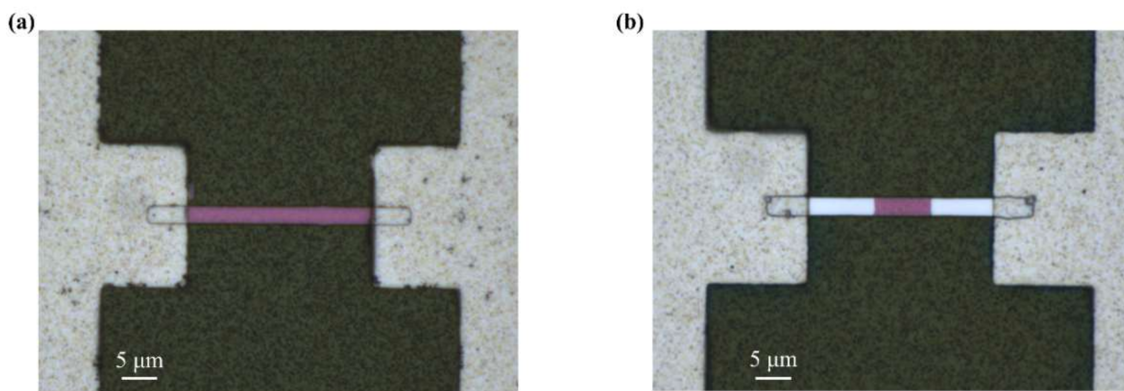

Figure 4.26 (a) The initial device with the Si nanosheet contacted by two sputtered Al pads. (b) The Al-Si-Al heterostructure after annealing at 773 K for 30 minutes. The width and thickness of the Si channel are 2.5 µm and 110 nm, respectively. The thickness of sputtered Al pads is 125 nm.

The Al/Si exchange requires a higher temperature of about 773 K, compared to 673 K for Al/Ge exchange, and appeared also to be dependent on the thickness and width of the Si nanoribbons. **Figure 4.26b** shows a shorter Si segment with the length of L_{Si} = 7.7 µm with sharp interface, after annealing at 773 K for 30 min, proving the successful Al-Si exchange. Again, the Al/Si exchange presents a compelling technology for effective and reliable device scaling.

Die approbierte gedruckte Originalversion dieser Dissertation ist an der TU Wien Bibliothek verfügbar.
The approved original version of this doctoral thesis is available in print at TU Wien Bibliothek.
TU Bibliothek WIEN Your knowledge hub

4.2.2 Basic electrical properties of Al-Si-Al heterostructure devices

4.2.2.1 Current/voltage characteristics

The fabrication of the Al-Si-Al heterostructures on an SOI wafer again results in a back gated SBFET device configuration. Same as for the Al-Ge-Al heterostructure devices electrical measurements, I/V and transfer characteristics are measured to characterize the electrical properties of the Al-Si-Al heterostructure SBFET. **Figure 4.27** depicts the I/V curves of an Al-Si-Al SBFET with a channel length of L = 5 µm at various back-gate voltages.

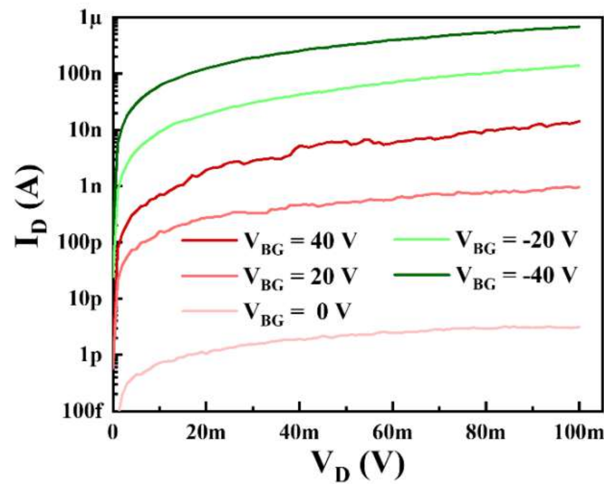

Figure 4.27 I/V characteristics of an Al-Si-Al SBFET with a channel length of L_{Si} = 5 µm for different back-gate voltages. The width and thickness of the Si channel are 2.5 µm and 110 nm, respectively.

As the back-gate voltage V_{BG} rises from -40 V to +40 V, the drain current I_D initially exhibits a decline until a minimum value (at V_{BG} = 0 V), followed by an increase. The altered drain current is due to the modulation of effective barrier height, as discussed before. The observed distinct modulation provides evidence for the successful fabrication of the Al-Si-Al SBFETs in the back-gate configuration.

4.1.2.2 Transfer characteristics of Al-Si-Al SBFET

Figure 4.28 shows the transfer characteristics of an Al-Si-Al heterostructure SBFET with a channel length of L = 5 µm at different drain bias V_D.

TU Bibliothek Your knowledge hub WIEN
Die approbierte gedruckte Originalversion dieser Dissertation ist an der TU Wien Bibliothek verfügbar.
The approved original version of this doctoral thesis is available in print at TU Wien Bibliothek.

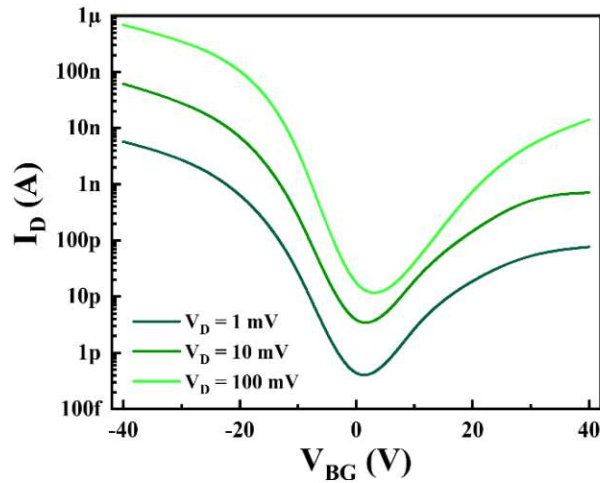

Figure 4.28 Transfer curves of an Al-Si-Al SBFET with a channel length of L_{Si} = 5 µm at different drain bias V_D. The width and thickness of the Si channel are 2.5 µm and 110 nm, respectively.

The Al-Si-Al SBFET shows bipolar behavior, however with a higher current for negative gate voltages. For the symmetric device the minimum drain current I_D is observed at a back-gate voltage of V_{BG} = 0 V. Compared to the transfer characteristics of the Al-Ge-Al SBFET, the Al-Si-Al SBFET apparently exhibits a higher on/off ratio of ~10^4. This is notably about 685 nA at negative V_{BG} = -40 V and approximately 14 nA at V_{BG} = +40 V, when the drain voltage is set as V_D = 100 mV. The reason for the more symmetric behaviour and higher on/off ratio is due to the larger bandgap of Si and particularities in the Fermi level pinning. Whereas for Ge the fermi level pins close to the valence band, for Si the Fermi level pins at the middle of the bandgap (see **Figure 2.12**). Both these two physical phenomena can be explained via the investigation of gate-controlled effective barrier height, which will be discussed in the next section.

4.1.2.3 Effective Schottky barrier height of Al-Si-Al SBFET

To discuss the conduction mechanism in Al-Si-Al heterostructure devices in more detail, temperature-dependent transfer measurements were performed to extract the effective barrier height at various back-gate voltages. **Figure 4.29a** shows the transfer curves at different temperatures.

Die approbierte gedruckte Originalversion dieser Dissertation ist an der TU Wien Bibliothek verfügbar.
The approved original version of this doctoral thesis is available in print at TU Wien Bibliothek.
TU Bibliothek Your knowledge hub WIEN

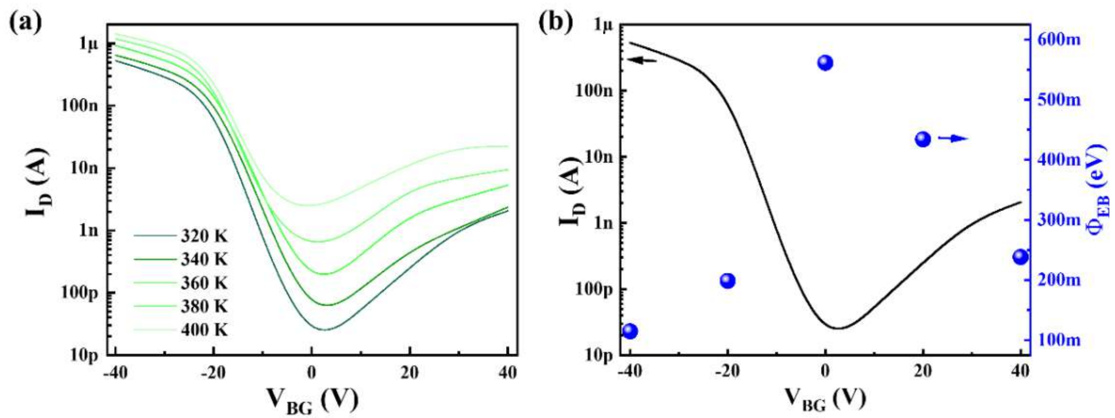

Figure 4.29 (a) Temperature-dependent transfer characteristics of an Al-Si-Al SBFET with a channel length of L_{Si} = 5 μm. The drain bias is V_D = 100 mV. (b) The derived effective barrier height Φ_{EB} at various back-gate voltages and transfer curve measured at room temperature and V_D = 100 mV.

The effective Schottky barrier height at different back-gate voltages was calculated using the Richardson method (see **Chapter 3.2.3**). **Figure 4.29b** shows the comparison of drain current I_D and the effective Schottky barrier height Φ_{EB} as the function of the back-gate voltage. Apparently, the larger effective barrier height Φ_{EB} results in a lower drain current I_D, in agreement with the thermionic emission theory (see **Eq. 3.1** in **Chapter 3.2.3**). At the back-gate voltage of V_{BG} = 0 V the highest effective barrier height of Φ_{EB} = 0.55 eV appears, which is almost half of the Si bandgap (i.e. E_g = 1.12 eV), indicating the Fermi level pinning about mid-gap. Furthermore, at the back-gate voltage of V_{BG} = +40 V and -40 V, the effective barrier height Φ_{EB} becomes 0.25 eV and 0.12 eV, respectively, indicating more symmetric barriers for electrons and holes, compared to that of Al-Ge-Al heterostructures.

TU Bibliothek – Die approbierte gedruckte Originalversion dieser Dissertation ist an der TU Wien Bibliothek verfügbar. The approved original version of this doctoral thesis is available in print at TU Wien Bibliothek.

4.2.3 Plasmonic applications of Al-Si-Al heterostructure devices

4.2.3.1 Switchable hot-carrier photodetection based on Al-Si-Al SBFET

Understanding the fundamental mechanism of hot carrier injection at metal/semiconductor interfaces is crucial for promoting the development of switchable hot-carrier photodetectors. As the Fermi level of the Al-Si-Al heterostructure device pins near mid-gap, the device is employed to investigate the principle for hot electron and hot hole injection. **Figure 4.30** shows the schematic of the Al-Si-Al heterostructure device enabling hot-carrier photodetection.

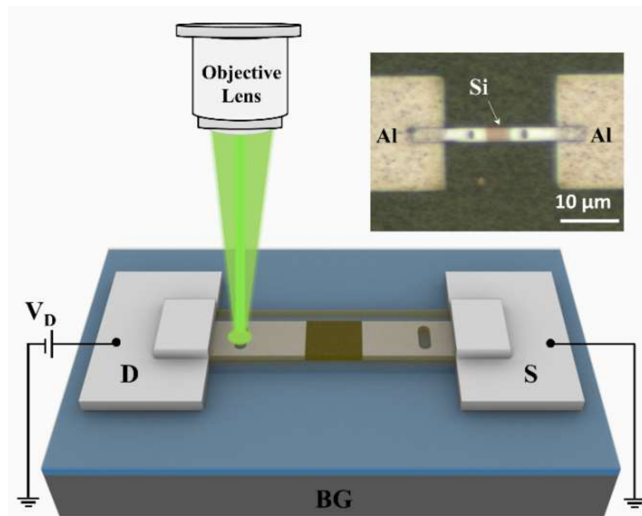

Figure 4.30 Schematic illustration of an Al-Si-Al SBFET with laser irradiation on the plasmon coupler. The right-upper inset shows the optical image of the Al-Si-Al heterostructure device with the oval trenches as plasmon couplers.

A SOI wafer comprising a 110 nm thick p-type Si device layer atop of the 385 nm thick BOX is adopted to fabricate the devices as shown in **Chapter 3.1**. The Al-Si-Al heterostructure micro-ribbons on top of the BOX resembles a back-gated SBFET with the BOX, and the doped Si handle wafer representing the gate insulator, and the back-gate electrode, respectively. Additionally, the oval-shaped trenches on the Al feed lines serve as the plasmonic couplers, which will generate SPPs under laser irradiation. The working principle of the Al-Si-Al SBFET as the SPP-induced hot-carrier detection system will be discussed with **Figure 4.31**.

Die approbierte gedruckte Originalversion dieser Dissertation ist an der TU Wien Bibliothek verfügbar.
The approved original version of this doctoral thesis is available in print at TU Wien Bibliothek.
TU Bibliothek Your knowledge hub WIEN

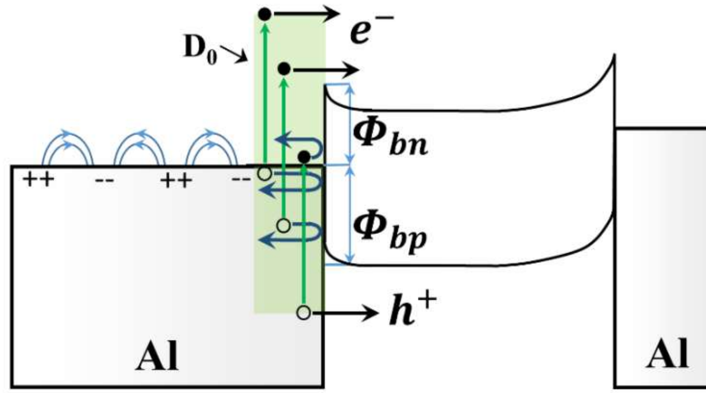

Figure 4.31 Hot-carrier photodetection based on the Al-Si-Al heterostructure, due to non-radiative decay of SPPs at the Al-Si interface and the injection of hot carriers to the Si segment. The effective barrier height for electrons and holes refers to as Φ_{bn} and Φ_{bp}, respectively. For Al, the energy distribution D_0 of hot carriers induced by the non-radiative decay of SPPs is homogeneous [97].

Optical diffraction gratings are usually implemented to excite SPPs due to the requirement of momentum conservation, here realized by a simple oval trench in the Al feed lines. Thus generated SPPs propagate towards the metal/semiconductor interface, and non-radiative decay at the Al/Si interface results in hot carriers. The corresponding energy distribution of thus generated hot charge carriers is determined by the electronic structure and density of states of the SPP waveguiding material. For the noble metals, such as gold (Au), and silver (Ag), metallic nanostructures under radiation yield hot carriers above (electrons) and below (holes) the metal Fermi level via either phonon-assisted transitions or direct interband transitions[65]. According to *ab-initio* calculations[98], in contrast to the bimodal distribution for noble metals, Al performs a relatively homogeneous distribution D_0 of both electrons and holes with respect to energy. Only those hot electrons with sufficient energy to surpass the effective barrier given by Φ_{bn} are injected into the Si channel and be collected by the opposite Al feed line. For hot holes, the energy must be correspondingly greater than Φ_{bp}.

Figure 4.32 shows the selectivity of capturing SPP-induced hot electrons and holes in a planar Al-Si-Al heterostructure device as a function of the back gate voltage.

Die approbierte gedruckte Originalversion dieser Dissertation ist an der TU Wien Bibliothek verfügbar.
The approved original version of this doctoral thesis is available in print at TU Wien Bibliothek.
TU WIEN Bibliothek Your knowledge hub

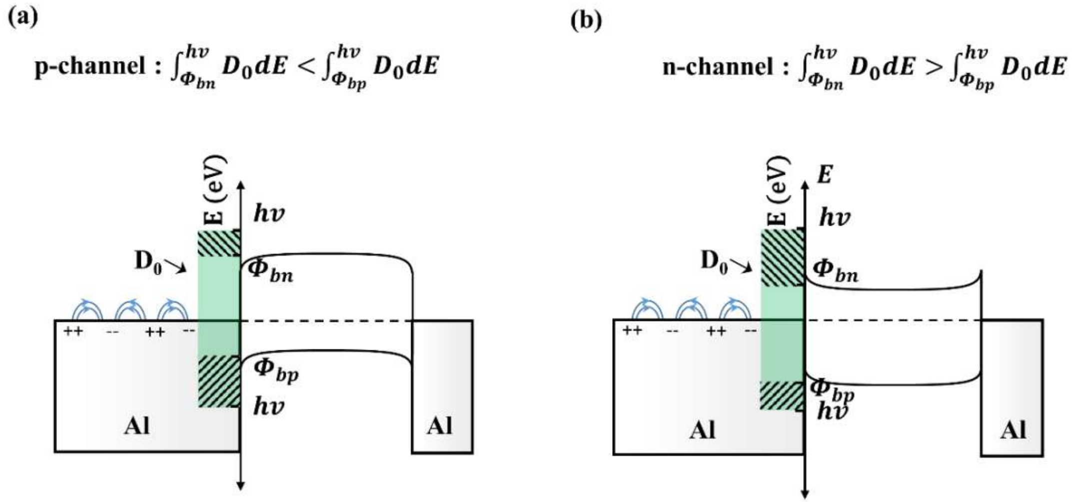

Figure 4.32 Schematic illustration of hole (a) and electron (b) injection at the negative and positive back-gate voltages, respectively. The injected hot electrons and holes can be derived as $\int_{\Phi_{bn}}^{h\nu} D_0\, dE$ and $\int_{\Phi_{bp}}^{h\nu} D_0\, dE$, as indicated with the shaded regions.

The effective barrier can thus serve as an energy filter, allowing both hot electrons and hot holes to be injected when the plasmon trench is irradiated with a 532 nm laser, as the bandgap of Si is much lower than the maximum plasmon energy $h\nu$. The net plasmon current should thus be equal to the difference between the two currents assigned to hot electrons and hot holes ($|I_{net}| = \left|\int_{\Phi_{bn}}^{h\nu} D_0 dE - \int_{\Phi_{bp}}^{h\nu} D_0 dE\right|$, where D_0 is the excited carrier distribution in Al). With the adjustment of the back gate voltage, the Fermi level E_F changes resulting in the modification of the effective barrier and consequently the barriers Φ_{bn} and Φ_{bp} for hot carrier injection. For positive back gate voltages, the effective barrier for electron injection is lowered. Due to the homogeneous distribution of hot carriers in Al[98], the lower barrier height for electrons prefers electrons injection (i.e. $\int_{\Phi_{bn}}^{h\nu} D_0 dE > \int_{\Phi_{bp}}^{h\nu} D_0 dE$), resulting in a net positive plasmon current. However, it completely contrasts for negative gate voltages with the larger barrier height for holes ($\Phi_{bn} > \Phi_{bp}$), enabling a net negative plasmon current, due to preferred holes injection.

The SPP-induced hot-carrier photodetection characteristics is demonstrated when one plasmonic trench is irradiated by a 532 nm laser in the power of 500 µW. **Figure 4.33a** demonstrates a comparison of the I/V characteristics in dark and under irradiation at the back-gate voltage of $V_{BG} = 0$.

Die approbierte gedruckte Originalversion dieser Dissertation ist an der TU Wien Bibliothek verfügbar.
The approved original version of this doctoral thesis is available in print at TU Wien Bibliothek.
TU Bibliothek Your knowledge hub WIEN

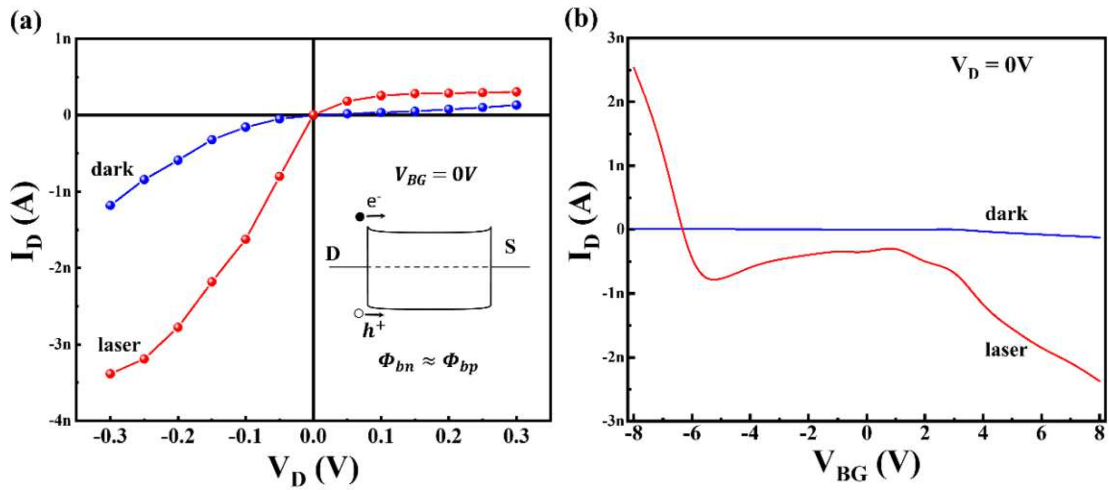

Figure 4.33 (a) I/V curves of Al-Si-Al SBFET measured in the dark (blue) and under the irradiation (red) on the plasmon coupler at V_{BG} = 0 V. The 532-nm laser beam is applied with a light power of 500 μW. The inset indicates the band diagram of Al-Si-Al heterostructure device at V_{BG} = 0 V and V_D = 0 V. (b) The transfer curves at the drain voltage of V_D = 0 V in dark (blue) and under green laser irradiation (red).

A typical I/V characteristic of the MSM device in the dark and V_{BG} = 0 V is illustrated in Figure **4.33a** (blue curve). Under the irradiation of the plasmon coupler, a significant difference appears between two I/V curves in **Figure 4.33a**. Here, the observed additional current refers to as plasmon current.

It is worthwhile to mention the reason of zero plasmon current under irradiation is not due to the lack of an external bias. Because the SPP-induced hot carriers can be injected into the Si channel and further diffuse to the opposite electrode, resulting in the generation of plasmon current. The actual origination is illustrated in the inset of **Figure 4.33a**. At zero back gate voltage and drain bias, the effective barrier for hot electrons and hot holes are approximately the same, thereby allowing the almost same number of electrons as holes to be injected. In other words, at V_D = 0 V plasmon current induced by hot electrons is compensated by that originated from hot holes. This is thus a direct experimental evidence for the theoretically predicted symmetrical distribution of hot charge carriers arising during the non-radiative decay of SPPs in Al[98].

This symmetry regarding the equal injection of hot electrons and holes can be broken via the back gate voltage, as modulation of effective barrier heights by the back gate can alter the injection number of hot electrons and hot holes, which has been discussed before (See **Figure 4.32**). Figure **4.33b** illustrates the modulated current at different back gate voltage in dark and

Die approbierte gedruckte Originalversion dieser Dissertation ist an der TU Wien Bibliothek verfügbar.
The approved original version of this doctoral thesis is available in print at TU Wien Bibliothek.
TU Bibliothek WIEN Your knowledge hub

under laser irradiation on the plasmon coupler. At V_{BG} = -8 V, it produces a positive plasmon current of about I_{PL} = 2.2 nA, due to predominant injection of hot holes. Conversely, at V_{BG} = 8 V the excess injection of electrons induces an opposite plasmon current of I_{PL} = -2.2 nA. Around V_{BG} = 0 V where approximately the same number of electrons and holes are injected, there should be zero plasmon current. However, a slightly negative current is observed, as in the Si segement the mobility and lifetime of holes is shorter than those of electrons.

The scanning photocurrent microscopy technique is implemented to analyze the electronic band structure of the gated Si channel. In this measurement, the Al-Si-Al heterostructure is irradiated by a diffraction-limited laser spot at the wavelength of 532 nm and a beam diameter of ~800 nm while the device photocurrent is recorded as a function of the local position of the laser spot. **Figure 4.34a** shows the scanning photocurrent mapping of the Al-Si-Al SBFET at various back-gate voltages V_{BG} and a drain voltage of V_D = 0V.

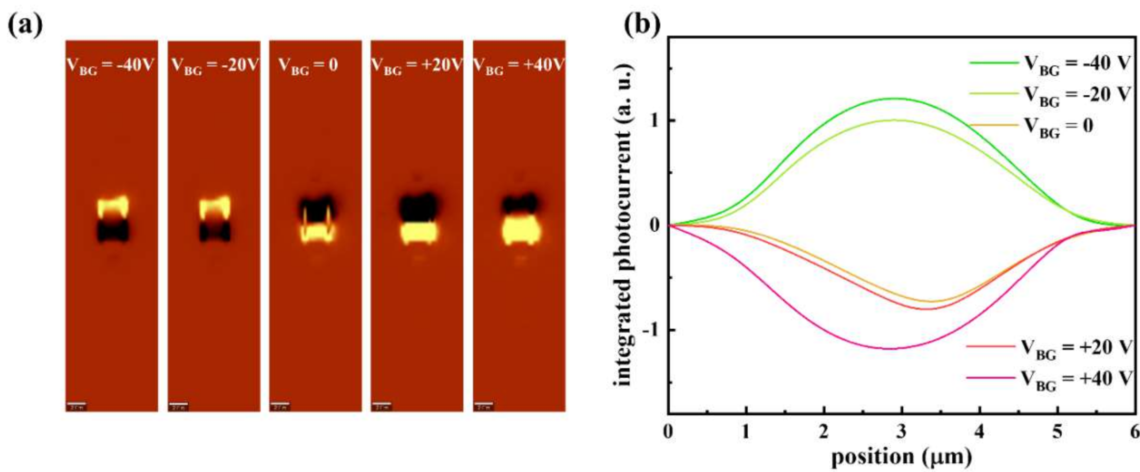

Figure 4.34 (a) Scanning photocurrent maps of the Al-Ge-Al SBFET under various back-gate voltages. The laser wavelength, light power and drain voltage are 532 nm, 500 μW and V_{DS} = 0 V, respectively. (b) The corresponding electrostatic potential under various back gate voltages.

At the back-gate voltage of V_{BG} = -40 V, the largest photocurrent appears near the two Al-Si interfaces. It indicates the existence of the Schottky junction providing a depletion region with a strong build-in electric field near the interface. A pronounced polarity switching behavior shows up when the laser spot moves from the source towards the drain, in agreement with the back-to-back biased Schottky barriers. Besides, photocurrent gradually declines while the corresponding position moves farther away from the interface, demonstrating the limited width

Die approbierte gedruckte Originalversion dieser Dissertation ist an der TU Wien Bibliothek verfügbar.
The approved original version of this doctoral thesis is available in print at TU Wien Bibliothek.
TU WIEN Bibliothek Your knowledge hub

of the depletion region. Therefore, the transport dynamics of photo-generated carriers at zero drain bias and the back-gate voltage of V_{BG} = -40 V can be described as follows: when the laser spot illuminates the Al/Si interface close to the drain electrode, it induces photo-generated electrons and holes. The electrons are accelerated toward the drain electrode, due to the build-in electric field in the depletion region, thereby enabling a positive photocurrent.

Not surprisingly, while the back-gate voltage is adjusted to 40 V, a distinct polarity switching behavior shows up, due to the changed direction of the build-in electric field.

The effective electrostatic potential E_{eff} (See **Figure 4.34b**) can be derived via the spatial integral of the photocurrent [119], given by

$$E_{eff} \propto \int I_{ph}(x)dx \tag{4.24}$$

When the back-gate voltage V_{BG} increases from -40 V to +40 V, the bending of the effective electrostatic potential-position curve switches from downward to upward presenting the same change of the electronic band.

Die approbierte gedruckte Originalversion dieser Dissertation ist an der TU Wien Bibliothek verfügbar.
The approved original version of this doctoral thesis is available in print at TU Wien Bibliothek.
TU WIEN Bibliothek Your knowledge hub

4.2.3.2 Plasmonic photovoltaics for Al-Si-Al SBFET

The possibility to filter plasmon generated charge carriers enables the exploration of a plasmonic on-chip energy harvester based on the Al-Si-Al heterostructures. **Figure 4.35** illustrates the Al-Si-Al heterostructure device in the split-gate configuration.

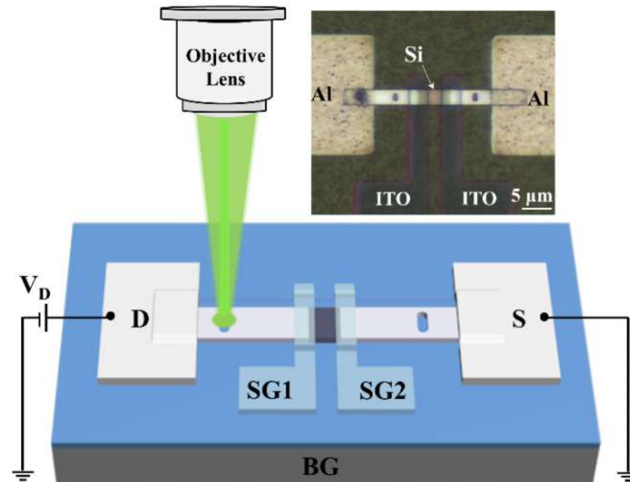

Figure 4.35 Schematic diagram of the Al-Si-Al heterostructure device with two split gates. The source, drain, the left split gate, and the second split gate are denoted as S, D, SG1, and SG2, respectively. The inset illustrates the corresponding optical image.

Such a split-gate Al-Si-Al SBFET is resembled with two ITO gates directly atop of the Al-Si interfaces. The other components are similar to that of the back-gate Al-Si-Al SBFET mentioned before (see **Chapter 4.2.3.1**). The SPCM measurements are carried out to verify the band bending for different split-gate voltages (see **Figure 4.36**). **Figure 4.36a** shows the optical image of the Al-Si-Al heterostructure the Al-Si-Al heterostructure with ITO split gates atop the two Al/Si interfaces. **Figure 4.36b** and **c** illustrate the respective photocurrent maps for various split-gate voltages. Like the back-gate Al-Si-Al SBFET, the device exhibits n-type behaviour if both split-gate voltages are positive (see the lower-right inset in **Figure 4.36d**).

Die approbierte gedruckte Originalversion dieser Dissertation ist an der TU Wien Bibliothek verfügbar.
The approved original version of this doctoral thesis is available in print at TU Wien Bibliothek.
TU Bibliothek WIEN Your knowledge hub

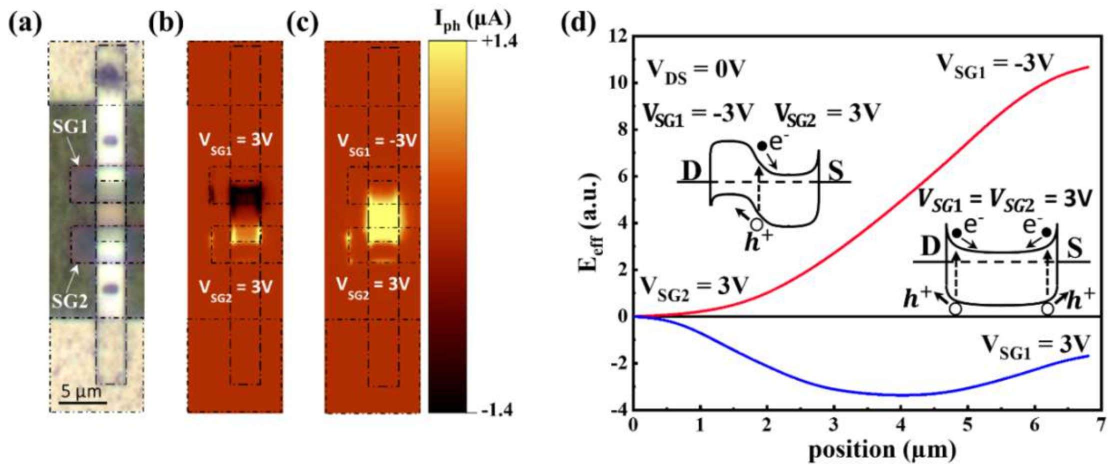

Figure 4.36 Optical image (a) and photocurrent images for the unbiased Al-Si-Al SBFET with (b) both split gates at V_{SG1} = V_{SG2} =3 V and (c) split gates with opposite polarity of V_{SG1} = 3 V and V_{SG2} = -3 V. (d) Plot of effective electrostatic potential E_{eff} along the Si channel of the SBFET for equal and opposite poled split gates and the respective band structures and charge separation mechanisms in the insets.

Again the largest photocurrent apparently shows up near the gated Al-Si junction. If the contact region is irradiated, photogenerated electrons and holes are accelerated by the strong build-in electric field provided by the Schottky contact, consequently generating the largest photocurrent. But for opposite polarities at the split gates (V_{SG1} = -3 V and V_{SG2} = 3 V), a significant photocurrent appears if the irradiation is located in the middle of the device. It should be attributed to a build-in electric field of the virtual p-n junction (see the upper-left inset in **Figure 4.36d**), which is formed for opposite biases of split gates. **Eq. 4.24** is employed again to calculate the effective electrostatic potential E_{eff}. **Figure 4.36d** illustrates the built-in electric field with the virtual p-n junction, corresponding to opposite polarity split gates (V_{SG1} = -3 V and V_{SG2} = 3 V). The rectifying performance of the I/V characteristic in dark (see blue curve in **Figure 4.37**) is another proof for forming the virtual p-n junction in the Si channel.

Die approbierte gedruckte Originalversion dieser Dissertation ist an der TU Wien Bibliothek verfügbar.
The approved original version of this doctoral thesis is available in print at TU Wien Bibliothek.
TU Wien Bibliothek Your knowledge hub

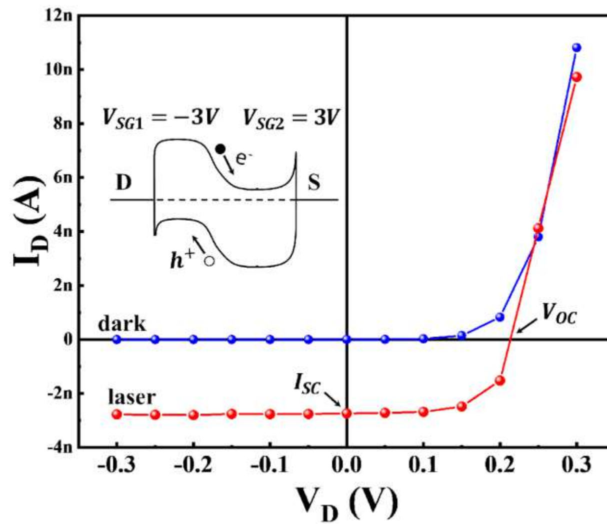

Figure 4.37 I/V curves measured in dark (blue) and under irradiation (red) of the plasmonic coupler at split-gate voltages of V_{SG1} = -3 V and V_{SG2} = 3 V. The laser wavelength and power are 532 nm and 500 µW, respectively. The inset shows the corresponding band diagram at the drain bias of V_D = 0 V.

When the plasmon coupler is irradiated, the resulting I/V curve remains the similar shape like the one tested in dark, but shifts downward due to the generation of plasmon current. The hot carriers originating from the non-radiative decay of SPPs can surmount the Al/Si Schottky barrier if their energy is sufficient enough. Subsequently they are separated inside the virtual p-n junction and get collected by the Al electrodes. Like for a conventional solar cell, the parameters named the short-circuit current I_{sc} and the open-circuit voltage V_{oc} are extracted from the I/V characteristic measured under irradiation (see the red curve in **Figure 4.37**). In the short-circuit state, the plasmonic solar cell can provide the short-circuit current of I_{sc} = -2.7 nA flowing through the external circuit. In the ideal case, the short-circuit current should be equal to the plasmon current induced by hot-carrier injection. In the open-circuit state, no current flows through the external circuit, meaning that the plasmon current is compensated by the dark current. In this case the plasmonic solar cell provides an open-circuit voltage of V_{oc} = 0.2 V.

The open-circuit voltage V_{oc} can be modulated by the applied split-gate voltages. **Figure 4.38a** shows the open-circuit voltage V_{oc} under different split gate voltages and **Figure 4.38b** illustrates the respective band structure diagrams corresponding to some selected combinations thereof.

Die approbierte gedruckte Originalversion dieser Dissertation ist an der TU Wien Bibliothek verfügbar.
The approved original version of this doctoral thesis is available in print at TU Wien Bibliothek.
TU WIEN Bibliothek Your knowledge hub

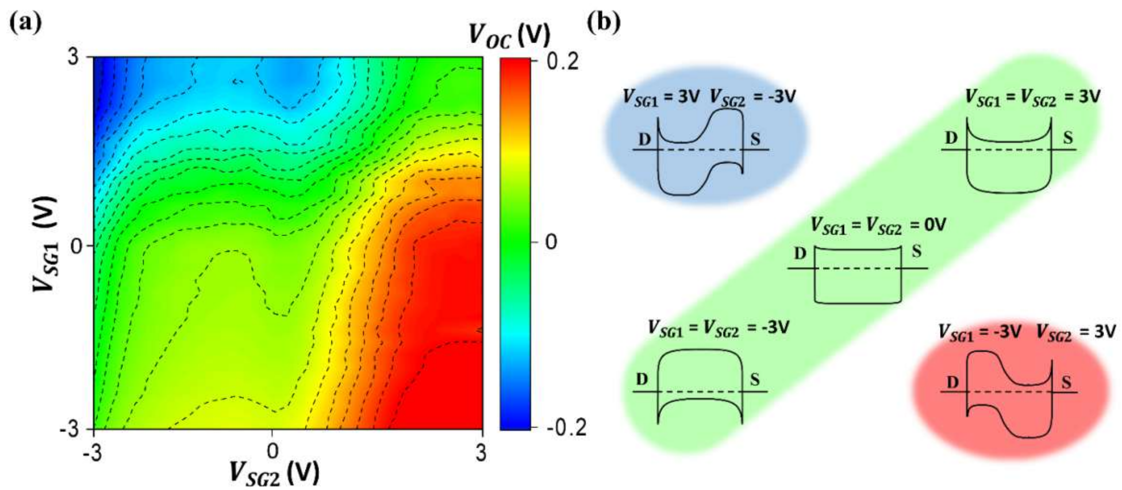

Figure 4.38 (a) The detailed maps of open-circuit voltage V_{oc} under different split-gate voltages. The irradiation power and the drain bias are 500 μW and 0 V, respectively. (b) Five typical band diagrams induced by different split-gate voltages.

In contrast to electronic impurity doping, the gate-bias-induced virtual doping apparently exhibits a more versatile and convenient modulation on the polarity and concentration of charge carriers. Compared to the split-gate voltage combination (V_{SG1} = -3 V and V_{SG2} = 3 V, the opposite combination (V_{SG1} = 3 V and V_{SG2} = -3 V) can reverse the polarity of the p-n junction and thereof the polarity of V_{oc} as well (see **Figure 4.38a**).

If a symmetric split-gate voltage of 3 V is applied on both split gates, the Al-Si-Al heterostructure SBFET performs n-type behaviour (see **Figure 4.38b**). In contrast, a p-type behaviour appears if both split gates are negatively biased (V_{SG1} = V_{SG2} = -3 V) [120,121]. In these cases, no virtual p-n junction is formed, thereby resulting in a zero V_{oc}.

TU WIEN Bibliothek Your knowledge hub
Die approbierte gedruckte Originalversion dieser Dissertation ist an der TU Wien Bibliothek verfügbar.
The approved original version of this doctoral thesis is available in print at TU Wien Bibliothek.

Die approbierte gedruckte Originalversion dieser Dissertation ist an der TU Wien Bibliothek verfügbar.
The approved original version of this doctoral thesis is available in print at TU Wien Bibliothek.
TU WIEN Bibliothek Your knowledge hub

Chapter 5

Summary and outlook

A systematic and fundamental study on CMOS-compatible on-chip plasmon detection systems is presented. The devices comprising a plasmon antenna, plasmon waveguide and a hot-carrier detection component are assembled by a monolithic Al-Ge-Al or Al-Si-Al heterostructure based on GeOI and SOI wafers, respectively. The self-aligned fabrication process is based on a thermally induced exchange reaction between Ge (or Si) and Al pads, enabling on-chip plasmon detection system without lithographic restrictions. To investigate the fundamental dynamics of hot carriers arising from the non-radiative decay of SPPs at the metal-semiconductor interface, electrostatically gated device architectures are realized.

As the generation of hot carriers by Landau damping or chemical interface damping of surface plasmons is of particular interest to the fundamental aspects of extreme light-matter interactions as well as for potential practical applications, a profound introduction of background knowledge in terms of hot-carrier photodetection from the material level to the device level is elaborated in the theory chapter. Further, the basics of plasmon generation and guiding, as well as the working principle of hot-carrier detection devices are introduced.

In the chapter regarding the experimental techniques, the fabrication process of hot-carrier photodetection devices is discussed, including Al-Ge-Al heterostructure and Al-Si-Al heterostructure SBFETs in different electrostatically gated configuration (i.e. back-gate or top split-gate architecture). Subsequently, the measurement setups for electrical and optoelectronic characterization are discussed in detail. Some special techniques, like temperature-dependent electrical measurements, the scanning photocurrent microscopy and the modified pump-probe cross-correlation technique, are introduced as effective characterization methods for sophisticated nanophotonic studies.

In the final chapter results and discussion, firstly the Al-Ge-Al heterostructure based devics are discussed. In particular, some phenomena with respect to the dynamics of hot carriers are explored, like negative photoconductivity and a photodetection scheme exhibiting superlinear current-power law. Additionally, a modified pump-probe cross-correlation technique is utilized to measure the response time of the plasmon detection system, demonstrating an ultra-fast response of around 50 GHz realized by a compact Al-Ge-Al heterostructure SBFETs with a

TU Bibliothek Your knowledge hub WIEN
Die approbierte gedruckte Originalversion dieser Dissertation ist an der TU Wien Bibliothek verfügbar.
The approved original version of this doctoral thesis is available in print at TU Wien Bibliothek.

channel length of less than 100 nm. Afterwards, using devices based on Al-Si-Al heterostructures the selective injection of hot carriers is demonstrated with significant potential for implementing for on-chip photovoltaics.

Further, the main findings for Al-Ge-Al and Al-Si-Al based plasmonic devices are as follows

- Light absorption, surface plasmon polariton generation and effective separation of hot charge carriers arising from the non-radiative decay of surface plasmon polariton is realized in monolithic Schottky barrier field effect transistors.
- The monolithic Al leads perform a dual function and simultaneously carry both optical and electrical signals, giving rise to exciting new capabilities.
- Via electrostatic modulation of the effective barrier height of the Schottky junctions, the transfer of hot charge carriers arising from the non-radiative decay of SPP can be tuned with respect to their energy and polarity. Thus generated hot carriers with sufficient energy to surpass the effective Schottky barrier are injected into the semiconductor channel and generate a detectable current. For these excited carriers the momentum must be in the direction towards the metal-semiconductor junction, so that the carrier's kinetic energy component in that direction is sufficient to overcome the Schottky barrier. The difficulty of achieving both energy and momentum matching is in general a main cause of the low quantum efficiency for extracting excited carriers in plasmonic devices. The actual monolithic device architecture is ideal in view of this as the SPPs are directly guided towards the metal-semiconductor interface.
- As a direct consequence of the monolithic architecture and thus improved momentum matching the devices have proven to be extremely effective plasmon detectors with an external quantum efficiency of EQE = 2.5%. Although no optimization with respect to effective plasmon coupling or SPP waveguiding has been done yet, this is quite remarkable since for other electrical plasmon detectors EQEs of less than 1% have been reported.
- Aside of barrier modulation, split gates can emulate a virtual p-n junction in the Si channel, making the plasmonic Al-Si-Al device working as a solar cell. The realized transparent gate stack enables further to investigate the electrical potential in the device. Combined with electrical measurements this reveals the mechanisms of excited charge carrier transfer during the non-radiative decay of SPPs at the metal-semiconductor junction.

Die approbierte gedruckte Originalversion dieser Dissertation ist an der TU Wien Bibliothek verfügbar.
The approved original version of this doctoral thesis is available in print at TU Wien Bibliothek.
TU WIEN Bibliothek Your knowledge hub

- A planar Al-Ge-Al photo-responsive heterostructure device with monolithic Al source/drain contacts equipped with a plasmon coupler is experimentally demonstrated. The deep-sub-micrometer scaled Ge channel comprises in effect a hot-carrier photodetector with a ballistic carrier transport. The demonstrator detector tested with 1560 nm light revealed a bandwidth around 50 GHz. Due to the nature of the electric signal generation, the detector features a responsivity of 0.35 mA/W at 1560 nm at notably zero bias.

Most notably, the standard top-down fabrication combined with a novel post-annealing method surmounts the size limit of lithography, enabling ultra-short Ge or Si channels, thus demonstrating the promising potential in the large-scale integration based on GeOI or SOI wafers. This thesis illustrates negative photoconductivity and selective injection of hot electrons/holes, both of which can provide the state for building plasmonic logic gates and further plasmonic logic circuits. In addition, the virtual p-n junction realized by the split-gate configuration shows possible application for CMOS-compatible plasmonic photovoltaics, which may have the capability of offering energy for on-chip autonomous nanosystems. Furthermore, SPP-induced hot carrier trapping likely enables plasmon-stimulated synaptic transistors for an on-chip neuromorphic platform in the future. Last but not least, the monolithic ultra-scaled and high-speed detectors have already been demonstrated in prototypes for future plasmonic interconnects. Nevertheless, a working on-chip plasmonic plateform still requires an effective plasmon source which have been realized recently using a metal-insulator-metal tunneling junction[122]. such a technology of an electrically pumped plasmon source could also be monolithically integrated into the existing process and would therefore complete the combined electrical-plasmonic plateform for future practical applications.

TU Bibliothek Your knowledge hub
Die approbierte gedruckte Originalversion dieser Dissertation ist an der TU Wien Bibliothek verfügbar.
The approved original version of this doctoral thesis is available in print at TU Wien Bibliothek.

Die approbierte gedruckte Originalversion dieser Dissertation ist an der TU Wien Bibliothek verfügbar.
The approved original version of this doctoral thesis is available in print at TU Wien Bibliothek.
TU WIEN Bibliothek Your knowledge hub

Curriculum Vitae

Zehao Song, MSc

Born: Sep 14th, 1994, in Wuhan (China)

E-mail: zehao.song@tuwien.ac.at

Phone: +43 6767004095

Address: Donaufelder Str. 54, 1210 Wien

Education

PhD candidate of Science in *Electrical Engineering*

2019 – Present

Institute of Solid State Electronics, Vienna University of Technology

Supervisor: ***Associate Professor Alois Lugstein***

Master of Science in *Electronic Science and Technology*

2016 – 2019

Faculty of Physics & Electronic Science, Hubei University

Supervisor: ***Professor Hai Zhou***

Bachelor of Science in *Microelectronics*

2012 – 2016

Faculty of Physics & Electronic Science, Hubei University

Die approbierte gedruckte Originalversion dieser Dissertation ist an der TU Wien Bibliothek verfügbar.
The approved original version of this doctoral thesis is available in print at TU Wien Bibliothek.
TU WIEN Bibliothek Your knowledge hub

Journal paper

- ***Z. Song***, *L. Wind, M. Sistani, F. Schwingshandl, A. Lugstein. Plasmon Stimulated Synaptic Transistor.* ***ACS Nano. (Submitted)***
- *Z. Song#, J. Darmo#, M. Sistani, L. Wind, D. Theiner, A. Lugstein. Ultra-High Speed Hot-Carrier Photodetection in Monolithic Al-Ge-Al Heterostructure Devices.* ***ACS Photonics. (Submitted)***
- ***Z. Song***, *M. Sistani, F. Schwingshandl, A. Lugstein. Controlling Hot Charge Carrier Transfer in Monolithic Al-Si-Al Heterostructures for Plasmonic On-Chip Energy Harvesting.* ***Small***, *2023, 2301055.*
- ***Z. Song***#, *M. Sistani#, L. Wind, D. Pohl, B. Ellingham, W. M. Weber, A. Lugstein. Plasmon-assisted polarization-sensitive photodetection with tunable polarity for integrated silicon photonic communication systems.* ***Nanotechnology***, *2021, 32, 50.* ***(as co-first author)***
- *C. Wang#,* ***Z. Song***#, *P. Shi, L. Lev, H. Wan, T. Li, J. Zhang, H. Wang, H. Wang. High-rate transition metal-based cathode materials for battery-supercapacitor hybrid devices.* ***Nanoscale Advances***, *2021, 3(18), 5222-5239.* ***(as co-first author)***
- *D. Wu, H. Zhou,* ***Z. Song***, *M. Zheng, R. Liu, X. Pan, H. Wan, J. Zhang, H. Wang, X. Li, H. Zeng. Welding perovskite nanowires for stable, sensitive, flexible photodetectors.* ***ACS Nano***, *2020, 14, 3, 2777-2787.*
- *P. Gui, H. Zhou, F. Yao,* ***Z. Song***, *B. Li, G. Fang. Space confined growth of individual wide bandgap single crystal $CsPbCl_3$ microplatelet for near ultraviolet photodetection.* ***Small***, *2019, 15, 39, 1902618.*
- ***Z. Song***, *H. Zhou, P. Gui, X. Yang, R. Liu, G. Ma, H. Wang, G. Fang. All-inorganic perovskite $CsPbBr_3$-based self-powered light-emitting photodetectors with ZnO hollow balls as an ultraviolet response center.* ***Journal of Materials Chemistry C***, *2018, 6, 5113-5121.*
- *Y. Zhu#,* ***Z. Song***#, *H. Zhou, D. Wu, R. Lu, R. Wang, H. Wang. Self-powered, broadband perovskite photodetector based on ZnO microspheres as scaffold Layer.* ***Applied Surface Science***, *2018, 448, 23-29.* ***(as co-first author)***
- ***Z. Song***, *H. Zhou, C. Ye, L. Yang, M. Xue, J. Mei, H. Wang. Surface treatment for*

Die approbierte gedruckte Originalversion dieser Dissertation ist an der TU Wien Bibliothek verfügbar.
The approved original version of this doctoral thesis is available in print at TU Wien Bibliothek.
TU Bibliothek Your knowledge hub WIEN

Schottky barrier photodetector based on Au/GaZnO nanorods/Au structure. ***Materials Science in Semiconductor Processing**, 2017, 64, 101-108.*

- ***Z. Song**, H. Zhou, P. Tao, B. Wang, J. Mei, H. Wang, S. Wen, Z. Song, G. Fang. The synthesis of TiO_2, nanoflowers and their application in electron field emission and self-powered ultraviolet photodetector.* ***Materials Letters**, 2016, 180, 179-183.*

Patent

- *H. Wang, H. Zhou, G. Ma,* ***Z. Song**. Hubei University, 2020. Preparation method and application of light-responsive LED based on GaN/$CsPbBr_xI_{3-x}$ heterojunction.* ***U.S. Patent** 10,749,065.*

Conference talk

- ***Z. Song**, M. Sistani, L. Wind, A. Lugstein, "CMOS-compatible Nanometre-Scale Germanium Photodetector with Tunable-Polarity Sensitivity",* ***EUROMAT** 2021, Virtual;*
- ***Z. Song**, A. Lugstein, "Selective Capture of Hot Electrons/Holes for Plasmon Decay at an Atomically Sharp Metal-Semiconductor Interface",* ***MRS** 2022, Boston.*

Die approbierte gedruckte Originalversion dieser Dissertation ist an der TU Wien Bibliothek verfügbar.
The approved original version of this doctoral thesis is available in print at TU Wien Bibliothek.
TU WIEN Bibliothek Your knowledge hub

TU WIEN Bibliothek Your knowledge hub
Die approbierte gedruckte Originalversion dieser Dissertation ist an der TU Wien Bibliothek verfügbar.
The approved original version of this doctoral thesis is available in print at TU Wien Bibliothek.

List of figures

Figure 1.1 The number of transistors in one microprocessor from 1970 to 2020. 1

Figure 1.2 Scanning electron microscopy images showing (a) the cross-sectional and (b) global view of modern ICs interconnect architecture. (c) Delay time determined by the feature size of interconnect metal wires for transistors. 2

Figure 1.3 The comparison of various interconnect methods with respect to device size and operating speed.. 3

Figure 1.4 Various plasmonic devices expanding the field of silicon technology. 4

Figure 1.5 Schematic of a monolithic plasmon device assembled by two plasmon trenches and Al-Semiconductor-Al heterostructure. 6

Figure 2.1 Schematic of the diamond cubic lattice structure of Si.. 10

Figure 2.2 (a) The first Brillouin zone of Si involving 14 faces. (b) One quadrant of the first Brillouin zone. 11

Figure 2.3 Band structure of Si with the band gap of E_g = 1.12 eV. 12

Figure 2.4 (a) Schematic of the Ge diamond lattice structure with the lattice constant of a_{Ge} = 0.566 nm. (b) Band structure demonstrates that Ge is an indirect band gap with E_g = 0.66 eV. 13

Figure 2.5 (a) Schematic diagram with respect to the surface traps of Ge. (b) A comparison of the density and detrapping time τ_t for fast and slow surface traps.. 14

Figure 2.6 (a) The primitive unit cell of Al crystallinity in the FCC lattice structure. (b) Band structure of Al. 15

Figure 2.7 Band diagrams of a metal, a semiconductor and an insulator.. 16

Figure 2.8 Schematic illustration of bandgap diagram, density of states, Fermi-Dirac distribution and carrier concentration for (a) intrinsic, (b) n-type, and (c) p-type semiconductor.. 19

Figure 2.9 (a) Space-charge distribution in p-type and n-type semiconductors with the doping concentration of N_A and N_D, respectively. (b) Electric-field distribution featuring a maximum at the interface (x = 0). (c) Potential distribution. (d) Energy-band diagram of the abrupt p-n junction in thermal equilibrium. 22

Figure 2.10 The I/V characteristic of an ideal p-n junction diode. 24

Figure 2.11 (a) Band diagrams of separated metal and n-type semiconductor. (b) Formation of the Schottky junction. 25

Die approbierte gedruckte Originalversion dieser Dissertation ist an der TU Wien Bibliothek verfügbar.
The approved original version of this doctoral thesis is available in print at TU Wien Bibliothek.
TU Bibliothek WIEN Your knowledge hub

Figure 2.12 (a) Fermi level pinning at mid-gap. (b) Material screening demonstrates that most metals result in strong Fermi level pinning at mid-gap for Si and near the valence band for Ge. 26
Figure 2.13 (a) Comparison of the typical I/V curve of a Schottky diode and a p-n junction diode. (b) Band diagram describing thermionic emission, thermionic-filed emission and Field emission. 27
Figure 2.14 Light absorption mechanism for (a) direct-bandgap semiconductor and (b) indirect-bandgap semiconductor.. 30
Figure 2.15 (a) Radiative recombination, resulting in the emission of photons or electrons via Auger recombination. (b) Non-radiative recombination through single-level traps. 31
Figure 2.16 (a) Schematic diagram demonstrating the excitation and propagation of SPPs at a metal/dielectric interface. (b) The dispersion relation.. 33
Figure 2.17 Various methods for exciting SPPs, including (a) Kretschmann geometry, (b) two-layer Kretschmann geometry, (c) Otto geometry, (d) excitation by a nearfield scanning optical microscopy probe, (e) diffraction on a grating, and (f) diffraction on a surface defect.. 35
Figure 2.18 (a) The intensity distribution of an SPP along a metal-dielectric interface. (b) The dispersion relations in different guiding modes in a metal waveguide. 37
Figure 2.19 The possible mechanisms for losses of SPPs while propagating along a metal waveguide.. 37
Figure 2.20 Radiative or non-radiative decay mechanisms of localized SPPs.. 38
Figure 2.21 Non-radiative decay mechanisms. 39
Figure 2.22 The permitted transitions in the band structure (see upper panels) for (a) aluminum, (b) silver, (c) copper and (d) gold. 40
Figure 2.23 Hot electrons transport through a metal-semiconductor-metal back-to-back Schottky diode. 44
Figure 2.24 The injection of hot electrons from the metal to the semiconductor requires momentum conservation.. 45
Figure 3.1 Schematic diagram shows the process flow for the fabrication of the Al-Si-Al heterostructure device. 48
Figure 3.2 Schematic diagram of the electrical measurement setup for current/voltage measurements of an Al-Ge-Al heterostructure device. 50
Figure 3.3 (a) I/V curves of one Al-Ge-Al heterostructure measured at various temperatures. (b) Richardson plots under different drain bias V_D. (c) Derived Schottky barrier height at different drain bias V_D. (d) Band diagram of back-to-back Schottky barrier diode. 52

Die approbierte gedruckte Originalversion dieser Dissertation ist an der TU Wien Bibliothek verfügbar.
The approved original version of this doctoral thesis is available in print at TU Wien Bibliothek.
TU Bibliothek Your knowledge hub WIEN

Figure 3.4 Schematic diagram of the scanning photocurrent measurement setup................. 54
Figure 3.5 Schematic diagram of the modified pump-probe cross-correlation setup............ 55
Figure 3.6 The working principle of pump-probe cross-correlation measurement. 56
Figure 3.7 The resolution limitation of the pump-probe setup.. 58
Figure 4.1 (a) SEM image of the initial Ge nanosheet with sputter-deposited Al pads and (b) the resulting heterostructure after annealing at 673 K for 5 min. 60
Figure 4.2 SEM images of Al-Ge-Al heterostructure device with different channel lengths L_{Ge}. 61
Figure 4.3 AFM topography plot showing the surface roughness of sputtered Al pad (a), exchanged Al feed line (b) and Ge segment (c). 62
Figure 4.4 (a) I/V curves of an Al-Ge-Al SBFET with a channel length of L_{Ge} = 0.6 µm measured at various back-gate voltages. (b) Band diagram of the Al-Ge-Al heterostructure device at the back-gate voltage of V_{BG} = 0 V.. 63
Figure 4.5 (a) I/V characteristics of Al-Ge-Al heterostructure devices with different channel lengths L_{Ge} measured at back-gate voltage of V_{BG} = 0V. (b) Resistance R of the Al-Ge-Al heterostructure as the function of channel length L_{Ge} at the back-gate voltage of V_{BG} = 0V. 64
Figure 4.6 Transfer characteristics of an Al-Ge-Al SBFET with a channel length of L_{Ge} = 0.6 µm measured at different drain bias V_D.. 65
Figure 4.7 Gate controlled effective barrier height Φ_{EB} for an Al-Ge-Al heterostructure SBFET with a channel length of L_{Ge} = 0.6 µm.. 66
Figure 4.8 Band diagram showing gate-controlled effective barrier height Φ_{EB} modulation for Al-Ge-Al heterostructure SBFETs. 66
Figure 4.9 (a) The measurement setup of the Al-Ge-Al heterostructure SBFET under laser irradiation. (b) The SEM image of an ultra-short Al-Ge-Al heterostructure with channel length of L_{Ge} = 200 nm. (c) The comparison of transfer characteristics of the Al-Ge-Al heterostructure transistor with a channel length of L_{Ge} = 200 nm in dark and under irradiation. (d) Wavelength-dependent photoconductance ΔG at a back gate voltage of V_{BG} = +40 V............................. 68
Figure 4.10 (a) Transfer characteristics of Ge SBFET with a channel length of L_{Ge} = 200 nm under different sweeping directions and sweeping rates. (b) Light intensity modulated transfer characteristics of the Al-Ge-Al heterostructure transistor with a channel length of L_{Ge} = 200 nm at a drain voltage of V_D = 10 mV. 69
Figure 4.11 Band diagrams applied to schematically explain PPC and NPC phenomena.. ... 71

Die approbierte gedruckte Originalversion dieser Dissertation ist an der TU Wien Bibliothek verfügbar.
The approved original version of this doctoral thesis is available in print at TU Wien Bibliothek.
TU Bibliothek WIEN Your knowledge hub

Figure 4.12 (a) Light intensity dependent photoconductance ΔG for two characteristic back-gate voltages of -50 V and +50 V. (b) The working mechanism related to the hot-carrier trapping model. 72

Figure 4.13 The impact of channel length on the polarity of the photoconductance ΔG at a gate voltage of V_{BG} = 50 V. 77

Figure 4.14 (a) Schematic of the setup for polarization-dependent measurement. (b) Polar plot of the photocurrent as a function of the polarization angle θ. (c) Photocurrent map as a function of the drain voltage V_D and polarization angle θ. 79

Figure 4.15 The layout of a plasmonic antenna-coupled Al-Ge-Al heterojunction used for plasmon-induced hot-carrier detector.. 81

Figure 4.16 Plasmon current I_{pl} as a function of the Ge channel length measured for the green (λ = 532 nm) and red (λ = 785 nm) laser excitation........82

Figure 4.17 Propagation length of SPPs on the monolithic Al feed line measured for the green the green (λ = 532 nm) and red (λ = 785 nm) laser excitation. 84

Figure 4.18 (a) The diagram schematically describes the working principles of plasmon-gating, including excitation of SPPs at the plasmon coupler, propagation of SPPs along the Al feed line, and hot carriers transport in the Ge channel. (b) The comparison of the transfer curves of the Al-Ge-Al heterostructure SBFET in dark and under irradiation of one plasmonic coupler with various light power. (c) Transient response to a laser pulse at $V_D = V_{BG}$ = 0 V........85

Figure 4.19 Plasmon current as a function of light power measured at various gate voltages V_{BG}. 87

Figure 4.20 Schematic illustration of non-radiative recombination models: (a) a common model containing only one recombination center; (b) the introduction of type II centers located above E_{Dn} does not affect the condition of (a); (c) when the location of type II centers becomes below E_{Dn}, these centers will become activators, sensitizing the photoconductor and increasing its photoconductivity. 88

Figure 4.21 Plasmon current I_{pl} as the function of light power under different drain bias. 90

Figure 4.22 (a) The layout of the Al-Ge-Al heterostructure transistor. (b) Transfer curves measured from Al-Ge-Al heterostructure transistors with various Ge channel lengths.. 91

Figure 4.23 Scanning photocurrent measurement of as the Al-Ge-Al SBFET with a Ge segment length of 1.3 µm........93

Figure 4.24 Spectral responsivity of Al-Ge-Al heterostructure photodetectors with various Ge channel lengths........94

Die approbierte gedruckte Originalversion dieser Dissertation ist an der TU Wien Bibliothek verfügbar.
The approved original version of this doctoral thesis is available in print at TU Wien Bibliothek.
TU WIEN Bibliothek Your knowledge hub

Figure 4.25 The impact of the Ge channel length on the pump-probe signal for SBFET devices with (a) $L_{Ge} = 2.4$ µm, (b) $L_{Ge} = 1.3$ µm and (c) the ballistic device ($L_{Ge} < 100$ nm).. 95
Figure 4.26 (a) The initial device with the Si nanosheet contacted by two sputtered Al pads. (b) The Al-Si-Al heterostructure after annealing at 773 K for 30 minutes.. 98
Figure 4.27 I/V characteristics of an Al-Si-Al SBFET with a channel length of $L_{Si} = 5$ µm for different back-gate voltages. 99
Figure 4.28 Transfer curves of an Al-Si-Al SBFET with a channel length of $L_{Si} = 5$ µm at different drain bias V_D. 100
Figure 4.29 (a) Temperature-dependent transfer characteristics of an Al-Si-Al SBFET with a channel length of $L_{Si} = 5$ µm. (b) The derived effective barrier height Φ_{EB} at various back-gate voltages and transfer curve measured at room temperature and $V_D = 100$ mV. 101
Figure 4.30 Schematic illustration of an Al-Si-Al SBFET with laser irradiation on the plasmon coupler. 102
Figure 4.31 Hot-carrier photodetection based on the Al-Si-Al heterostructure. 103
Figure 4.32 Schematic illustration of hole (a) and electron (b) injection at the negative and positive back-gate voltages, respectively.. 104
Figure 4.33 (a) I/V curves of Al-Si-Al SBFET measured in the dark (blue) and under the irradiation (red) on the plasmon coupler at $V_{BG} = 0$ V. (b) The transfer curves at the drain voltage of $V_D = 0$ V in dark (blue) and under green laser irradiation (red). 105
Figure 4.34 (a) Scanning photocurrent maps of the Al-Ge-Al SBFET under various back-gate voltages. (b) The corresponding electrostatic potential under various back gate voltages. .. 106
Figure 4.35 Schematic diagram of the Al-Si-Al heterostructure device with two split gates. 108
Figure 4.36 Optical image (a) and photocurrent images for the unbiased Al-Si-Al SBFET with (b) both split gates at $V_{SG1} = V_{SG2} = 3$ V and (c) split gates with opposite polarity of $V_{SG1} = 3$ V and $V_{SG2} = -3$ V. (d) Plot of effective electrostatic potential E_{eff} along the Si channel of the SBFET 109
Figure 4.37 I/V curves measured in dark (blue) and under irradiation (red) of the plasmonic coupler at split-gate voltages of $V_{SG1} = -3$ V and $V_{SG2} = 3$ V. 110
Figure 4.38 (a) The detailed maps of open-circuit voltage V_{oc} under different split-gate voltages. (b) Five typical band diagrams induced by different split-gate voltages. 111

Die approbierte gedruckte Originalversion dieser Dissertation ist an der TU Wien Bibliothek verfügbar.
The approved original version of this doctoral thesis is available in print at TU Wien Bibliothek.
TU WIEN Bibliothek Your knowledge hub

Die approbierte gedruckte Originalversion dieser Dissertation ist an der TU Wien Bibliothek verfügbar.
The approved original version of this doctoral thesis is available in print at TU Wien Bibliothek.

List of abbreviations

AFM	Atomic force microscopy
Al	Aluminum
Al_2O_3	Aluminum oxide
ALD	Atomic layer deposition
Au	Gold
AOTF	Acousto-optical tunable filter
BHF	Buffered hydrofluoric acid
BOX	Buried oxide
C-band	Conventional band (the wavelength range 1530-1565 nm)
CCD	Charge coupled device
CMOS	Complementary metal oxide semiconductor
Cu	Copper
DC	Direct current
DOS	Density of states
EQE	External quantum efficiency
FCC	Face-centered cubic
FET	Field effect transistor
FinFET	Fin field effect transistor
FWHM	Full width at half maximum
GaAs	Gallium arsenide
Ge	Germanium
GeOI	Germanium on insulator
GeO_x	Germanium oxide
HF	Hydrofluoric acid
HI	Hydroiodic acid
IC	Integrated circuit
InGaAs	Indium gallium arsenide
IQE	Internal quantum efficiency
IR	Infrared
ITO	Indium tin oxide
I/V	Current-voltage

TU Bibliothek Your knowledge hub WIEN
Die approbierte gedruckte Originalversion dieser Dissertation ist an der TU Wien Bibliothek verfügbar.
The approved original version of this doctoral thesis is available in print at TU Wien Bibliothek.

LED	Light emitting diode
MOSFET	Metal oxide semiconductor field effect transistor
NIR	Near infrared
NW	Nanowire
NPC	Negative photoconductivity
PCB	Printed circuit board
PPC	Positive photoconductivity
PV	Photovoltaic
RC delay	Resistive-capacitive delay
RIE	Reactive ion etching
SBFET	Schottky barrier field effect transistor
SEM	Scanning electron microscopy
Si	Silicon
SOI	Silicon on insulator
SiO_2	Silicon oxide
SMU	Source measure unit
SPCM	Scanning photocurrent microscopy
SPP	Surface plasmon polariton
TE	Transverse electric
TEM	Transmission electron microscopy
TM	Transverse magnetic
TSMC	Taiwan semiconductor manufacturing company

Die approbierte gedruckte Originalversion dieser Dissertation ist an der TU Wien Bibliothek verfügbar.
The approved original version of this doctoral thesis is available in print at TU Wien Bibliothek.
TU WIEN Bibliothek Your knowledge hub

List of symbols

a	Lattice constant
$\vec{a}_1$, $\vec{a}_2$, $\vec{a}_3$	Fundamental vectors
A	Absorbance
D(E)	Density of states
D^*	Detectivity
D_n	Diffusion coefficient for electrons
D_p	Diffusion coefficient for holes
D_t	Surface trap level density
D_0	Homogeneous energy distribution from non-radiative decay for Al
$erf(x)$	Error function
$E_{kin,m}$	Kinetic energy of hot electrons in the metal
$E_{kin,s}$	Kinetic energy of hot electrons in the semiconductor
E_{ph}	Photon energy
E	Electric field
E_{bi}	Build-in electric field
E_{eff}	Effective electrostatic potential
E_F	Fermi level
E_{Fn}	Quasi-Fermi energy for electrons
E_C	Bottom edge of conduction band
E_g	Band gap
E_R	Trap energy level
E_V	Top edge of the valence band
E_{vac}	Vacuum energy level
E_A	Acceptor level
E_D	Donor level
E_i	Intrinsic level of an intrinsic semiconductor
Δf	Electrical bandwidth
f_{3dB}	3-dB bandwidth
$g(E)$	Density of states
g	Generation rate of hot carriers (or the SPP induced injection rate)
G_d	Conductance of semiconductor channel measured in the dark

Die approbierte gedruckte Originalversion dieser Dissertation ist an der TU Wien Bibliothek verfügbar.
The approved original version of this doctoral thesis is available in print at TU Wien Bibliothek.
TU Bibliothek Your knowledge hub WIEN

G_{ph}	Conductance of semiconductor channel under irradiation
ΔG	Photoconductance
g_m	Transconductance
h	Planck constant
$\hbar$	Dirac constant
H	Magnetic field
I_d	Dark current
I_{noise}	Noise current
I_{ph}	Photocurrent
I_{pl}	Plasmon current
J_0	Reverse-bias saturation current density
k_B	Boltzmann constant
k_m	Momenta of hot electrons in the metal
k_s	Momenta of hot electrons in the semiconductor
L_p	Propagation length of SPPs
m_e^*	Effective mass of electrons
m_h^*	Effective mass of holes
n_i	Intrinsic carrier concentration
n_{eff}	Effective refractive index
NA	Numerical aperture of the objective
N_A	Acceptor doping concentration
N_D	Donor doping concentration
N_C	Effective density of states in the conduction band
N_V	Effective density of states in the valence band
N_t	Trap density
n_{trap}	Density of trapped electrons
n_{hot}	Density of hot electrons
P_{esc}	Probability of the escape
$P_{tot}(E)$	Total transmission probability for hot electron injection
P_{opt}	Absorbed optical power
q	Elementary charge
Q_{trap}	Charge of the filled traps
T	Transmittance of light through the semiconductor

Die approbierte gedruckte Originalversion dieser Dissertation ist an der TU Wien Bibliothek verfügbar.
The approved original version of this doctoral thesis is available in print at TU Wien Bibliothek.
TU WIEN Bibliothek Your knowledge hub

$\mathcal{T}$	Transmission probability of hot electrons across the interface
V_{th}	Threshold voltage
ΔV_{th}	Light-induced shift of the threshold voltage
V_{BG}^{eff}	Effective gate voltage due to the photogating effect
W_n	Depletion width in the n-type region of p-n junction
W_p	Depletion width in the p-type region of p-n junction
W_m	Work function of the metal
W_{sc}	Work function of semiconductors
α	Optical absorption coefficient
β_n	Capture cross-section of electrons
β_p	Capture cross-section of holes
$\delta_{\boldsymbol{p}}$	Penetration depth of light in semiconductor
$\delta_{\boldsymbol{d}}$	Penetration depths of the SPP electric field in the dielectric
$\delta_{\boldsymbol{m}}$	Penetration depths of the SPP electric field in the metal
ε_0	Vacuum permittivity
ε_s	Relative permittivity of the semiconductor
ε_m	Relative permittivity of the metal
ε_d	Relative permittivity of the dielectric
ζ	Variance of the Gaussian function for the objective lens
$\eta_i(E_{ph})$	Internal quantum efficiency for internal photoemission
θ	Rotation angle of polarized light
λ	Wavelength of light in vacuum
λ_{SPP}	SPP wavelength
μ	Carrier mobility
$\Delta\mu$	Light-induced change of carrier mobility
ν	Frequency of light
ρ	Resistivity
σ_i	Intrinsic conductivity
σ_{ph}	Electrical conductivity under irradiation
τ_m	Mean scattering time of charge carriers
τ_n	Carrier lifetime for electrons
τ_p	Carrier lifetime for holes
τ_t	Detrapping lifetime

Die approbierte gedruckte Originalversion dieser Dissertation ist an der TU Wien Bibliothek verfügbar.
The approved original version of this doctoral thesis is available in print at TU Wien Bibliothek.
TU Bibliothek WIEN Your knowledge hub

τ_r	Rise time of photodetector responding to a light pulse
τ_f	Fall time of photodetector responding to a light pulse
τ_l	Effective lifetime of hot carriers
τ_{tr}	Transit time of the carriers through the semiconductor channel
τ_{th}	Thermalization time of hot electrons
τ_{rec}	Hot electron lifetime determined by band-to-band recombination
τ_{trap}	Trapping time
τ_{detrap}	Detrapping time
Φ_b	Effective barrier height
Φ_{bn}	Effective barrier height for hot electron injection
Φ_{bp}	Effective barrier height for hot hole injection
Ψ_{bi}	Build-in potential
Φ_c	Build-in contact potential for Schottky contact
χ	Electron affinity
ω	Angular frequency of the wave
ω_p	Plasma frequency

Die approbierte gedruckte Originalversion dieser Dissertation ist an der TU Wien Bibliothek verfügbar.
The approved original version of this doctoral thesis is available in print at TU Wien Bibliothek.
TU WIEN Bibliothek Your knowledge hub

Bibliography

[1] König K and Ostendorf A. 2015 Optically induced nanostructures: biomedical and technical applications. (Book, ISBN: 3110337185, De Gruyter)

[2] Madhukar J S and Janardan G V. 2020 Enhancement of short channel effect and drain induced barrier lowering in Fin-FET. Int. J. Innov. Technol. Explor. Eng. **9** 1303–1308.

[3] Edelstein D, Heidenreich J, Goldblatt R, Cote W, Uzoh C, Lustig N and Roper P et al. 1997 Full copper wiring in a sub-0.25 µm CMOS ULSI technology. IEEE IEDM, Washington, 773–776. (Conference report)

[4] Venkatesan S, Gelatos A V, Misra V, Smith B, Islam R, Cope J and Wilson B et al. 1997 A high performance 1.8V, 0.20 pm CMOS technology with copper metallization. IEEE IEDM, Boron, 769–772. (Conference report)

[5] Loke A L S. 1999 Process integration issues of low-permittivity dielectrics with copper for high-performance interconnects. (PhD dissertation, Stanford university)

[6] Chen X, Huo Y, Harris J S, Cho S and Park B G. 2014 O_2-enhanced surface treatment of Ge epitaxially grown on Si for heterogeneous Ge technology. Proc. Int. Symp. Consum. Electron. ISCE **3** 331–337.

[7] Zia R, Schuller J A, Chandran A and Brongersma M L. 2006 Plasmonics: the next chip-scale technology. Mater. Today **9** 20–27.

[8] Glassner S, Keshmiri H, Hill D J, Cahoon J F, Fernandez B, den Hertog M I and Lugstein A. 2018 Tuning electroluminescence from a plasmonic cavity-coupled silicon light source. Nano Lett. **18** 7230–7237.

[9] Melikyan A, Alloatti L, Muslija A, Hillerkuss D, Schindler P C, Li J and Palmer R et al. J 2014 High-speed plasmonic phase modulators. Nat. Photonics **8** 229–233.

[10] Ahmadivand A. 2018 Plasmonic nanoplatforms for biochemical sensing and medical applications. (PhD dissertation, Florida international university)

[11] Kumari S, Singh R R and Tripathi S M. 2022 Parametric optimization of hybrid plasmonic waveguide-based SOI ring resonator refractive index sensor. Plasmonics **17** 2417–2430.

[12] Salamin Y, Ma P, Baeuerle B, Emboras A, Fedoryshyn Y, Heni W and Cheng B et al. 2018 100 GHz plasmonic photodetector. ACS Photonics **5** 3291–3297.

Die approbierte gedruckte Originalversion dieser Dissertation ist an der TU Wien Bibliothek verfügbar.
The approved original version of this doctoral thesis is available in print at TU Wien Bibliothek.
TU WIEN Bibliothek Your knowledge hub

[13] Smirnov V, Stephan S, Westphal M, Emmrich D, Beyer A, Gölzhäuser A and Lienau C et al. 2021 Transmitting surface plasmon polaritons across nanometer-sized gaps by optical near-field coupling. ACS Photonics **8** 832–840.

[14] Nikolajsen T, Leosson K and Bozhevolnyi S I. 2004 Surface plasmon polariton based modulators and switches operating at telecom wavelengths. Appl. Phys. Lett. **85** 5833–5835.

[15] Schildkraut J S. 1988 Long-range surface plasmon eletrooptic modulator. Appl. Opt. **27** 4587–4590.

[16] Dionne J A, Diest K, Sweatlock L A and Atwater H A. 2009 PlasMOStor: A metal-oxide-Si field effect plasmonic modulator. Nano Lett. **9** 897–902.

[17] Lan H Y, Hsieh Y H, Chiao Z Y, Jariwala D, Shih M H, Yen T J and Hess O et al. 2021 Gate-tunable plasmon-enhanced photodetection in a monolayer MoS_2 phototransistor with ultrahigh photoresponsivity. Nano Lett. **21** 3083–3091.

[18] Zhang C, Luo Y, Maier S A and Li X. 2022 Recent progress and future opportunities for hot carrier photodetectors: from ultraviolet to infrared bands laser. Photonics Rev. **2100714** 1–29.

[19] Prangsma J C, Kern J, Knapp A G, Grossmann S, Emmerling M, Kamp M and Hecht B. 2012 Electrically connected resonant optical antennas. Nano Lett. **12** 3915–3919.

[20] Knight M W, King N S, Liu L, Everitt H O, Nordlander P and Halas N J. 2014 Aluminum for plasmonics. ACS Nano **8** 834–840.

[21] Lee D N and Lee H J. 2003 Effect of stresses on the evolution of annealing textures in Cu and Al interconnects J. Electron. Mater. **32** 1012–1022.

[22] Chalabi H, Schoen D and Brongersma M L. 2014 Hot-electron photodetection with a plasmonic nanostripe antenna. Nano Lett. **14** 1374–1380.

[23] Friedrich J, Ammon W and Müller G. 2015 Czochralski growth of silicon crystals. (Book)

[24] Glassner S. 2018 Tuning the optical properties of silicon nanowires by ultra-high strain and plasmonic coupling. (PhD dissertation, Vienna university of technology)

[25] Bartmann M G. 2020 Germanium nanowires for bolometric sensors. (PhD dissertation, Vienna university of technology)

[26] Suyog G, Blanka M, Yoshio N and Krishna C. 2013 Achieving direct band gap in germanium through integration of Sn alloying and external strain. J. Appl. Phys. **113** 073707.

Die approbierte gedruckte Originalversion dieser Dissertation ist an der TU Wien Bibliothek verfügbar.
The approved original version of this doctoral thesis is available in print at TU Wien Bibliothek.
TU Bibliothek WIEN Your knowledge hub

[27] Sui Z and Herman I P. 1993 Effect of strain on phonons in Si, Ge, and Si/Ge heterostructures. Phys. Rev. B **48** 17938–17953.

[28] Kingston R H. 1956 Review of germanium surface phenomena. J. Appl. Phys. **27** 101–114.

[29] Mukherjee S, Das K, Das S and Ray S K. 2018 Highly responsive, polarization sensitive, self-biased single GeO_2-Ge nanowire device for broadband and low power photodetectors. ACS Photonics **5** 4170–4178.

[30] Staudinger P. 2016 Ultrascaled germanium nanowires for highly sensitive and spatially resolved photon detection. (Master's thesis, Vienna university of technology)

[31] Malik A, Muneeb M, Pathak S, Shimura Y, Campenhout J, Loo R and Roelkens G. 2013 Germanium-on-silicon mid-infrared arrayed waveguide grating multiplexers. IEEE Photonics Technol. Lett. **25** 1805–1808.

[32] Staudinger P, Sistani M, Greil J, Bertagnolli E and Lugstein A. 2018 Ultrascaled germanium nanowires for highly sensitive photodetection at the quantum ballistic limit. Nano Lett. **18** 5030–5035.

[33] Zi W, Ren X, Ren X, Wei Q, Gao F and Liu S. 2016 Perovskite/germanium tandem: A potential high efficiency thin film solar cell design. Opt. Commun. **380** 1–5.

[34] Sistani M. 2019 Transport in ultra-scaled Ge quantum dots embedded in Al-Ge-Al nanowire heterostructures. (PhD dissertation, Vienna university of technology)

[35] Yang S, Mehl M and Papaconstantopoulos D. 1998 Application of a tight-binding total-energy method for Al, Ga, and In. Phys. Rev. B. **57** R2013.

[36] Ioffe Institute Electrical properties of Germanium (Ge). (Webpage, Link: https://www.ioffe.ru/SVA/NSM/Semicond/Ge/electric.html)

[37] Sze S M, Li Y and Ng K K. 2006 Physics of semiconductor devices. (Book, ISBN:1119429110, Wiley)

[38] Li S S and Thurder W R. 1977 The dopant density and temperature dependence of electron mobility and resistivity in n-type silicon. Solid State Electron. **20** 609–616.

[39] Schricker A D, Joshi S V., Hanrath T, Banerjee S K and Korgel B A. 2006 Temperature dependence of the field effect mobility of solution-grown germanium nanowires. J. Phys. Chem. B **110** 6816–6823.

[40] Shockley W. 1949 The Theory of p-n junctions in semiconductors and p-n Junction transistors. Bell Syst. Tech. J. **28** 425–489.

TU Bibliothek WIEN Your knowledge hub
Die approbierte gedruckte Originalversion dieser Dissertation ist an der TU Wien Bibliothek verfügbar.
The approved original version of this doctoral thesis is available in print at TU Wien Bibliothek.

[41] Hudait M K and Krupanidhi S B. 2001 Doping dependence of the barrier height and ideality factor of Au/n-GaAs Schottky diodes at low temperatures. Phys. B Condens. Matter **307** 125–137.

[42] Zhang Y, Han G, Wu H, Wang X, Liu Y, Zhang J and Liu H et al. 2018 Reduced contact resistance between metal and n-Ge by insertion of ZnO with argon plasma treatment. Nanoscale Res. Lett. **13** 1–8.

[43] Ang K W, Majumdar K, Matthews K, Young C D, Kenney C, Hobbs C and Kirsch P et al. 2012 Effective schottky barrier height modulation using dielectric dipoles for source/drain specific contact resistivity improvement. IEEE IEDM, 18-6. (Conference report)

[44] Jeon D Y, Pregl S, Park S J, Baraban L, Cuniberti G, Mikolajick T and Weber W M. 2015 Scaling and graphical transport-map analysis of ambipolar schottky-barrier thin-film transistors based on a parallel array of Si Nanowires. Nano Lett. **15** 4578–4584

[45] Heidary D S B, Qu W and Randall C A. 2015 Electrical characterization and analysis of the degradation of electrode Schottky barriers in $BaTiO_3$ dielectric materials due to hydrogen exposure. J. Appl. Phys. **117**, 124104.

[46] Goetzberger A, Knobloch J and Voss B. 1998 Crystalline silicon solar cells: technology and systems, applications. (Book, ISBN: 0471971448, Wiley)

[47] Pankove J I. 1975 Optical Processes in Semiconductors. (Book, ISBN: 0486602753, Dover Publications)

[48] van Eerden M, van Gastel J, Bauhuis G J, Mulder P, Vlieg E and Schermer J J. 2020 Observation and implications of the Franz-Keldysh effect in ultrathin GaAs solar cells. Prog. Photovoltaics Res. Appl. **28** 779–787

[49] Lee S M, Kwong A, Daehwan J, Faucher J, Shen L, Biswas R and Lee M L et al. 2015 High performance ultrathin GaAs solar cells enabled with heterogeneously integrated dielectric periodic nanostructures. ACS Nano **9** 10356–10365.

[50] Satpathy R and Pamuru V. 2020 Solar PV power: design, manufacturing and applications from sand to systems. (Book, ISBN: 0128176261, Academic Press)

[51] Picozzi S, Asahi R, Geller C B and Freeman A J. 2002 Accurate first-principles detailed-balance determination of Auger recombination and impact ionization rates in semiconductors. Phys. Rev. Lett. **89** 1–4.

[52] Irish R T and Bryant G H. 1964 Determination of ionization rate and electron temperature in a mercury discharge by a microwave method. Proc. Phys. Soc. **84** 975.

Die approbierte gedruckte Originalversion dieser Dissertation ist an der TU Wien Bibliothek verfügbar.
The approved original version of this doctoral thesis is available in print at TU Wien Bibliothek.
TU WIEN Bibliothek Your knowledge hub

[53] Frank F and Rolf R. G. 2006 Metal optics near the plasma frequency. (Book, ISBN: 3662151952, Springer)

[54] R. H. RITCHIE. 1957 Plasma losses by fast electrons in thin films. Phys. Rev. **106** 874.

[55] Powell C J and Swan J B. 1959 Origin of the characteristic electron energy losses in aluminum. Phys. Rev. **115** 869–875.

[56] C.J.Powell and J.B.Swan. 1960 Effect of oxidation on the characteristic loss spectra of aluminnm and magnesium. Phys. Rev. **118** 640–643.

[57] Otto A 1967 Theory of plasmon Exeitation in Thin thin film by electrons of Non-Normal Ineidence **401** 401–406.

[58] Plummer W, Tsuei K D and Kim B O 1995 The impact of the concept of a surface plasmon Nucl. Inst. Methods Phys. Res. B **96** 448–59.

[59] Luo M R. 2001 The encyclopedia of science and technology. (Book, ISBN: 0415937248, Routledge)

[60] Maier S A. 2007 Plasmonics: Fundamentals and Applications. (Book, ISBN: 0387331506, Springer)

[61] Wei H, Pan D, Zhang S, Li Z, Li Q, Liu N and Wang W et al. 2018 Plasmon waveguiding in nanowires. Chem. Rev. **118** 2882–926.

[62] Ahlawat M, Mittal D and Govind Rao V. 2021 Plasmon-induced hot-hole generation and extraction at nano-heterointerfaces for photocatalysis. Commun. Mater. **2** 1–15.

[63] Ford G W and Weber W H. 1984 Electromagnetic interactions of molecules with metal surfaces. Phys. Rep. **113** 195–287.

[64] Jain P K and El-Sayed M A. 2010 Plasmonic coupling in noble metal nanostructures Chem. Phys. Lett. **487** 153–164.

[65] Sundararaman R, Narang P, Jermyn A S, Goddard W A and Atwater H A. 2014 Theoretical predictions for hot-carrier generation from surface plasmon decay. Nat. Commun. **5** 1–8.

[66] Bube R H. 1992 Photoelectronic properties of semiconductors. (Book, ISBN: 0521406811, Cambridge University Press)

[67] García De Arquer F P, Armin A, Meredith P and Sargent E H. 2017 Solution-processed semiconductors for next-generation photodetectors. Nat. Rev. Mater. **2** 1–17.

[68] Liu R, Zhang J, Zhou H, Song Z, Song Z, Grice C R and Wu D et al. 2020 Solution-processed high-quality cesium lead bromine perovskite photodetectors with high detectivity for application in visible light communication. Adv. Opt. Mater. **8** 1–7.

TU Bibliothek WIEN Your knowledge hub
Die approbierte gedruckte Originalversion dieser Dissertation ist an der TU Wien Bibliothek verfügbar.
The approved original version of this doctoral thesis is available in print at TU Wien Bibliothek.

[69] Leenheer A J, Narang P, Lewis N S and Atwater H A. 2014 Solar energy conversion via hot electron internal photoemission in metallic nanostructures: Efficiency estimates. J. Appl. Phys. **115** 134301.

[70] Song Z, Sistani M, Wind L, Pohl D, Rellinghaus B, Weber W M and Lugstein A. 2021 Plasmon-assisted polarization-sensitive photodetection with tunable polarity for integrated silicon photonic communication systems. Nanotechnology **32** 505205.

[71] Semiconductor, Virginia. 2002 The General Properties of Si , Ge , SiGe , SiO_2 and Si_3N_4. (Handbook)

[72] Hall K L, Lenz G, Ippen E P and Raybon G. 1992 Heterodyne pump–probe technique for time-domain studies of optical nonlinearities in waveguides. Opt. Lett. **17** 874.

[73] El Hajraoui K, Luong M A, Robin E, Brunbauer F, Zeiner C, Lugstein A and Gentile P et al. 2019 In situ transmission electron microscopy analysis of aluminum-germanium nanowire solid-state reaction. Nano Lett. **19** 2897–2904.

[74] Wind L, Sistani M, Song Z, Maeder X, Pohl D, Michler J and Rellinghaus B et al. 2021 Monolithic metal-semiconductor-metal heterostructures enabling next-generation germanium nanodevices. ACS Appl. Mater. Interfaces **13** 12393–12399.

[75] Kral S, Zeiner C, Stöger-Pollach M, Bertagnolli E, Den Hertog M I, Lopez-Haro M and Robin E et al. 2015 Abrupt Schottky junctions in Al/Ge nanowire heterostructures. Nano Lett. **15** 4783–4787.

[76] Delaforce J, Sistani M, Kramer R B, Luong M A, Roch N, Weber W M and Lugstein A et al. 2021 Al–Ge–Al nanowire heterostructure: from single-hole quantum dot to Josephson effect. Adv. Mater. **33**, 2101989.

[77] Sistani M, Staudinger P and Lugstein A. 2020 Polarity control in Ge nanowires by electronic surface doping. J. Phys. Chem. C **124** 19858–19863.

[78] Wang D, Chang Y L, Wang Q, Cao J, Farmer D B, Gordon R G and Dai H 2004 Surface chemistry and electrical properties of germanium nanowires J. Am. Chem. Soc. **126** 11602–11611.

[79] Furchi M M, Polyushkin D K, Pospischil A and Mueller T. 2014 Mechanisms of photoconductivity in atomically thin MoS_2 Nano Lett. **14** 6165–6170.

[80] Wei P, Chattopadhyay S, Yang M, Tong S, Shen J, Lu C and Shih H et al. 2010 Room-temperature negative photoconductivity in degenerate InN thin films with a supergap excitation. Phys. Rev. B **81** 045306.

Die approbierte gedruckte Originalversion dieser Dissertation ist an der TU Wien Bibliothek verfügbar.
The approved original version of this doctoral thesis is available in print at TU Wien Bibliothek.
TU WIEN Bibliothek Your knowledge hub

[81] Yang Y, Peng X, Kim H S, Kim T, Jeon S, Kang H K and Choi W et al. 2015 Hot carrier trapping induced negative photoconductance in InAs nanowires toward novel nonvolatile memory. Nano Lett. **15** 5875–5882.

[82] Baek E, Rim T, Schütt J, Baek C K, Kim K, Baraban L and Cuniberti G 2017 Negative photoconductance in heavily doped Si nanowire field-effect transistors. Nano Lett. **17** 6727–6734.

[83] Yang Y, Li J, Choi S, Jeon S, Cho J H, Lee B H and Lee S. 2021 High-responsivity $PtSe_2$ photodetector enhanced by photogating effect. Appl. Phys. Lett. **118** 013103.

[84] Lindley D H and Banbury P C. 1960 Surface relaxation effects in germanium at reduced temperatures. J. Phys. Chem. Solids **14** 200–207.

[85] Zürch M, Chang H-T T, Borja L J, Kraus P M, Cushing S K, Gandman A and Kaplan C J et al. Direct and simultaneous observation of ultrafast electron and hole dynamics in germanium. Nat. Commun. **8** 15734.

[86] Dosunmu O I, Cannon D D, Emsley M K, Ghyselen B, Liu J, Kimerling L C and Ünlü M S. 2004 Resonant cavity enhanced Ge photodetectors for 1550 nm operation on reflecting Si substrates. IEEE J. Sel. Top. Quantum Electron. **10** 694–701

[87] Bird G R and Parrish M. 1960 The wire grid as a near-infrared polarizer. J. Opt. Soc. Am. **50** 886.

[88] Auton J P. 1967 Infrared transmission polarizers by photolithography. Appl. Opt. **6** 1023.

[89] Bräuninger H, Kraus H, Dangschat H, Beuermann K P, Predehl P and Trümper J. 1979 Fabrication of transmission gratings for use in cosmic x-ray and XUV astronomy. Appl. Opt. **18** 3502.

[90] Sonek G J, Wagner D K and Ballantyne J M. 1981 Ultraviolet graing polaizers. Journal of vacuum science & technology **19** 921–923.

[91] Lochbihler H, Polnau E and Predehl P. 1995 Polarimetry of transmission gratings. Appl. Opt. **34** 5725.

[92] Fan P, Huang K C Y, Cao L and Brongersma M L. 2013 Redesigning photodetector electrodes as an optical antenna. Nano Lett. **13** 392–396.

[93] Echtermeyer T J, Milana S, Sassi U, Eiden A, Wu M, Lidorikis E and Ferrari A C. 2016 Surface plasmon polariton graphene photodetectors. Nano Lett. **16** 8–20.

[94] Sobhani A, Knight M W, Wang Y, Zheng B, King N S, Brown L V and Fang Z et al. 2013 Narrowband photodetection in the near-infrared with a plasmon-induced hot electron device. Nat. Commun. **4** 1643.

TU Bibliothek Your knowledge hub WIEN
Die approbierte gedruckte Originalversion dieser Dissertation ist an der TU Wien Bibliothek verfügbar.
The approved original version of this doctoral thesis is available in print at TU Wien Bibliothek.

[95] Ruda H E and Shik A. 2005 Polarization-sensitive optical phenomena in semiconducting and metallic nanowires. Phys. Rev. B. **72** 115308.

[96] Buddhiraju S, Shi Y, Song A, Wojcik C, Minkov M, Williamson I A D and Dutt A et al. 2020 Absence of unidirectionally propagating surface plasmon-polaritons at nonreciprocal metal-dielectric interfaces. Nat. Commun. **11** 674.

[97] Bernardi M, Mustafa J, Neaton J B and Louie S G. 2015 Theory and computation of hot carriers generated by surface plasmon polaritons in noble metals. Nat. Commun. **6** 7044.

[98] Brown A M, Sundararaman R, Narang P, Goddard W A and Atwater H A. 2016 Nonradiative plasmon decay and hot carrier dynamics: Effects of phonons, surfaces, and geometry. ACS Nano **10** 957–966.

[99] Kamieniecki E. 2014 Effect of charge trapping on effective carrier lifetime in compound semiconductors: High resistivity CdZnTe. J. Appl. Phys. **116** 193702.

[100] Qi Z, Zhai Y, Wen L, Wang Q, Chen Q, Iqbal S and Chen G et al. 2017 Au nanoparticle-decorated silicon pyramids for plasmon-enhanced hot electron near-infrared photodetection. Nanotechnology **28** 275202.

[101] Liao F, Deng J, Chen X, Wang Y, Zhang X, Liu J and Zhu H et al. 2020 A dual-gate MoS_2 photodetector based on interface coupling effect. Small **16** 1904369.

[102] Zhao Q, Wang W, Carrascoso-Plana F, Jie W, Wang T, Castellanos-Gomez A and Frisenda R. 2020 The role of traps in the photocurrent generation mechanism in thin InSe photodetectors. Mater. Horizons **7** 252–262.

[103] Fermi T and Bube R H. 1955 Infrared quenching and a unified description of photoconductivity phenomena in cadmium sulfide and selenide. Phys. Rev. **99** 1105.

[104] Klee V, Preciado E, Barroso D, Nguyen A E, Lee C, Erickson K J and Triplett M et al. 2015 Superlinear composition-dependent photocurrent in CVD-Grown monolayer $MoS_{2(1-x)}Se_{2x}$ alloy devices. Nano Lett. **15** 2612–2619.

[105] Li L, Wang W, Gan L, Zhou N, Zhu X, Zhang Q and Li H et al. 2016 Ternary Ta_2NiSe_5 flakes for a high-performance infrared photodetector. Adv. Funct. Mater. **26** 8281–8289.

[106] Sugioka K. 2017 Progress in ultrafast laser processing and future prospects. Nanophotonics **6** 393–413.

[107] Ziebell M, Marris-Morini D, Rasigade G, Fédéli J-M, Crozat P, Cassan E and Bouville D et al. 2012 40 Gbit/s low-loss silicon optical modulator based on a pipin diode. Opt. Express **20** 10591.

Die approbierte gedruckte Originalversion dieser Dissertation ist an der TU Wien Bibliothek verfügbar.
The approved original version of this doctoral thesis is available in print at TU Wien Bibliothek.
TU WIEN Bibliothek Your knowledge hub

[108] Reed G T, Mashanovich G, Gardes F Y and Thomson D J. 2010 Silicon optical modulators. Nat. Photonics 518–526.

[109] Ghayour R and Bakhtazad A. 1998 Trade-off between speed and efficiency of silicon metal-i-n photodetectors. Solid. State. Electron. **42** 715–720.

[110] Cao L, Park J S, Fan P, Clemens B and Brongersma M L. 2010 Resonant germanium nanoantenna photodetectors. Nano Lett. **10** 1229–1233.

[111] Sorger V J and Maiti R. 2020 Roadmap for gain-bandwidth-product enhanced photodetectors: opinion. Opt. Mater. Express **10** 2192.

[112] Sistani M, Staudinger P, Greil J, Holzbauer M, Detz H, Bertagnolli E and Lugstein A. 2017 Room temperature quantum ballistic transport in monolithic ultrascaled Al-Ge-Al nanowire heterostructures. Nano Lett. **17** 4556–4561.

[113] MacDonald K F, Sámson Z L, Stockman M I and Zheludev N I. 2009 Ultrafast active plasmonics. Nat. Photonics **3** 55–58.

[114] Mongin D, Shaviv E, Maioli P, Crut A, Banin U, Del Fatti N and Vallée F. 2012 Ultrafast photoinduced charge separation in metal-semiconductor nanohybrids. ACS Nano **6** 7034–7043.

[115] Chen G, Ni G, Mahan G, Tong J K, Meroueh L, Zeng L and Boriskina S V et al. 2017 Losses in plasmonics: from mitigating energy dissipation to embracing loss-enabled functionalities. Adv. Opt. Photonics **9** 775–827.

[116] Khurgin J B 2015 How to deal with the loss in plasmonics and metamaterials. Nat. Nanotechnol. **10** 2–6.

[117] Jacoboni C, Nava F, Canali C and G. Ottaviani. 1981 Electron drift velocity and diffusivity in germanium. Phys. Rev. B **24** 1014.

[118] Prasankumar R P, Choi S, Trugman S A, Picraux S T and Taylor A J. 2008 Ultrafast electron and hole dynamics in germanium nanowires. Nano Lett. **8** 1619–1624.

[119] Wu C C, Jariwala D, Sangwan V K, Marks T J, Hersam M C and Lauhon L J. 2013 Elucidating the photoresponse of ultrathin MoS_2 field-effect transistors by scanning photocurrent microscopy. J. Phys. Chem. Lett. **4** 2508–2513.

[120] Wind L, Böckle R, Sistani M, Schweizer P, Maeder X, Michler J and Murphey C G E et al. 2022 Monolithic and single-crystalline aluminum-silicon heterostructures. ACS Appl. Mater. Interfaces **14** 26238–26244.

[121] Cristoloveanu S, Lee K H, Park H and Parihar M S. 2019 The concept of electrostatic doping and related devices. Solid. State. Electron. **155** 32–43.

Die approbierte gedruckte Originalversion dieser Dissertation ist an der TU Wien Bibliothek verfügbar.
The approved original version of this doctoral thesis is available in print at TU Wien Bibliothek.
TU WIEN Bibliothek Your knowledge hub

[122] Du W, Wang T, Chu H S and Nijhuis C A. 2017 Highly efficient on-chip direct electronic-plasmonic transducers. Nat. Photonics **11** 623–627.

TU Bibliothek, WIEN Your knowledge hub
Die approbierte gedruckte Originalversion dieser Dissertation ist an der TU Wien Bibliothek verfügbar.
The approved original version of this doctoral thesis is available in print at TU Wien Bibliothek.